technische universität dortmund

KASANMASCHEFF LAB

Advanced EPR Spectroscopy: unraveling the binding behavior and modes of metals and biomolecules

Dissertation

for the degree of
"Doctor rerum naturalium"

TU Dortmund University
Department of Chemistry and Chemical Biology

Submitted by
Victor Richard Selve
from Dortmund, Germany
Dortmund, October 2025

Spins,
spins everywhere

Dissertation in der Fakultät Chemie und Chemische Biologie, geschrieben an der Technischen Universität Dortmund

This Doctoral Thesis has been elaborated from May 2021 till October 2025 and has been examined by a committee of the Faculty of Chemistry and Chemical Biology as follows:

Principal advisor: **Prof. Dr. Müge Kasanmascheff**
Faculty of Chemistry and Chemical Biology,
TU Dortmund University

Coexaminer: **Prof. Dr. Hannes Mutschler**
Faculty of Chemistry and Chemical Biology,
TU Dortmund University

Submission date: 07.10.2025

Abstract

Modern Electron Paramagnetic Resonance (EPR) has found applications in nearly every field of science. However, while many methods spread into other fields through their high applicability and ease of use, EPR tends to be the opposite. Countless experiments with countless variations for different samples, all requiring different considerations and giving slightly different parts of the full picture. These differences between the experiments can be leveraged to untangle complex systems by combining different EPR techniques. This thesis shows how a small group of EPR experiments can be used in entirely different paradigms to extract otherwise difficult-to-collect data.

Although they are as different as can be, both ribonucleotide reductase (RNR) and guanine quadruplexes (GQs) form cornerstones of life as we know it. Where RNR's role is catalytic, being the only enzyme capable of creating new deoxynucleotides, the building blocks of DNA, the function of guanine quadruplexes is primarily in their structure, and the interaction of that structure with its surroundings, often to create regulatory effects in the genome.

This thesis examines the β_2-subunit of class Ia RNR, which generates a tyrosyl radical necessary for subsequent RNR activity. Specifically, the generation of the necessary di-iron cofactors, or more precisely, what happens when manganese is incorporated in place of iron, is studied. It combines multiple dipolar spectroscopy methods as well as different types of field-sweeps to gain information on global binding modes of manganese, uncovering a previous misinterpretation of data by combining the results of all these methods. Given the central importance RNR has in cells, deepening our understanding of how RNR functions is a top priority.

Furthermore, this thesis examines the interaction of GQ-dimers and the binding of intercalators within GQs. This work builds on previous work with highly rigid copper labels for GQs, which can be used for high-precision dipolar distance measurements. To study the dynamics of GQ systems, a new measurement scheme for quantitative dipolar distance measurements is created, which exploits the large orientation selection of copper rather than recording complete orientation-averaged spectra. To this end, the implications and treatment of orientation selection as it influences quantitative dipolar spectroscopy measurements are discussed for different types of measurements in different systems. The application of the new measurement scheme was able to uncover an unexpected effect of the intercalator PIPER onto GQ-dimers, as well as a switch-like behavior between different binding modes not seen before. It furthermore lays the foundation for the usage of copper-labeled GQs not only as an EPR ruler but also as playing an active role in future drug development.

Zusammenfassung

Moderne Elektronenparamagnetspektroskopie hat ihren Weg in fast jedes wissenschaftliche Feld gefunden. Wohingegen jedoch die meisten Methoden, die so fachübergreifend Verwendung finden, durch breite Anwendbarkeit und einfache Nutzung charakterisiert sind, ist es bei EPR eher umgekehrt. Unzählige Experimente mit unzähligen Variationen je nach Probe. Und alle zeigen einen etwas anderen Ausschnitt des Gesamtbildes. Diese Unterschiede können genutzt werden, um Eigenschaften komplizierter Systeme mithilfe verschiedener Experimente und Parameter auseinander zu ziehen. Diese Arbeit demonstriert, wie ein kleines Set von EPR-Methoden genutzt werden kann, um in verschiedenen Systemen sonst nur schwierig zugängliche Informationen zu extrahieren.

Obwohl sie wohl unterschiedlicher nicht sein könnten, sind sowohl Ribonukleotidreduktase (RNR) als auch Guanin-Quadruplexe (GQs) instrumental für Leben, wie wir es kennen. Wo die Rolle von RNR darin besteht, als einziges Enzym neue Desoxyribonukleotide, die Bausteine für DNS, herzustellen, ist die Rolle von GQs durch ihre Struktur in DNS und Interaktion mit der Umgebung und anderen GQs gekennzeichnet. Oft spielen diese Interaktionen wichtige Rollen in der Kontrolle und Regulation des Genoms.

Diese Arbeit charakterisiert die β_2-Untereinheit von Klasse Ia RNR, welche ein Tyrosilradikal generiert, was für die Aktivität von RNR essentiell ist. Im Genaueren beschäftigt sich die Arbeit damit, wie sich der zur Radikalgenerierung benötigte Dieisen-Kofaktor bildet, beziehungsweise was passiert, wenn β_2 fälschlicherweise Mangan bindet. Hierfür wurden sowohl mehrere dipolare Spektroskopie-Methoden als auch feldabhängige Messungen kombiniert, um die globalen Bindungsverhältnisse von Mangan in β_2 zu charakterisieren. In diesem Zusammenhang wird eine Fehlinterpretation in der Literatur aufgedeckt, die nur durch Kombination aller dieser Methoden ersichtlich wird. Die zentrale Rolle von RNR in der Zelle macht das Verständnis des Mechanismus von RNR zu einem sehr wichtigen Thema.

Des Weiteren wird in dieser Arbeit das Bindeverhalten von GQs mit sich selbst und mit Interkalatoren untersucht. Diese Arbeit erweitert die vorherige Arbeit mit Kupferlabeln für GQs, welche höchst präzise Distanzmessungen ermöglichen. Dazu wurde ein neues Messschema entwickelt, welches die starke Orientierungsselektivität von dipolaren Distanzmessungen in mit Kupfer gelabelten GQs ausnutzt, um über quantitative Messungen die Dynamik der Systeme zu charakterisieren. Hierbei werden die Einflüsse von Orientierungselektivität auf Modulationsamplitude und quantitative Messungen ausführlich diskutiert. Dies erlaubte, einen unerwarteten Effekt, den das Binden des Interkalators PIPER auf die Stabilität von GQ-dimeren hat, zu ermitteln. Des Weiteren wurde eine schalterartige Änderung im Bindungsmodus von PIPER entdeckt. Diese Forschung legt die Grundlage für die Nutzung von kupfergelabelten GQs jenseits ihrer Anwendung als Modellsystem für EPR-Distanzmessungen, als aktiver Reporter in der Entwicklung von neun Medikamenten.

Conference contributions

Oral presentation

2024 Mar. RESOLV Klausurtagung 2024

Poster presentation

2022 Aug. 43rd FGMR Annual Discussion Meeting

2022 Sept. RESOLV Klausurtagung 2022

2024 Feb. Tag der Chemie, TU Dortmund

Publications

I. Heghmanns, Melanie; Yadav, Shalini; Boschmann, Sergius; **Selve, Victor R.**; Veliju, Astrit; Brocks, Claudia et al. (2025): Distinct Valence States of the 4Fe4S Cluster Revealed in the Hydrogenase CrHydA1. In Angewandte Chemie (International ed. in English) 64 (14), e202424167. DOI: 10.1002/anie.202424167.

II. Kutin, Yury; Reitz, Justus; Drosou, Maria; Antoni, Patrick W.; He, Yijie; **Selve, Victor** R. et al. (2025): Triplet Vinylidenes Based on (Benz)imidazole and 1,2,3-Triazole N-Heterocycles. In JACS Au 5 (6), pp. 2884–2897. DOI: 10.1021/jacsau.5c00491.

III. Double electron-electron resonance spectroscopy for precise reaction tracking in DNA dimerization, 2025,
in preparation

IV. Mismetallation or regulation? Role of manganese ions in tuning the activity of ribonucleotide reductase
in preparation.

Acknowledgments

First and foremost, I want to thank my supervisor, Prof. Dr. Müge Kasanmascheff. I had the pleasure of being a member of her lab from my bachelor's studies through my master's studies and during my PhD. She always supported me and encouraged me to learn new things. Furthermore, I would like to thank her for entrusting me with the spectrometers and enabling me to spend two months in Songi Han's lab at UCSB, where I learned about spectrometer instrumentation and ODNP.
I would also like to thank Songi and her lab for the warm welcome and the very educational time spent there.
Finally, I would like to thank the RESOLV Cluster of Excellence for sponsoring my trip to UCSB and financially supporting my PhD studies as well as giving me the opportunity to network and mix with other fields I usually would never have come into contact with.

I want to thank Prof. Dr. Hannes Mutschler for being my second supervisor.

I would also like to thank Prof. Dr. Guido Clever, who provided me with the opportunity to work on the copper-labeled guanine-quadruplex developed by his group. I especially want to thank Lukas Stratmann and Simon Kotnig for providing me with the guanine-quadruplex samples used in this work.

Next, I would like to thank Prof. Dr. Daniel Summerer for allowing me to use his lab for S1 work and the members of his lab for helping me navigate the lab.

Last but not least, I would like to thank all past and present members of the Kasanmascheff group. It has been a lot of fun working with all of them over the years, with everybody always keeping a cheerful attitude. Special thanks go out to Dr. Melanie Heghmanns, for giving me the opportunity to work on the iron sulfur cluster project, Viktoria Gocke and Shari Meichsner for providing the many samples for the RNR project, Yury Kutin for indulging my random ideas and questions about EPR, and finally, a big thanks goes to Simon Schumann, who has helped me out more times than I can count.

Finally, I want to thank my family and friends, who always supported me during my studies and probably still don't know what a blocking transfer line is, but know that it makes me very frustrated.

Contents

Abstract IV
Zusammenfassung V
Conference contributions VI
Oral presentation VI
Poster presentation VI
Publications VI
Acknowledgments VII
Contents VIII
1. Introduction and motivation 11
1.1. RNR 12
1.2. GQ 14
2. Theoretical background 16
2.1. Basic EPR theory 16
2.2. Spin Hamiltonian 17
2.3. CW-spectroscopy 19
2.4. Pulse spectroscopy 20
2.4.1. Hahn-echo 22
2.4.2. T_1/T_2 relaxation 23
2.5. Dipolar spectroscopy 24
2.5.1. Orientation selection 28
2.5.2. Modulation depth and the effect of orientation selection on modulation depth 30
3. Guanine Quadruplexes 35
3.1. Monomer shuffling and protocol development 36
3.1.1. DEER vs RIDME 42
3.1.2. Monomer shuffling 44
3.2. Intercalation and temperature dependence 45
3.2.1. PIPER intercalation 45
3.2.2. Temperature dependence 46
3.2.3. Double intercalation 47
3.3. Conclusion 49
3.4. Materials and methods 49

3.4.1. Sample preparation 49
3.4.2. Measurement parameters 50
3.4.3. Data analysis 52
4. RNR 53
4.1. Tyr-DEER 55
4.2. Mn-Mn DEER 62
4.3. Power-dependent field sweeps 65
4.4. Conclusions 69
4.5. Materials and methods 70
4.5.1. Sample preparation 70
4.5.2. Measurement parameters 72
5. Appendix 74
5.1. Normalizations and procedures for conversion between the XQ-band machine and the Q-band standalone 74
5.1.1. Power levels 74
5.1.2. Fieldshifts 74
5.2. DEER with chirp pulses 78
5.2.1. QTII resonator 78
5.2.2. Pulse optimisation for Tyr-FeMn in β_2 79
5.3. Additional spectra 80
5.4. RNR DEER 84
5.4.1. Alternative pulse length nutation 84
5.4.2. Manganese artefact 85
5.4.3. Manganese ruler 86
5.5. Guanine quadruplex 88
5.5.1. Guanine quadruplex RIDME dimerization approximation 88
5.5.2. Guanine quadruplex chirp DEER 91
Abbreviations 92
List of figures 93
List of tables 101
References 103
List of used Tools 114

1.
Introduction and motivation

Since the first EPR (electron paramagnetic resonance) spectroscopy measurements,[1–3] the study of unpaired electron-bearing atoms and molecules (paramagnetic centers) has found applications in almost every field of science[4–6] ranging from its origin in physics to material sciences like catalysis[7,8] and polymer science,[9] environmental biology,[10] geology,[11] medicine,[12,13] and biochemistry.[14] Furthermore, EPR can access a multitude of different information, with just its applications for in vivo and in vitro biochemistry, including measurements of protein mobility, solvent accessibility, environmental sensing of pH, viscosity, ions, and pressure, as well as water dynamics with nitroxide spin labels;[15–21] the identification, characterization of their environment, and quantification of different metal clusters in proteins,[22–27] structural elucidation via distance measurements between different paramagnetic centers and nuclei,[28,29] and more. Furthermore, due to EPR detection being limited to the paramagnetic species, EPR is not limited by the size of the studied system, which stands in stark contrast to EPR's sibling method NMR, which uses the same principles to study nuclei and can easily become uninterpretable when applied to big molecules. One would think that with so many potential applications, EPR would have many standardized methods available to the masses. However, the majority of EPR experiments are still limited to expert use.[5] While a lack of accessible EPR instrumentation, as well as the need to incorporate spin labels for systems without natural paramagnetic centers, are significant contributors, another issue with many EPR experiments is their poor generalizability.[5] Few EPR experiments are compatible with all types of EPR samples, and even within an experiment, vastly different parameters are required. In addition, the correct interpretation of data and which information can be accessed depends highly on the type and parameters of the experiment, and often other EPR properties of the sample need to be taken into account as well. However, while this specificity can make EPR data interpretation less straightforward, it can also be leveraged to extract additional information on systems by combining different methods to paint a more complete picture.

Field-swept EPR presents arguably the most basic of EPR experiments, with any standard EPR spectrometer being able to record some form of field-swept EPR. It enables the rapid detection and quantification of paramagnetic species, as well as the basic determination of many EPR parameters.[30,31] However, even a basic method like field sweeps has multiple implementations, with very different considerations in continuous wave (CW) and electron spin echo (ESE)-detected field sweeps. While signal intensity in (non-saturating) CW is virtually agnostic towards the relaxation properties of different paramagnetic species and easily accounts for different spin quantum numbers, making quantitative measurements as well as the simulation of a full spectrum fairly straightforward,[30,32] pulse EPR can be supremely sensitive to each of

these parameters.[25,33,34] Although this can make quantitative measurements and simulations significantly more complicated, that same sensitivity allows pulse EPR to separate different species based on their properties, detangling mixtures of paramagnetic species too complicated for CW.

Another fairly common group of EPR methods is dipolar EPR measurements, which leverage the interaction between paramagnetic centers to gain information on the distance and angle between them. These methods have also found application in quantitative measurements, although they remain a minority case.[35–37] Among the various dipolar methods, double electron-electron resonance spectroscopy (DEER) has established itself as the most prevalent, followed by its sibling, RIDME. The application of structural DEER on spin-labeled biomolecules is arguably the closest thing modern EPR has to offer in terms of standardized methods and protocols.[6] However, if one moves away from the world of purely structural DEER on nitroxide-labeled, otherwise EPR-inactive proteins, the same image as before emerges: different methods and parameters enable selective examination and detangling the respective parts of the EPR image.

1.1. RNR

In addition to labeled biomolecules, dipolar spectroscopy is also used to study biomolecules that naturally carry organic radicals and paramagnetic metallic cofactors.

Ribonucleotide reductase (RNR) is one such protein, being the first protein where organic radicals were found to be part of its working mechanism.[38] Still, many questions about its underlying mechanisms and regulation remain unanswered. RNRs are responsible for reducing nucleotide di-/tri-phosphates (NDP/NTP) to deoxynucleotide di-/tri-phosphates (dNDP/dNTP) (Figure 1a). Since this is the only way to add new dNTPs to the dNTP pool for all organisms, RNR presents a key player in the survival of all life. As such, RNR activity requires very tight regulation, with misregulation being associated with the formation of tumor cells.[38–45] As such, RNR has proven itself to be an essential drug target, primarily for cancer therapy,[46–49] but also for antiviral drugs,[50] antibiotics[51,52] and anthelmintics[53].

While many different RNRs with different oxygen tolerance and metal cofactors exist, *E. coli* class Ia has emerged as a model system for studying class Ia RNRs, to which human RNR also belongs.[41,43,54] Like all class I RNRs, it is aerobic and, being of class Ia, it uses di-iron as its metal cofactor. Its active unit consists of two homodimers, the α_2 and the β_2-subunits (Figure 1b).[a] The α_2 unit contains the catalytic side where NDPs are reduced, a regulatory side where ATP promotes the formation of the $\alpha_2\beta_2$ complex, and a side that influences the specificity binding dATP/ATP, dGTP, or dTTP, promoting the binding of UDP/CDP, ADP, or GDP as substrates, respectively. For α_2 to be active, it needs to form a radical (C_{439}•). The required radical is generated via proton-coupled electron transport from a tyrosyl radical (Y_{122}•) in the β_2 subunit.[55–57] β_2 is proposed to follow a `two or none` model where each β_2 will either generate Y_{122}• in both β-subunits or neither.[58] Formation of Y_{122}• requires the formation of a metal di-iron cofactor (Figure 1c).

[a] The use of α and β to refer to the subunits of RNRs is not exclusive to class Ia, however, unless otherwise specified, α_2 and β_2 in this work refer to the subunits of *E. Coli* class Ia RNR.

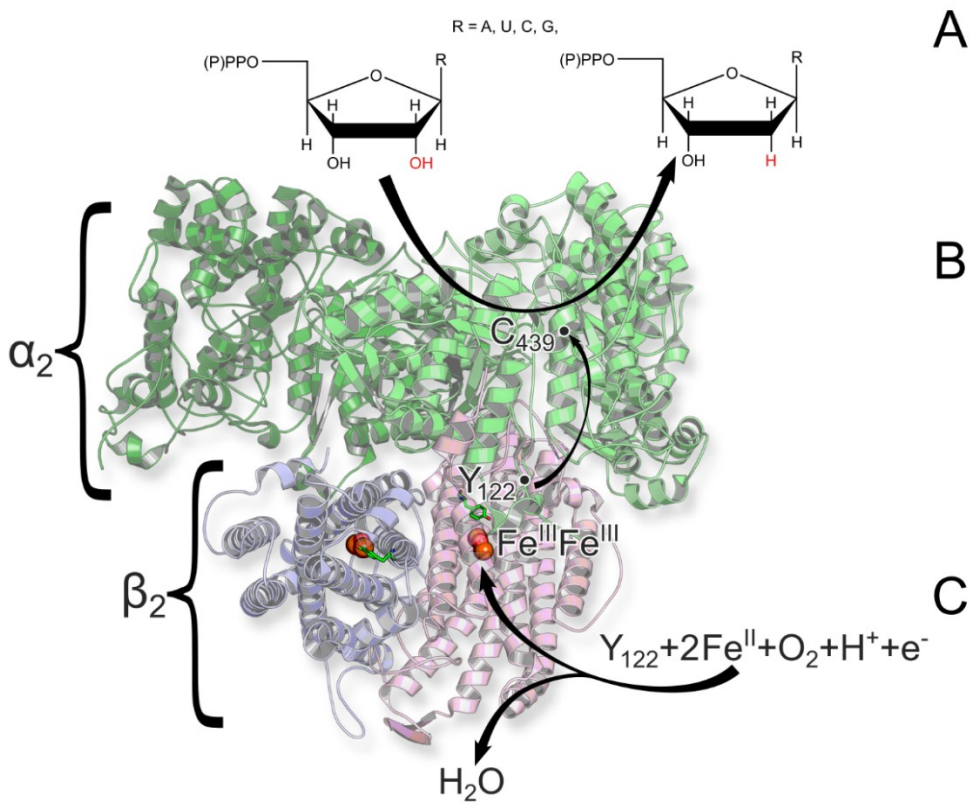

Figure 1: *E. Coli* RNR. **A**: Reduction of NDP/NTP to dNDP/dNTP. **B**: Cryo-electron microscopy structure of $\alpha_2\beta_2$ complex (6W4X).[55] **C**: Formation of β_2 metal cofactor.

However, instead of iron, β_2 can also bind manganese, leading to protein inactivation and preventing reductase activity. Furthermore, β_2 activity is limited to at most 60% active β_2 and at most 3.6 eq. (instead of the expected 4) of iron are bound, regardless of Fe^{2+} availability.[59,60] This makes the binding of manganese twice-fold interesting. First, it can serve as a model for iron binding, as both behave similarly. Unlike the di-iron cluster, which is virtually EPR silent, bound manganese can be detected via EPR.[61] The second point of interest is the competition between manganese and iron, and how, if at all, β_2 recovers from mismetallation. Extensive studies utilizing CW-spectroscopy to probe the binding behavior of manganese do exist.[62,63]

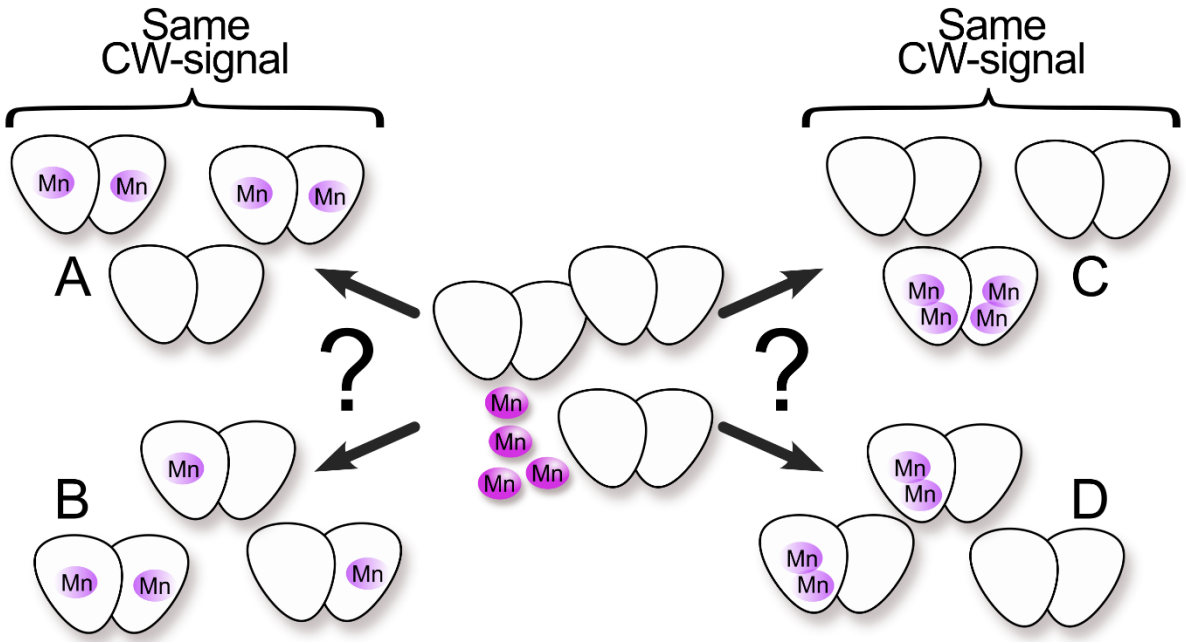

Figure 2: Illustration of different potential ways four Mn^{2+} could bind to three β_2-subunits. CW-spectroscopy only allows for the differentiation of A/B vs C/D, but not A vs B or C vs D.

However, CW-spectroscopy can only differentiate between free, mono-, and di-manganese (Figure 2). But, the binding situation in β_2 cannot be fully described by characterizing the local binding behavior within a single β subunit; a global description that examines the combined binding in both manganese binding sites and the distribution of tyrosyl radicals, if formed, is required. While no single method offers all this, by combining different dipolar spectroscopy approaches and field-sweeps, a much clearer picture of the metal binding behavior in β_2 can be generated.

1.2. GQ

Deoxyribonucleic acid (DNA) forms the backbone of all life, encoding the instructions each organism follows in its sequence of four nucleotides (adenine, thymine, cytosine, and guanine) and their modifications.[64] The most well-known secondary DNA structure is the antiparallel double helix from two complementary DNA strands. Here, the complementary nucleobases adenine and thymine, and cytosine and guanine, respectively, are paired through Watson-Crick base pairing.[65] It is this paired double-strand structure in which the sequence of nucleotides encodes for the sequence of amino acids that make up the different proteins a cell needs to produce. However, not all DNA exists to encode protein sequences, and not all DNA structures consist of two strands of Watson-Crick base pairs.

Perhaps the most prevalent example of DNA structures not made up of Watson-Crick pairs is guanine quadruplexes (GQ). GQs are a naturally occurring DNA structure formed from π-stacked tetrads of Hoogsteen-bonded guanines (Figure 4a). GQs can be found throughout all domains of life, with over 10k GQs confirmed to form in human cells, plus an additional 60k known sites capable of GQ formation.[66–69] Being present in virtually all functional regions of the human genome, they display their ability to stack on top of each other and form higher-order structures (Figure 3c).[70–74] This stacking is thought to have regulatory roles in gene

expression and telomere maintenance.[75–77] GQs have also been shown to be targeted by multiple drugs for treating different afflictions, ranging from malaria[78,79] to antitumor activity[80,81], and present a promising target for further drug development.[82–86] GQs have also found application as a structural motive in DNA nanotechnology.[87–89] Recently, a new copper label has been developed for GQs. [28,29,90] Thanks to both the labels and the GQs rigid structure, this made it possible to elucidate the structure of stacked GQs using high-precision DEER spectroscopy.[29] However, like most biological systems, GQ binding behavior is inherently dynamic.[91]

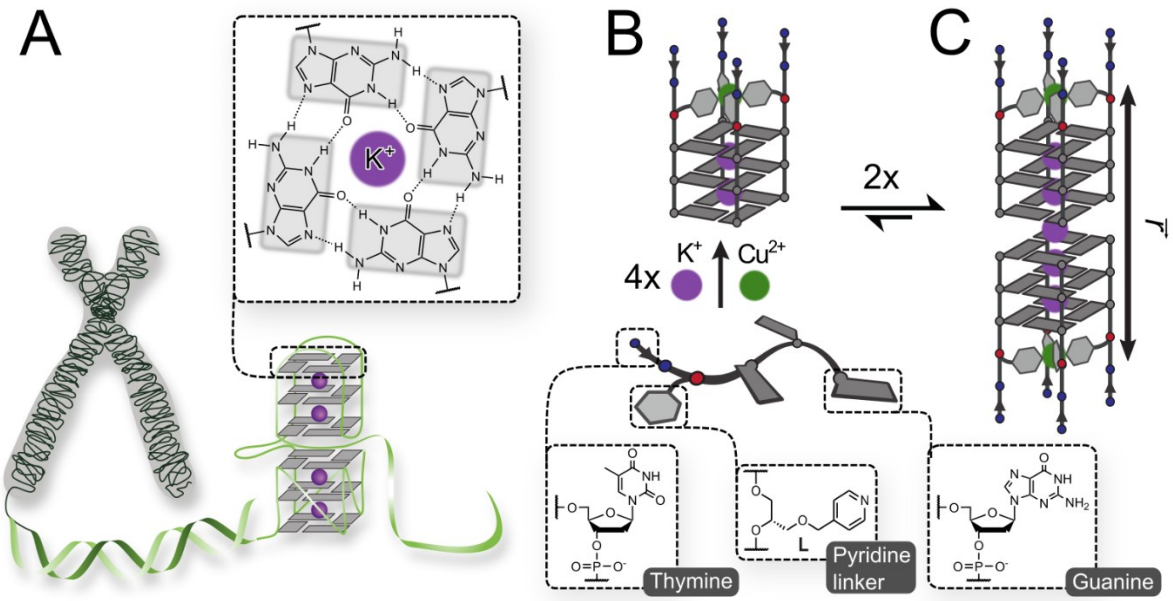

Figure 3: **A**: Schematic representation of a telomer with GQs in the telomeric region, and zoom in showing the binding mode of the guanine tetrad with Hoogsteen-base pairing. **B**: Exemplary oligonucleotide and its assembly into a tetramolecular GQ with copper label. **C**: Dimerization of GQs, with the distance between the Cu^{2+} measured in EPR indicated.

To effectively study the dynamics, quantitative methods are required that can distinguish species based on slight differences in distance of less than 0.3 nm. DEER spectroscopy possesses the necessary resolution and, in principle, is quantitative. However, due to the significant anisotropy of copper, the standard approach to quantitative DEER would require many measurements per sample[92] and be very time-consuming for copper-labeled GQs. Instead, a different approach utilizing the strong orientation selectivity associated with copper DEER measurements was developed to uncover distinct binding modes between GQs and intercalators.

2. Theoretical background

Electron paramagnetic resonance spectroscopy (EPR), also known as electron spin resonance spectroscopy (ESR), utilizes the interaction of electromagnetic waves to effect and detect the states of unpaired electrons in an externally applied magnetic field and draw conclusions about the nature of the electrons and their environment. It has found application in the study of inorganic, organic, and biological compounds, utilizing both naturally occurring radicals as well as artificially added spin labels. The following EPR theory is based on Harris&Wasylishen[93] Eaton et al.[30,94] Goldfarb&Stoll[95] Schweiger&Jeschke[96] unless cited differently.[a]

2.1. Basic EPR theory

EPR spectroscopy relies on electrons having spin angular momentum $\boldsymbol{S}$. Since electrons are also carry a charge, they have a magnetic moment $\boldsymbol{\mu}_\mathrm{e}$, which relates to $\boldsymbol{S}$ via the gyromagnetic ratio γ_e.

$$\boldsymbol{\mu}_\mathrm{e} = \gamma_\mathrm{e} \cdot \boldsymbol{S}. \tag{1}$$

The gyromagnetic ratio can be expressed in terms of the Bohr magneton μ_B, with the reduced plank constant $\hbar$ and the g-value of the free electron $g_\mathrm{e} \approx 2.002$.[97] Please note that different definitions varying in the signs used for g_e and γ_e exist in literature. This work uses the version where g_e is positive and γ_e is negative, as is common in EPR.

$$\gamma_\mathrm{e} = -\frac{g_\mathrm{e}\mu_\mathrm{B}}{\hbar}. \tag{2}$$

By definition, the external magnetic field in an EPR experiment is applied in the Z-direction. The Z-component of the magnetic moment μ_e is calculated as follows:

$$\mu_\mathrm{e} = -g_\mathrm{e}\mu_\mathrm{B} \cdot m_s. \tag{3}$$

Here, m_s is the spin magnetic quantum number, which can take any combination of sums and differences of the spin quantum numbers $\left(s = {}^1/_2\right)$ of all unpaired electrons, which make up a spin system. The total spin of a system is given as $S = \sum s_i$. As such the values for the spin magnetic quantum number can be expressed as $m_s = \text{-}S, \text{-}S + 1, \text{-}S + 2, \ldots, S$. For $S = {}^1/_2$ the $m_s = -{}^1/_2$ and $m_s = {}^1/_2$ states are typically referred to as 'spin down' and 'spin up' or β and

[a] Tensors and vectors are given in bold, operators by a circumflex

α. The energy E of the interaction between an external magnetic field B_0 and the electrons magnetic field is:

$$E = g_e \mu_B m_S B_0. \tag{4}$$

Therefore, the energy difference between two states with $\Delta m_s = \pm 1$ (allowed EPR transition) is given by:

$$\Delta E = g_e \mu_B B_0 = h\nu. \tag{5}$$

If irradiated with electromagnetic waves of frequency ν (Larmor frequency), transitions between the respective states can be excited. This is called the resonance condition (Figure 4).

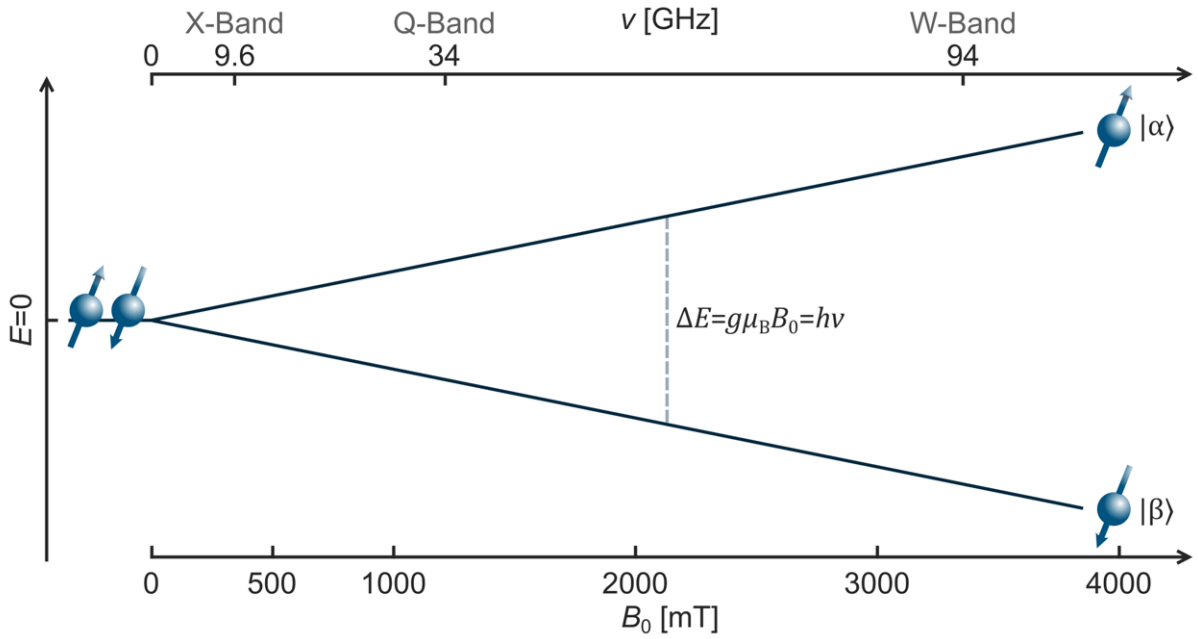

Figure 4: Illustration of Zeeman splitting as a function of magnetic field with common spectrometer frequencies for a free electron marked on the top.

Since transitions with $\Delta m_s = 1$ absorb one photon and transitions of $\Delta m_s = -1$ release a photon, only the difference between both transitions can be detected. For two-level systems, following the Boltzmann distribution, the polarization P, which quantifies the difference between the β and α population (n_β, n_α) can be expressed as:

$$P = \frac{n_\beta - n_\alpha}{n_\beta + n_\alpha} = \frac{1 - \exp\left(-\frac{\Delta E}{k_B T}\right)}{1 + \exp\left(-\frac{\Delta E}{k_B T}\right)}. \tag{6}$$

Therefore, EPR signal intensity scales with B_0 and scales inversely with the temperature T.

2.2. Spin Hamiltonian

The energy of an unpaired electron in a static magnetic field is described by the spin Hamiltonian $\hat{H}$ which can be separated into the following components:

$$\hat{H}(B) = \hat{H}_{EZ} + \hat{H}_{HF} + \hat{H}_{ZF} + \hat{H}_{EE} + \hat{H}_{NZ} + \hat{H}_{NQ}. \tag{7}$$

Of these $\widehat{H}_{\mathrm{NZ}}$ (nuclear Zeeman interaction) and $\widehat{H}_{\mathrm{NQ}}$ (nuclear quadrupole interaction) are not discussed here as they are not used in this work.

The electron Zeeman interaction $\widehat{H}_{\mathrm{EZ}}$ describes the interaction of the electron with the external magnetic field. It is the only field-dependent component of the used spin Hamiltonian.

$$\widehat{H}_{\mathrm{EZ}} = \mu_{\mathrm{B}} \boldsymbol{B}^{\mathrm{T}} \boldsymbol{g} \widehat{\boldsymbol{S}} \tag{8}$$

It is common practice to choose the reference frame for $\boldsymbol{g}$ in such a manner that $\boldsymbol{g}$ is a diagonal tensor and only the diagonal components of the tensor $(g_{\mathrm{x}}, g_{\mathrm{y}}, g_{\mathrm{z}})$ are given. In case the system displays axial symmetry (two of the g-values are equal) only $g_{\perp}$ and $g_{\parallel}$ are provided, and in case the system has no asymmetry only g_{iso} (often just written as g) is given. For a free electron in vacuum g equals g_{e}. However, in practice, interaction with the orbital angular momentum (**L**) will cause the g-value to deviate from g_{e}. While these deviations tend to be smaller in organic radicals, transition metals can reach quite large deviations. Since the electron Zeeman is the only field dependent term high frequency spectroscopy can be used to resolve smaller differences in g-value and g-anisotropy. On the other hand, low frequencies such as X-band can make spectra with small g-anisotropy effectively isotropic with respect to g. This can simplify the analysis of other features greatly.

The hyperfine interaction $\widehat{H}_{\mathrm{HF}}$ describes the interaction between the electron and close-by nuclei with a nuclear spin $I \neq 0$ as the magnetic field of the nucleus interacts with the electron on top of B_0:

$$\widehat{H}_{\mathrm{HF}} = h \cdot \widehat{\boldsymbol{S}}^{\mathrm{T}} \boldsymbol{A} \widehat{\boldsymbol{I}}. \tag{9}$$

While the hyperfine coupling tensor $\boldsymbol{A}$ does not have to be diagonalizable, it often is or is close enough that it can be treated as such. In that case, $\boldsymbol{A}$ is usually diagonalized and the same nomenclature as for $\boldsymbol{g}$ is used. If the eigenframes of $\boldsymbol{g}$ and $\boldsymbol{A}$ do not align, the Euler angles required for transformation into the g-frame are given as well.

The zero-field splitting (zfs) $\widehat{H}_{\mathrm{ZF}}$ term describes the interaction of multiple unpaired electrons within a spin center $(S > {}^1/_2)$ with each other:

$$\widehat{H}_{\mathrm{ZF}} = h \cdot \widehat{\boldsymbol{S}}^{\mathrm{T}} \boldsymbol{D} \widehat{\boldsymbol{S}}. \tag{10}$$

Since the eigenform of $\boldsymbol{D}$ is traceless $(D_{\mathrm{x}} + D_{\mathrm{y}} + D_{\mathrm{z}} = 0)$ it is often just written as:

$$D_{\mathrm{x}} = -\frac{1}{3}D + E, \quad D_{\mathrm{y}} = -\frac{1}{3}D - E, \quad D_{\mathrm{z}} = \frac{2}{3}D. \tag{11}$$

where D and E are the axial and rhombic components of the zfs.[98] While establishing quantitative relations is difficult, the magnitude of D and E are qualitatively linked to the local symmetry of the spin environment, with the zfs vanishing for symmetric environments.[99]

Finally, the electron-electron interaction is described through $\widehat{H}_{\mathrm{EE}}$:

$$\widehat{H}_{\mathrm{EE}} = h \cdot \widehat{\boldsymbol{S}}_{\boldsymbol{1}}^{\mathrm{T}} \boldsymbol{J} \widehat{\boldsymbol{S}}_{\boldsymbol{2}}. \tag{12}$$

This interaction becomes relevant if multiple electron spins are close enough to interact but not close enough to be treated as part of the same spin system. [100] The interaction can further

be split into the exchange coupling J, representing the isotropic part of $\boldsymbol{J}$, $\hat{H}_{\mathrm{dd}}$ representing the symmetric part (dipolar interaction) and the antisymmetric part (Dzyaloshinskii–Moriya interaction), which tends to be too weak compared to the other terms to be of consequence in this work.[101] There are multiple definitions of J varying in factor and sign, this work uses $+J\widehat{\boldsymbol{S}}_{\boldsymbol{1}}^{\mathrm{T}}\widehat{\boldsymbol{S}}_{\boldsymbol{2}}$ in line with how it is used in EasySpin.

2.3. CW-spectroscopy

Continuous wave (CW) spectroscopy presents the conceptually simplest of EPR methods. It works by continuously irradiating the sample with a constant frequency while sweeping the magnetic field, recording the absorption. For each field position, the magnetic field is modulated quickly (Figure 5). By modulating the field position, the recorded signal is also modulated. As long as the spectrum is approximately linear over the modulated range, the amplitude of the recorded sine-wave scales with the slope of the spectrum. Recording the spectrum this way has the advantage that the phase and frequency of the recorded signal are the same as those of the field modulation. Therefore, other interfering signals that do not have the same phase and frequency can be filtered out. Additionally, field modulation also serves as a kind of filter function, as features narrower than the modulation amplitude are broadened and reduced in intensity.[30] Therefore, small fluctuations in the signal stemming from noise are suppressed. Another practical advantage of displaying a spectrum as a first derivative stems from the fact that many significant features of an EPR spectrum, such as, for example, g_x and g_z in rhombic species, are marked by inflection points, which in the first derivative become turning points, making immediate identification by eye easier. For this reason, even EPR spectra recorded as absorption spectra are often displayed as "pseudo-modulated" spectra where field modulation is added to the recorded data in postprocessing. This can also serve to highlight broad features against narrow features and vice versa.

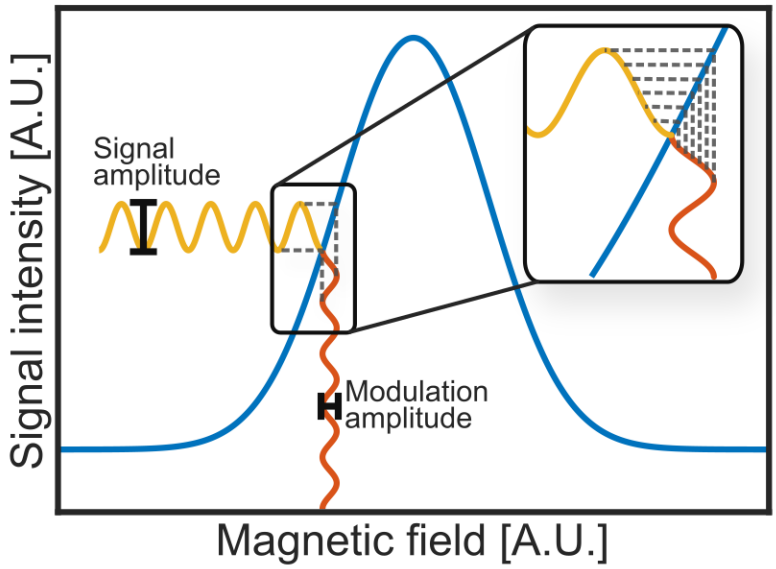

Figure 5: Schematic representation of field modulation in CW EPR, with the orange signal representing the field modulation and the yellow signal representing the generated signal. The insert shows how multiple time points in the field modulation correspond to time points in the signal modulation.

To induce an EPR transition, only the magnetic part of the microwaves is required. On the other hand, the electrical part of the electromagnetic wave only induces sample heating, which is not desired. To maximize signal and minimize heating, most EPR spectrometers utilize a resonator. Resonators have a frequency-dependent profile of how much microwave energy is reflected by the resonator. This profile is called the dip. In CW, the resonator is critically coupled, referring to the resonator mode where the dip is as deep and narrow as possible. The spectrometer frequency is then set to match the frequency of the dip. The performance of a resonator is quantified by the Q-factor:

$$Q = \frac{2\pi(\text{Energy stored})}{\text{Energy dissipated per cycle}} \approx \frac{\nu_{\text{res}}}{\text{Resonator bandwidth}}. \tag{13}$$

2.4. Pulse spectroscopy

The other arguably broader method is pulsed EPR spectroscopy. Here, short microwave pulses are applied to manipulate the bulk magnetization of the sample. When exposed to an external magnetic field, the bulk magnetic moment precedes about $\boldsymbol{B_0}$ at the Larmor frequency (Figure 6a). When adding a microwave pulse, the precession happens about the combined external field and field of the pulse. To simplify the picture, a rotating frame, revolving around the Z-axis at the spectrometer frequency, is used (Figure 6b). If the spectrometer frequency matches the Larmor frequency, $\boldsymbol{B_0}$ vanishes and the magnetization precedes about the magnetic field of the pulse in the rotating frame ($\boldsymbol{B_1}$) (Figure 6c-d).

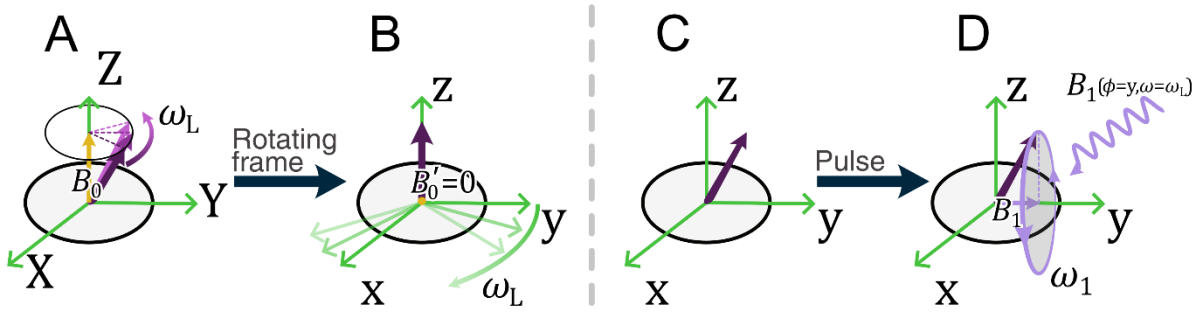

Figure 6: **A**: Larmor precession of magnetic moment in static external magnetic field B_0. **B**: Same picture but in rotating frame.[a] The magnetization is static and the external magnetic field $B_0 \xrightarrow{\text{Rot. frame}} B_0' = 0$ vanishes.[102] **C**: Spin in rotating frame. **D**: Application of microwave pulse. The spin starts to rotate around the phase direction of the pulse counterclockwise at the Rabi frequency.

The rate at which the magnetization is rotated is given by the Rabi frequency ω_1:

$$\omega_1 = \gamma B_1 \sqrt{S(S+1) - m_{s,1} \cdot m_{s,2}}. \tag{14}$$

For $S = {}^1/_2$ systems the expression simplifies to $\omega_1 = \gamma B_1$ since $m_{s,1} \rightarrow m_{s,2} = -{}^1/_2 \rightarrow {}^1/_2$ is the only possible transition. For $S > {}^1/_2$, ω_1 depends on the excited transition. Furthermore, the equation only works for systems where the states are well separated (zfs >> pulse bandwidth).[102–105] Since pulses have a nonzero bandwidth, each pulse will not only affect the spins where the spectrometer frequency exactly matches the Larmor frequency but also spins with close-by Larmor frequencies. By dividing spins with the same properties (Larmor frequency, interactions, experienced relaxation events…) into spin packages, one can look at how a group of dissimilar spins evolves over time. In the simple case where a group of spin packages, with Larmor frequencies that differ from the spectrometer frequency by $\Omega_i = \omega_{\text{Larmor},i} - \omega_{\text{Spectrometer}}$, evolve in the xy-plane over time, they will diphase (Figure 7c-d).

[a] Static frames are indicated by using upper case letters (XYZ), rotating frames by using lower case letters (xyz)

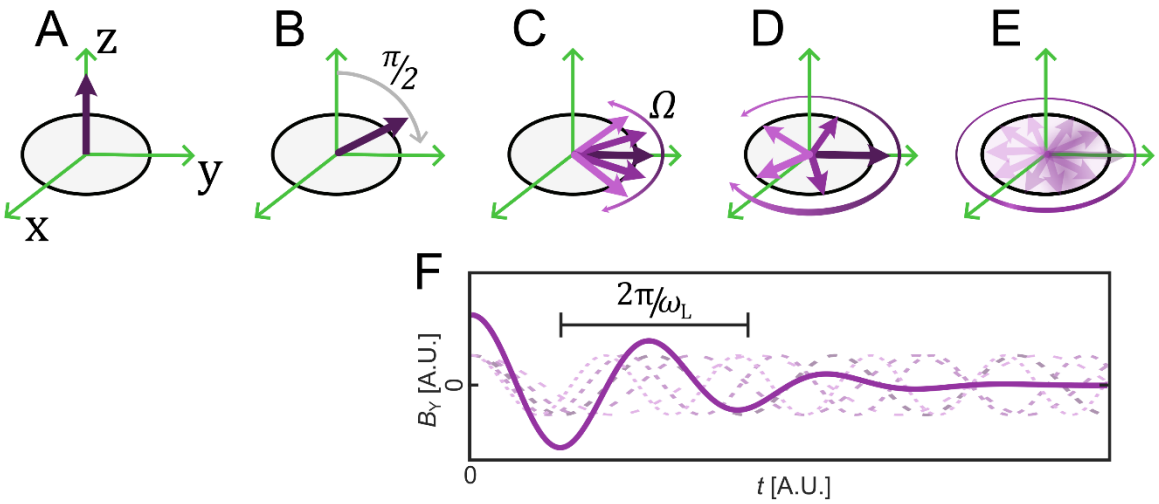

Figure 7: **A**-**E**: FID (free induction decay) following $\pi/2$-pulse flipping the magnetization onto the xy-plane. The dark purple spin package ω_{Larmor} matches the spectrometer frequency. The brighter the spin package is colored, the larger the offset from the spectrometer frequency. As the spin packages evolve the **F**: The resulting magnetization along the Y-axis as the spin packets dephase. The bold, continuous line represents the bulk magnetization. The dashed lines represent the magnetization of different isolated spin packages.

In principle, flipping the entire spectrum in the xy-plane and taking the Fourier transform of the resulting signal would enable the recording of the entire frequency-dependent EPR spectrum in a single shot (Figure 7).[106] This method of recording the FID (free induction decay) is popular in NMR (nuclear magnetic resonance) where the same principles of EPR are applied to nuclei. However, in EPR this detection method is rarely feasible. Compared to NMR, EPR experiments happen at orders of magnitude faster timescales and at higher and broader frequency ranges. Therefore, generating pulses with sufficient bandwidth to cover the entire spectrum is rarely possible. Furthermore, every pulse is followed by so-called "ring-down".[106] This describes the period where the energy of a pulse disperses from the spectrometer. Since the pulses are orders of magnitude stronger than the detected signal, detection during ring-down is not possible. Ringdown can be reduced by overcoupling the resonator, which lowers the Q-value and increases the bandwidth of the resonator compared to critical coupling. Still, between the faster relaxation and broader frequency range of EPR, the signal usually dephases completely by the time ring-down allows for detection. To circumvent this issue, Hahn-echo sequences are employed for detection.[107]

2.4.1. Hahn-echo

The Hahn-echo sequence is the standard pulse method to record field-swept spectra (Figure 8).[33] Starting with magnetization on the z-axis (Figure 8a) a $^{\pi}/_{2}$ is used to flip the magnetization into the xy-plane (Figure 8b). Afterwards, the magnetization will spread out (Figure 8c) as their Larmor frequency differs from the spectrometer frequency by $\omega_{\mathrm{Larmor}} - \omega_{\mathrm{Spectrometer}} = \Omega$. During this time, the respective spin packets gain a phase of $\tau\Omega$. Next, the spin is refocused by a π-pulse (Figure 8d). This turns the acquired phase from $\tau\Omega$ to $\pi - \tau\Omega$ (π pulse along the same axis as $^{\pi}/_{2}$-pulse) or $-\tau\Omega$ (π pulse along different axis as $^{\pi}/_{2}$-pulse). As the spins evolve for another period of τ the spin packages accumulate an additional phase of $\tau\Omega$ (Figure 8e).

Finally, the spin packages run back together, resulting in an "echo" of the magnetization after the initial pulse (Figure 8f).

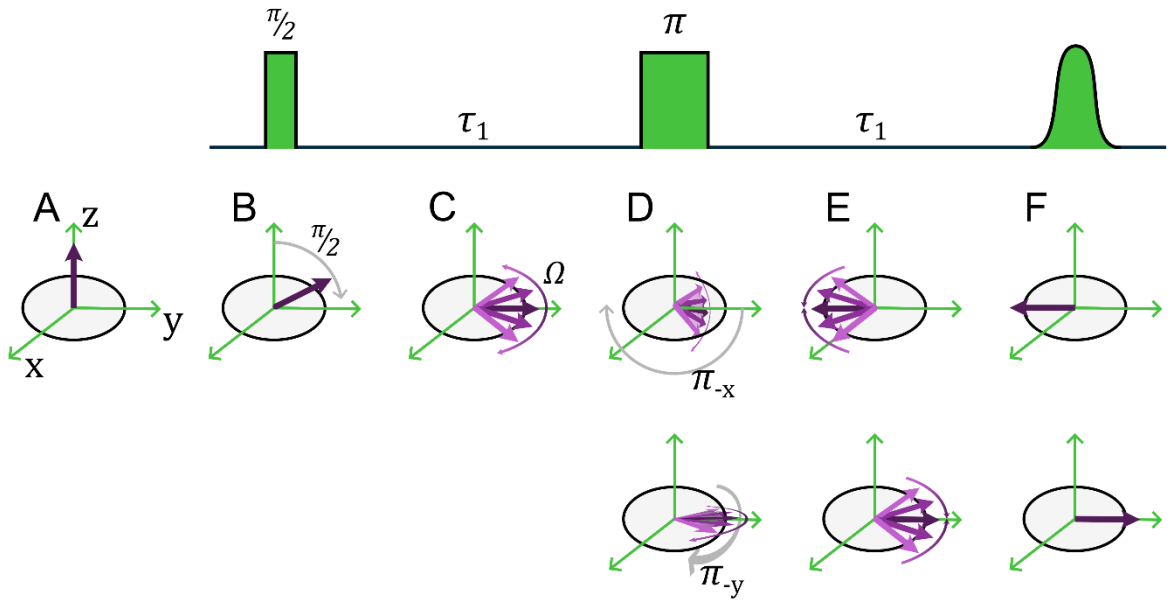

Figure 8: Different stages of a Hahn-echo signal detection. Pulse sequence on top, magnetization in rotating frame at the bottom. The pulses are -x pulses. Alternatively, to using a π_{-x} the use of a π_{-y} is shown in the bottom row.

The effective contribution to the total phase of a signal after n π-pulses, which evolve for a period of t_n, following each pulse can be generalised to be:

$$\phi_n = \Omega \cdot t_n \cdot (-1)^{n_{\text{total}}-n}. \tag{15}$$

With each π-pulse of phase $\phi_{\pi,n}$, an additional phase contribution of:

$$2\phi_{\pi,n}(-1)^{n_{\text{total}}-n}. \tag{16}$$

is added. This leads to the signal refocusing at a phase of:

$$\left(\phi_{\pi/2} - \frac{\pi}{2}\right)(-1)^{n_{\text{total}}} \sum 2\phi_{\pi,n}(-1)^{n_{\text{total}}-n}. \tag{17}$$

Most pulse detection schemes in EPR rely on spin echoes created through refocusing.

2.4.2. T_1/T_2 relaxation

So far, relaxation processes have been ignored. Two major relaxation processes are involved in EPR measurements. Spin lattice relaxation (T_1) describes the return of the magnetization to equilibrium along the z-axis and forms the slower of the relaxation processes.[34] It is the process that is responsible for resetting the spin system between shots. Spin-spin relaxation (T_2) is caused by spins interacting with each other during evolution, resulting in changes in Ω during evolution. This prevents the spins from entirely refocusing, degrading the echo strength. Therefore, T_1 limits how rapidly a pulsed experiment can be repeated and T_2 limits how long a pulse sequence can become.

T_1 measurements are usually performed with inversion recovery measurements (Figure 9).[107] Here, the magnetization is inverted with a π pulse followed by a Hahn-echo sequence. As the

Hahn-echo is moved backwards the spins have more time to relax back to equilibrium magnetization, resulting in a return of the normal echo. The signal $I(t)$ is fitted to an exponential to determine T_1.

$$I(t) = I_0\left(1 - 2 \cdot \exp\left(-(t \cdot T_1^{-1})^{\beta}\right)\right) \tag{18}$$

Sometimes an additional stretch factor β, ranging from 0 to 1, is introduced. This factor does not directly correspond to any physical property and arises for distributions of T_1 with $\beta = 1$ corresponding to a single T_1 with no distribution.[108]

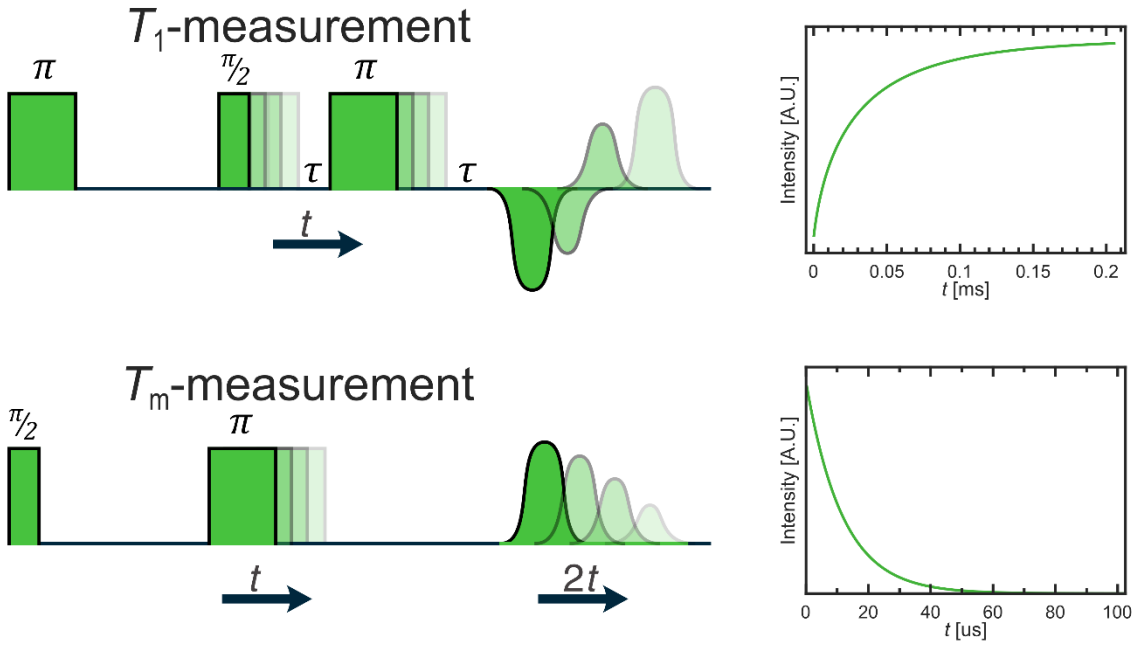

Figure 9: Schematic T_m and T_1 measurements on the left and exemplary resulting signals on the right.

The standard pulse method for determining T_2 consists of recording Hahn-echos with increasing τ (Figure 9). [107] Since T_1-relaxation still takes place on top of T_2-relaxation, the measured relaxation rate is technically the phase memory time T_m, not T_2. However, since T_1 tends to be much longer than T_2, T_m and T_2 are often taken to be equivalent. Just as with T_1 a stretch factor can be introduced to better fit T_2 distributions:

$$I(t) = I_0 \exp\left(-(2t \cdot T_m^{-1})^{\beta}\right) \tag{19}$$

2.5. Dipolar spectroscopy

Dipolar spectroscopy presents a group of advanced pulse EPR experiments primarily designed to leverage the dipolar interaction between a so-called A and B spin to determine the distance between the two spins.[109]

While single-resonance techniques, such as SIFTER (single frequency technique for refocusing dipolar couplings)[110] and DQC (double-quantum coherence)[111] Existing, the double-resonance

DEER (dipolar electron-electron resonance)[112,113] and the closely related single-frequency technique RIDME (relaxation-induced modulation enhancement)[114] are the most widely used dipolar spectroscopy techniques (Figure 10).[112,115]

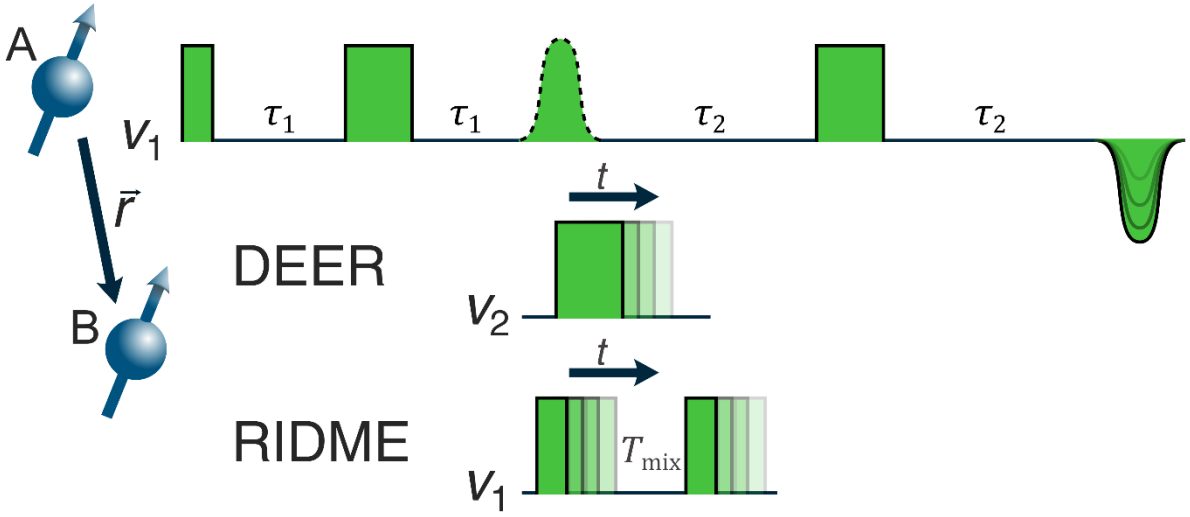

Figure 10: 4-pulse DEER / 5-pulse RIDME. The top row displays the detection sequence forming a refocused Hahn-echo. The second and third rows show the B-spin inversion events for DEER and RIDME, respectively. The DEER inversion event is a π-pulse acting at a second frequency, referred to as the pump pulse. For RIDME the A-spin is flipped out of the xy-plane by a $\pi/2$ effectively storing it as a gradient along the z-axis before flipping it back onto the xy-plane after the mixing time T_{mix}. The B-spin is flipped by T_1 relaxation processes.

They both follow the same underlying principle, detecting the echo of an A-spin while flipping the B-spin at different points in time. While DEER uses a pump-pulse at a second frequency to invert the B-spin, RIDME utilizes a mixing block. The mixing block contains of two $\pi/2$-pulses where the first pulse flips the A-spin back onto the z-axis effectively storing the current magnetization in a gradient along the z-axis. The second $\pi/2$-pulse then flips the magnetization back into the xy-plane. Since T_2-relaxation is in practice suspended between the pulses, the mixing block can be made quite long. This gives the B-spin a chance to flip on its own due to T_1-relaxation processes, regardless of where the B-spin is on the EPR spectrum.[114] Since B-spins that undergo an even number of spin flips just end up where they started, only B-spins with an odd number of spin flips contribute to the modulation. The probability for a B-spin to undergo an odd number of flips (P_{odd}) during the mixing block, based on the spin of B-spin (S_{B}) can therefore be described as:[114]

$$P_{\mathrm{odd}} = \left(1 - \exp\left(-\frac{T_{\mathrm{mix}}}{T_{1,\mathrm{B}}}\right)\right) \cdot \frac{2S_{\mathrm{B}}}{2S_{\mathrm{B}} + 1}. \tag{20}$$

Therefore, if T_{mix} is sufficiently larger than $T_{1,\mathrm{B}}$, P_{odd} approaches $\frac{2S_{\mathrm{B}}}{2S_{\mathrm{B}}+1}$ which for the most common case of $S = 1/2$ equals 0.5.

Without inversion of the B-spin, the dipolar contribution to the evolution of the A-spin is constant and therefore refocused fully with all other contributions $\frac{\omega_{\mathrm{dd}}}{2}(\tau_1 + \tau_2) - \frac{\omega_{\mathrm{dd}}}{2}(\tau_1 + \tau_2) = 0$ (Table 1). With the B-spin flipped, the dipolar contribution is no longer fully refocused $\frac{\omega_{\mathrm{dd}}}{2}(\tau_1 + t + \tau_2) - \frac{\omega_{\mathrm{dd}}}{2}(\tau_1 + \tau_2 - t) = \omega_{\mathrm{dd}} \cdot t$.

Table 1: Evolution of an A-spin during a 4-pulse DEER sequence. The sequence with and without pumping the B-spin is shown. For both sequences, the states of the A and B spins during each evolution period are given, as well the phase the spin packets pick up during each evolution period. The sign of the phase contribution is given as the effective phase after all π-pulses have taken effect (eq. (15)). For the echo, the sum of all contributions during the sequence is given. In both scenarios, a second sequence, where the B-spin starts off as α can be constructed. This case leads to an inversion of the sign of the dipolar contribution. Since DEER and RIDME are not sensitive to the sign of the dipolar contribution, both pathways lead to the same signal.

Pump pulse off

	$\pi/2$	τ_1	π	τ_1	(p)	τ_2	π	τ_2	Echo
Observer coherence & B-spin state		$-\ \beta$		$+\ \beta$			$-\ \beta$		
Accumulated phase		$+\Omega \cdot \tau_1$ $-\frac{\omega_{dd}}{2} \cdot \tau_1$		$-\Omega \cdot (\tau_1 + \tau_2)$ $+\frac{\omega_{dd}}{2} \cdot (\tau_1 + \tau_2)$			$+\Omega \cdot \tau_2$ $-\frac{\omega_{dd}}{2} \cdot \tau_2$		$+\Omega \cdot 0$ $+\omega_{dd} \cdot 0$

Pump pulse on

	$\pi/2$	τ_1	π	$\tau_1 + t$	p	$\tau_2 - t$	π	τ_2	Echo
Observer coherence & B-spin state		$-\ \beta$		$+\ \beta$		$+\ \alpha$		$-\ \alpha$	
Accumulated phase		$+\Omega \cdot \tau_1$ $-\frac{\omega_{dd}}{2} \cdot \tau_1$		$-\Omega \cdot (\tau_1 + t)$ $+\frac{\omega_{dd}}{2} \cdot (\tau_1 + t)$		$-\Omega \cdot (\tau_2 - t)$ $-\frac{\omega_{dd}}{2} \cdot (\tau_2 - t)$		$+\Omega \cdot \tau_2$ $+\frac{\omega_{dd}}{2} \cdot \tau_2$	$+\Omega \cdot 0$ $+\omega_{dd} \cdot t$

The resulting signal V of a single A-spin, with the electron-electron interaction frequencies ω_{AB} for all B-spins, which were inverted in the entire sample, is given by:

$$V_A(t) = \prod_{B_{inverted}} \cos(\omega_{AB} t). \tag{21}$$

In practice, the signal can be separated into an intramolecular part $F(t)$ and an intermolecular part $B(t)$:

$$V(t) = F(t) \cdot B(t). \tag{22}$$

The intermolecular part (Background) includes all the low-frequency long-range interactions, which average out to create an exponential background:

$$B(t) = \exp\left(-\frac{2\pi\gamma_A\gamma_B\mu_0}{9\sqrt{3}\hbar} c\lambda_B t^{\frac{D}{3}}\right). \tag{23}$$

Here, c is the sample concentration, λ_B the inversion efficiency and D the dimensionality associated with the spin center distribution.[37,116–118] A dimensionality of 2 would correspond to a sample where all spin centers are in a plane, such as on a protein layer. Most common is $D = 3$ which corresponds to a random distribution in solution. Higher dimensionalities technically don't directly correspond to any physical dimensionality; however, can occur if other effects contribute to the background or if the distances aren't equally distributed. For example, in samples with exclusion volumes, small distances are underrepresented, leading to dimensionalities of up to 6.[119] The background function for RIDME is more complicated and beyond the scope of this work.[120,121]

The intramolecular signal for all A-spins can be derived from equation (21) by considering only B-spins in the same object as the A-spins:

$$F(t) = \frac{1}{n}\langle \sum_{A=1}^{n} \prod_{\substack{B=1 \\ B\neq A}}^{n} \left(\lambda_B \cos(\omega_{AB} t) + (1-\lambda_B)\right)\rangle \tag{24}$$

Since only a fraction of B-spins is inverted, the interaction term for the B-spin is the inversion efficiency (λ_B) weighted sum of $\cos(\omega_{AB}t)$ (case that the specific B-spin was inverted) and 1 (case that B-spin was not inverted). The observed electron-electron interaction is the sum of the exchange coupling J_{AB} and dipolar interaction ω_{dd}.

$$\omega_{AB} = \omega_{dd} + 2\pi J_{AB} \tag{25}$$

Within the weak coupling regime, it can be possible to detangle ν_{dd} and J_{AB}, however, most DEER measurements are taken in conditions where exchange coupling is negligible.[122,123]

This leaves the distant dependent dipolar interaction:[124,125]

$$\hat{H}_{dd} = \frac{\mu_0 \mu_B^2 g_{A,eff} g_{B,eff}}{4\pi h r^3} \cdot \left[\hat{A} + \hat{B} + \hat{C} + \hat{D} + \hat{E} + \hat{F}\right]. \tag{26}$$

Of these terms $\hat{C}$-$\hat{F}$ can be ignored in the high field approximation (electron Zeeman $\gg \nu_{dd}$).

$$\begin{aligned} \hat{A} &= \hat{S}_{z,A}\hat{S}_{z,B}\left(1 - 3\cos^2(\theta)\right) \\ \hat{B} &= -\frac{1}{4}\left(\hat{S}_A^+ \hat{S}_B^- + \hat{S}_A^- \hat{S}_B^+\right)\left(1 - 3\cos^2(\theta)\right) \end{aligned} \tag{27}$$

The pseudo-secular term $\hat{B}$ can also be dropped if the difference between the Zeeman frequencies of A- and B-spin is much larger than ν_{dd}. Since pump and detect pulse need to be well separated in DEER experiments anyway, this is usually given in DEER experiments. However, in RIDME experiments, there is no B-spin selection; therefore, some overlap can occur, leading to spin flip-flops, which can reduce modulation depth.

This leaves the familiar expression for the dipolar frequency in DEER measurements:

$$\nu_{dd}(r,\theta) = \underbrace{\frac{\mu_0 \mu_B^2}{4\pi h}}_{\text{Constant}} \cdot \underbrace{g_{A,\text{eff}} g_{B,\text{eff}}}_{\substack{\text{Constant for} \\ \text{given experiment}}} \cdot \underbrace{r^{-3}}_{\text{Distance}} \cdot \underbrace{\left(1 - 3\cos^2(\theta)\right)}_{\text{Orientation}}. \tag{28}$$

With the first term being constant and the second term also being constant for any given experiment ν_{dd} only depends on the distance of the spins to each other and the angle θ between the magnetic field and the interspin vector $\vec{r}$ (Figure 11).

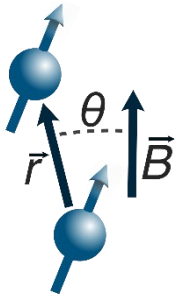

Figure 11: Angle θ between the interspin vector $\vec{r}$ and external magnetic field $\vec{B}$.

The angle-dependent part of ν_{dd} can take values in the range of -2 for $\theta = 0°$ to 1 for $\theta = 90°$. When summing up the respective ν_{dd} for all possible orientations, the characteristic "Pake-pattern" is generated (Figure 12).[126] The Pake pattern displays two peaks at $\pm\nu_{dd}$ respectively and shoulders running to $\mp 2\nu_{dd}$.

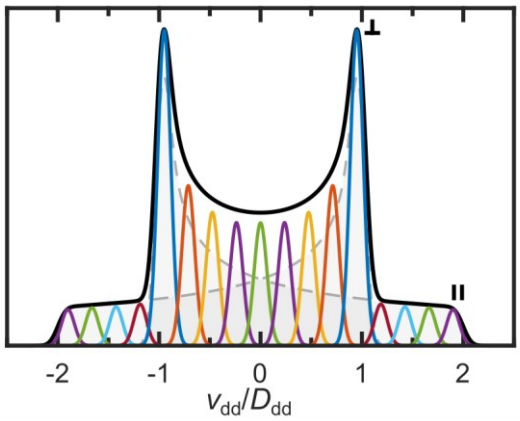

Figure 12: Exemplary Pake pattern with the dipolar frequency normalized to the dipolar frequency at $\theta = 90°$ (D_{dd}). The black line describes a Pake pattern in the case of no orientation selection as a result of summing over all orientations (indicated by the colored lines). Since DEER is not sign-sensitive, the resulting spectra is the sum of itself and its mirror image. The dashed lines indicate the shape expected with sign-sensitive detection. The dipolar frequencies for $\theta = 90°$ ($\perp$) and $\theta = 0°$ ($\parallel$) are indicated.

2.5.1. Orientation selection

To extract the distance from ν_{dd} one of two cases needs to be satisfied. In the first case the distribution of measured θ is known for the given measurement leaving r as the only variable to solve for. In practice, knowing θ *ab initio* is rarely possible and a combination of multiple measurements and sufficient knowledge of the EPR parameters to simulate the EPR spectrum are required to solve for both r and θ at the same time.[124] The second option is to measure orientation-averaged DEER. Here, all orientations are sampled, either in a single measurement or through the summing of multiple measurements. Since the shape of the resulting dipolar frequency distribution is known (Pake pattern), only the distance distribution needs to be fitted. This approach is used by programs like DeerAnalyis.[117]

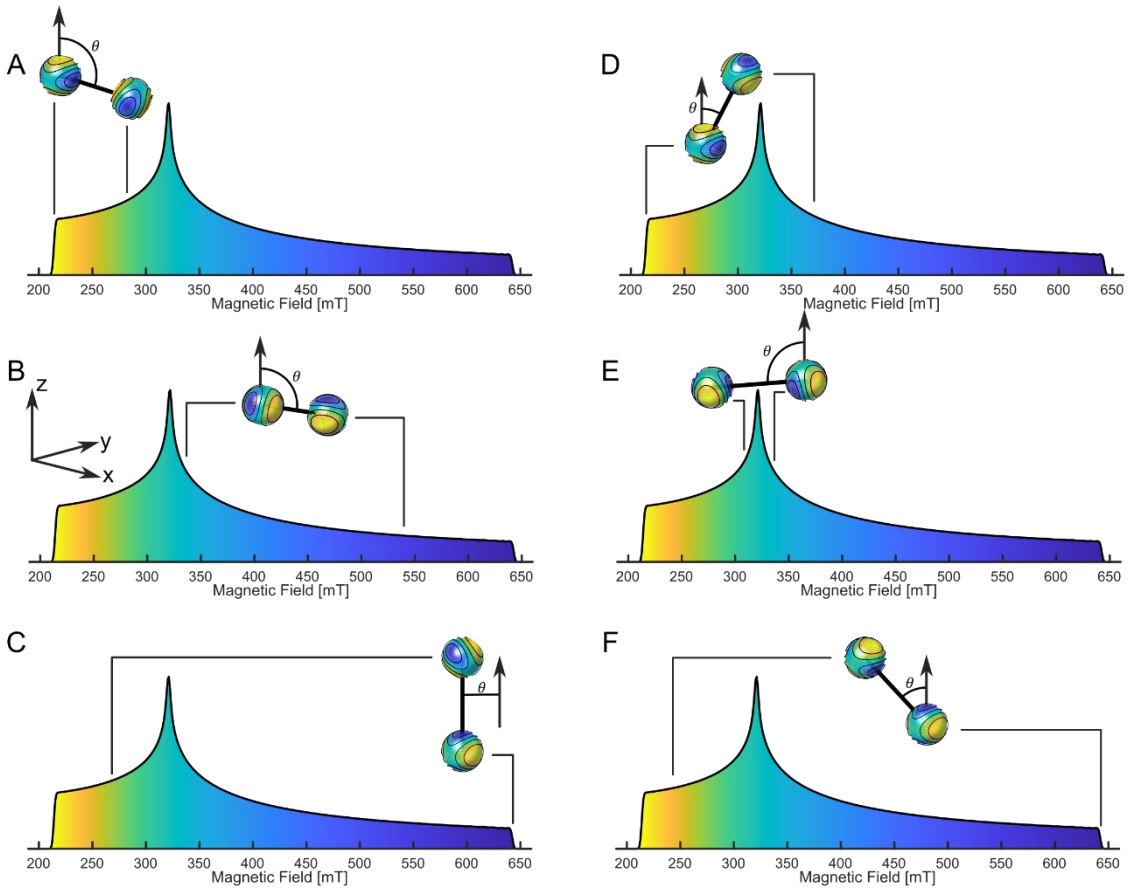

Figure 13: Schematic examples of orientation selection in DEER. The hypothetical system has $g = [1, 2, 3]$. Each subplot shows a the A- and B-spin as balls with the effective *g*-value for each orientation colored in (1=blue, 3=yellow) and the interspin vector. The field positions where the respective spins are found in the spectrum are indicated. The field sweep was simulated with the easyspin function pepper at 9 GHz and colored in according to their *g*-value. **A**-**C**: Interspin vector [0 0 *r*] rotated by the euler angles: [0, 90, 0]° (zxz-rotation). The B-spin is rotated by [35.26, 120.00, 54.74]°. **D**-**F**: Here, the interspin vector is rotated by [0, 30, -90]° B-spin is rotated by [0, 120, 0]°.

In practice, whether a DEER measurement is orientation selective depends on two conditions.[127] First, at least either A- or B-spin must have very little orientational freedom with respect to the molecule, linking the orientation of the restricted spin to the orientation of the interspin vector. Secondly, that restricted spin-center must display enough anisotropy that different positions on the EPR spectrum correspond to distinctly different orientations. In that case, positioning of the detect (restricted A-spin) / pump (restricted B-spin) selects a set of A/B-spin orientations, in turn selecting a set of θ. A visualization of how anisotropy in rigid samples creates orientation selection is given in Figure 13. The same rules apply to RIDME measurements. However, active selection on the B-spin, if possible at all, is not straightforward and often negligible. In practice, this leaves only the A-spin as a target for orientation selection. A quick flowchart for orientation selection is given in Table 2.

Table 2: Flowchart for checking if DEER/RIDME experiment can have orientation selectivity.[a]

	Rigid?	Anisotropic?	RIDME	DEER
A-spin	Yes	Yes	Orientation selection	Orientation selection
	Yes	No	No controlled orientation selection possible	Check B-spin
	No	Yes		
	No	No		
B-spin (if no A-spin selection)	Yes	Yes	If T_1 anisotropy & not $T_1 \ll T_{\mathrm{mix}}$	Orientation selection
	Yes	No	If T_1 anisotropy & not $T_1 \ll T_{\mathrm{mix}}$	No orientation selection possible
	No	Yes	No orientation selection possible	
	No	No		

2.5.2. Modulation depth and the effect of orientation selection on modulation depth

So far, the DEER signal has only been discussed in terms of the inversion efficiency λ_{B}, but in practice, not every A-spin shares a molecule with a B-spin. Furthermore, orientation selection can limit which B-spins are actually available. Therefore, the modulation depth parameter Δ is introduced, which describes the effective inversion efficiency in an experiment. Returning to equation (*24*), the $\cos(\omega_{\mathrm{AB}}t)$ containing terms will average out to 0 at long times as the respective contributions with different dipolar frequencies dephase. That only leaves $(1-\lambda_{\mathrm{B}})^{n-1}$, which turns into $\left(1-\lambda_{\mathrm{B,eff}}\right)^{n-1} = 1-\Delta$ for actual measurements (Figure 14). For $n = 2$, which is the most common situation where the modulation depth is analyzed, the dimer fraction is given by $\frac{\Delta}{\lambda_{\mathrm{B,eff}}}$.

[a] Please note that orientation selectivity is taken as a binary property for the sake of simplicity. In practice is makes more sense to discuss orientation selectivity in levels.

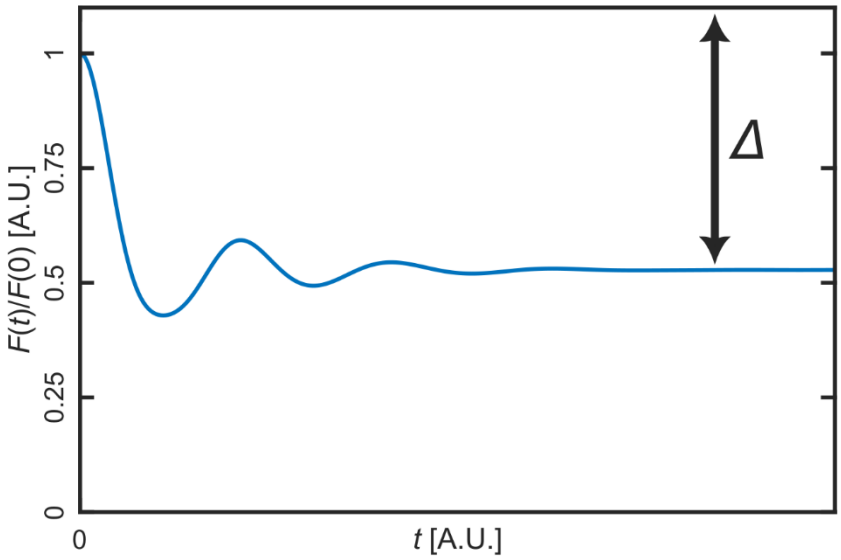

Figure 14: Example of background corrected DEER spectrum with the modulation depth Δ marked.

$\lambda_{\mathrm{B,eff}}$ depends on two main factors. First is the actual inversion efficiency λ_{B}, which depends on the pulse parameters, spectrometer, resonator, and Rabi-frequency of the sample. For RIDME P_{odd} provides the equivalent value. The other factor is orientation selection. To illustrate how orientation selection influences the modulation depth, the same hypothetical system from Figure 13 is examined again in Figure 15.

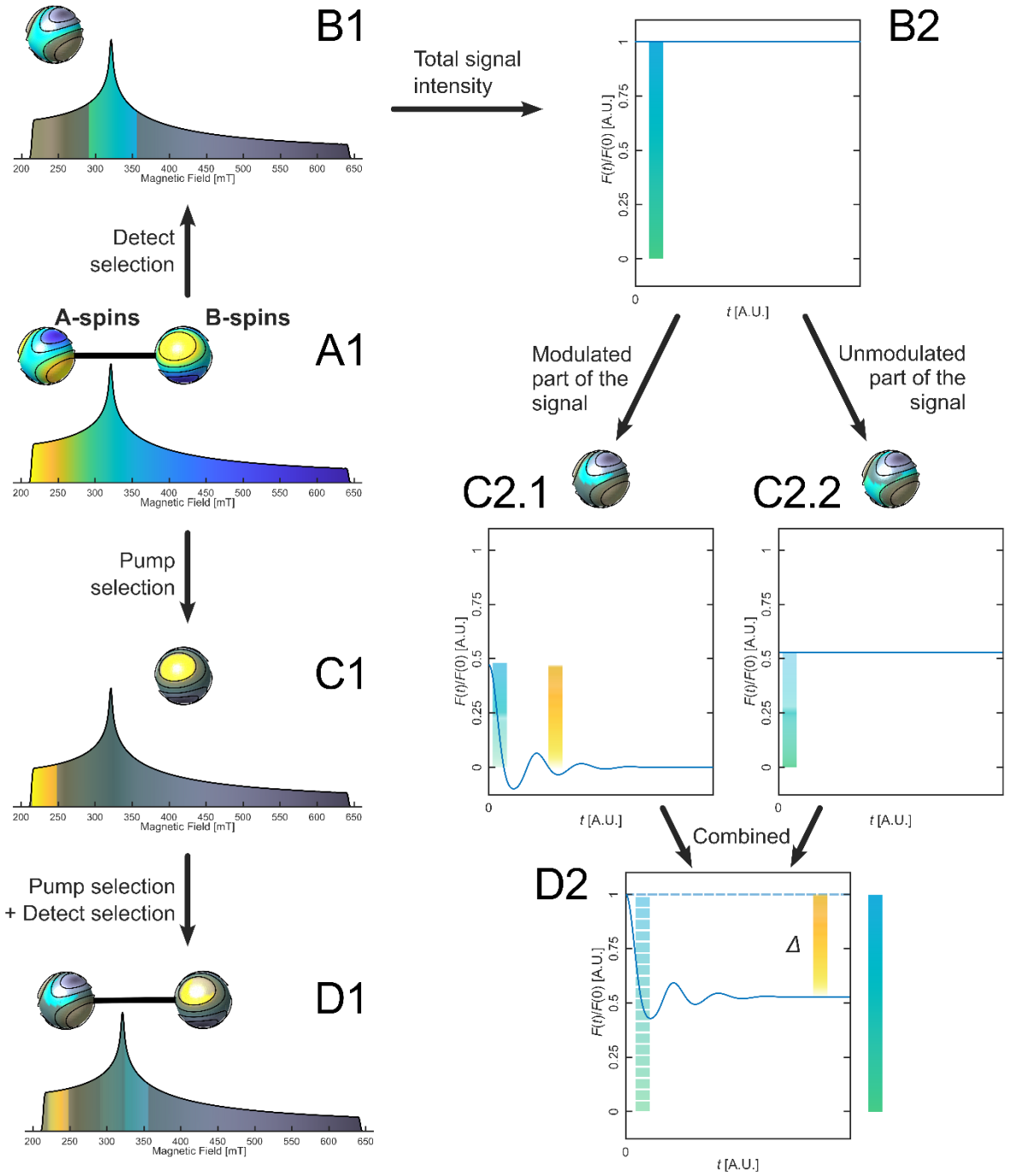

Figure 15: Orientation selection in DEER. **A1**: An example system with two identical spins and *g*-anisotropy $(g_{\mathrm{x,y,z}} = 1{,}2{,}3)$ (1=blue, 3=yellow). For the sake of the example, both spins are completely rigid and the spectrometer can generate perfect pulses that flip each spin in its bandwidth perfectly. **B1**: Selection of the A-spin based on the detection sequence. The spins not selected are greyed out. **B2**: The resulting signal from just the A-spin selection which determines the signal intensity at $t = 0$. **C1**: Selection of the B-spin based on the pump pulse. The spins not selected are greyed out. **C2.1-C2.2**: The A-spins from (B) separated into the fraction with pumped B-spins $\{A : A \in A_{\mathrm{d}} \text{ and } B \in B_{\mathrm{p}}\}$ and the fraction that does not have a pumped B-spin $\{A : A \in A_{\mathrm{d}} \text{ and } B \notin B_{\mathrm{p}}\}$. **D1**: Spin pairs that comprise the modulated part of the signal $AB_{\mathrm{mod}} = \{AB : A \in A_{\mathrm{d}} \text{ and } B \in B_{\mathrm{p}}\}$ as a result of the combined selection The amount the respective *g*-values are greyed out reflects the fraction of their spin pairs that contribute to the modulated part of the DEER trace. **D2**: The DEER signal that results from the sum of the modulated and unmodulated part of the DEER trace.

For this examination, a spectrometer that can perfectly flip all spins in a given frequency range is imagined ($\lambda_\mathrm{B} = 1$), and a sample where every A-spin has a corresponding B-spin. The sample would be a set of available spin pairs $\{AB_1, AB_2, \dots\} \cup \{BA_1, BA_2, \dots\} = \{(A_1, B_1), (A_2, B_2), \dots\} \cup \{(B_1, A_1), (B_2, A_2), \dots\}$ of the A and B-spin. Note that each spin pair is listed twice, as without specifying pump and detect position, both spins of each pair could act as either A- or B-spin. Furthermore, the assignment of A- and B-spin is only not arbitrary for spin pairs where at least one spin is selected for either pump or detect and neither spin is selected for both. For simplicity only (A, B) pairs are considered, but for completeness the same process would need to be repeated with the same (B, A) pairs.

By placing the detect frequency ν_d a fraction of all A-spins will be selected $A_\mathrm{d} = \{A : \nu(A) \in \nu_\mathrm{d}\}$ (Figure 15b1). This fraction determines the total signal intensity of the refocused echo (Figure 15b2). Next, the pump frequency ν_p, selects a fraction of B spins $B_\mathrm{p} = \{B : \nu(B) \in \nu_\mathrm{p}\}$ (Figure 15c1). Therefore, of all spin pairs only those where the A- and B-spin were selected contribute to the modulated signal $AB_\mathrm{mod} = \{AB : A \in A_\mathrm{d} \text{ and } B \in B_\mathrm{p}\}$ (Figure 15d1). As a result, the modulation depth is $\Delta = \frac{|AB_\mathrm{mod}|}{|A_\mathrm{d}|}$ (Figure 15c2-d2). To connect this with orientation selection a number is assigned to each orientation O and grouping spins by their orientation rather than just referring to them by counting the spins. For the extremer case of a completely rigid system where the g-frames of both spins align this results in the same set of spins $AB = \{(A_{O=1}, B_{O=1}), (A_{O=2}, B_{O=2}), \dots\}$ as before or the same case with reordered indexes in case the g-frames do not align $AB = \{(A_{O=1}, B_{O=7}), (A_{O=2}, B_{O=5}), \dots\}$. However, for the other extreme case of either spin being able to revolve freely relative to the system, the selection is $AB = \{(A_{O=1}, B_{O=1}), (A_{O=1}, B_{O=2}), (A_{O=1}, B_{O=3}), \dots, (A_{O=2}, B_{O=1}), (A_{O=2}, B_{O=2}), (A_{O=2}, B_{O=3}), \dots\}$, so each respective orientation of A-spins contains pairs with every orientation of B-spins. In this case the modulation depth is independent of the detect selection and only depends on the fraction of B-spins which is pumped: $\Delta = \frac{|AB_\mathrm{mod}|}{|A_\mathrm{d}|} = \frac{|B_{O,\mathrm{p}}|}{|B_O|}$. On the other hand, in the rigid case the modulation depth depends on the relative orientation of the B-spin to the A-spin. For this case $B_{O,\mathrm{d}} = \{B_O : A_O \in A_{O,\mathrm{d}}\}$ can be defined as all the B-spins which have a corresponding A-spin which is detected. Therefore, the modulation depth can be expressed as $\Delta = \frac{|AB_\mathrm{mod}|}{|A_\mathrm{d}|} = \frac{|B_{O,\mathrm{p}} \cap B_{O,\mathrm{d}}|}{|B_{O,\mathrm{d}}|}$. Please note that this means orientation selection occurs in the sense of being able to select subsets of θ and in the sense of modulation depth having an orientation-dependent component are not necessarily the same (Table 3).

Table 3: Overview of which combinations of A and B-spin orientation selection result in orientation selection on θ and Δ respectively.

A-spin orientation-selection	B-spin orientation-selection	θ orientation dependent	Δ orientation dependent
Yes	Yes	Yes	Yes
Yes	No	Yes	No (depends on fraction of spectrum pumped)
No	Yes	Yes	No (depends on fraction of spectrum pumped)
No	No	No	No (depends on fraction of spectrum pumped)

3.
Guanine Quadruplexes

While double-stranded helices are the most well-known form of DNA, there are other naturally occurring structures, with guanine quadruplexes presenting the possibly most important of these classes.[71,73] Guanine quadruplexes are found in guanine-rich sections of DNA, where four guanines form π-stacked tetrads based on Hoogsteen-binding.[128] GQs have been found to play regulatory roles in gene expression and are, for example, commonly found in telomeres.[91] Furthermore, GQs are of great interest as structural building blocks in DNA nanotechnology. Their ability to form very rigid higher-order structures to create multimers like G-wires[129,130] make them a popular motif. Thanks to very rigid GQ-copper labels, EPR has become a prime method to study the structure of GQs, GQ-multimers and GQ-binding.[28,29,131]

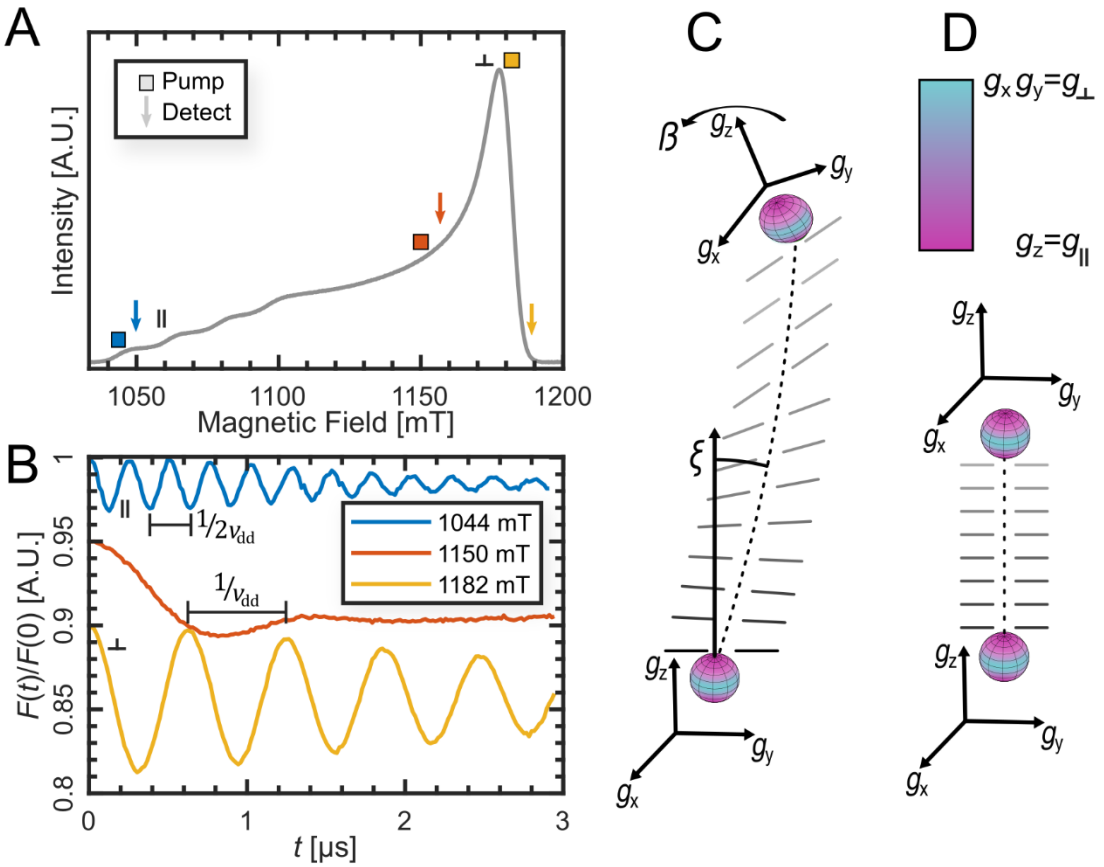

Figure 16: Overview of structural analysis of GQ dimers with EPR. **A**: ESE-detected fieldsweep of GQ with pump and detect positions for DEER marked. Furthermore, the parallel ∥ and perpendicular ⊥ position orientations are marked. **B**: Background corrected DEER traces. **C**: Overview of the potential angles between the copper labels. The spheres are coloured in based on the *g*-value in each respective direction. **D**: Schematic representation of the geometry of stacked GQ based on the angles found in previous DEER measurements.[29]

In these studies, copper-labeled GQs exhibited high rigidity and orientation selectivity, enabling the precise determination of distances and angles between GQ-dimers (Figure 16). As part of testing the capabilities of copper-labeled GQs as a ruler, two tetramolecular GQ-dimers ($[Cu^{2+}@(TTLGGG)_4]_2$, termed $[3G]_2$) and $[Cu^{2+}@(TLGGGG)_4]_2$, termed $[4G]_2$), differing by only one tetrad per GQ in length, were mixed. However, the DEER measurements were not only able to distinguish $[3G]_2$ and $[4G]_2$ but also showed a third distance consistent with [3G][4G]. Since DEER was able to distinguish the different species quite well and could identify and characterize various intercalators that bind at the GQ-GQ interface, many of which exhibit some level of drug activity, DEER can provide a valuable tool for studying the binding dynamics of GQs and their intercalators.[29,91,132,133] Therefore, the potential of extending DEER to study the dynamics of GQ is tested here.

3.1. Monomer shuffling and protocol development

There are different approaches to quantitative DEER spectroscopy. In the simplest case of only one species contributing to the DEER signal the relative amount can be extracted directly from the modulation depth. [134,135] However, for mixtures of different species, one needs to complete full orientation averaging and distance analysis and then extract the amounts from the

distance distribution.[136] But copper-labeled GQs display strong orientation selection combined with a broad spectrum. Therefore, multiple DEER measurements would be required for just one sample, making the process quite time-intensive. This issue is further exacerbated by the goal of studying dynamic systems, which requires a high volume of samples to measure for every time series. Instead, the orientation selection can be turned into an asset. By directly fitting the dipolar signals on a single well-defined orientation, one can also extract quantitative data in the same way one would from the distance distribution. But for this approach to work, orientation-selection must be strong enough that the respective frequency peaks can be well distinguished. To achieve high orientation selection, a field position with as little variation in g-value as possible is needed. This would be the case for either the low- or high-field end of the spectrum (Figure 17a-b). Since the g-tensor and interspin vector are nearly aligned (Figure 16d), the low field ($g_{\parallel}$) corresponds to $\theta = 0°$ while the high field ($g_{\perp}$) corresponds to $\theta = 90°$. In principle $\theta = 0°$ presents the most advantageous orientation, only requiring a shorter trace to be recorded, due to the higher dipolar frequency (Figure 16c). Since T_2-relaxation leads to signal degradation with increasing length of the trace, shorter traces result in a better signal-to-noise ratio. However, due to the g-tensor being axial, there are more spins with a g-value of $g_{\perp}$ than with $g_{\parallel}$. Furthermore, copper exhibits a strongly anisotropic hyperfine splitting, with virtually no splitting in the perpendicular direction, while having a coupling of over 500 MHz in the parallel region. The large splitting not only further reduces the signal intensity but also causes more mixing of g-values. This happens because each field position does not only correspond to one transition but up to four for each m_I (Figure 17a). The only field positions that are exempt from this are the perpendicular position where the hyperfine splitting disappears and the very outmost low-field edge of the signal (Figure 17b).

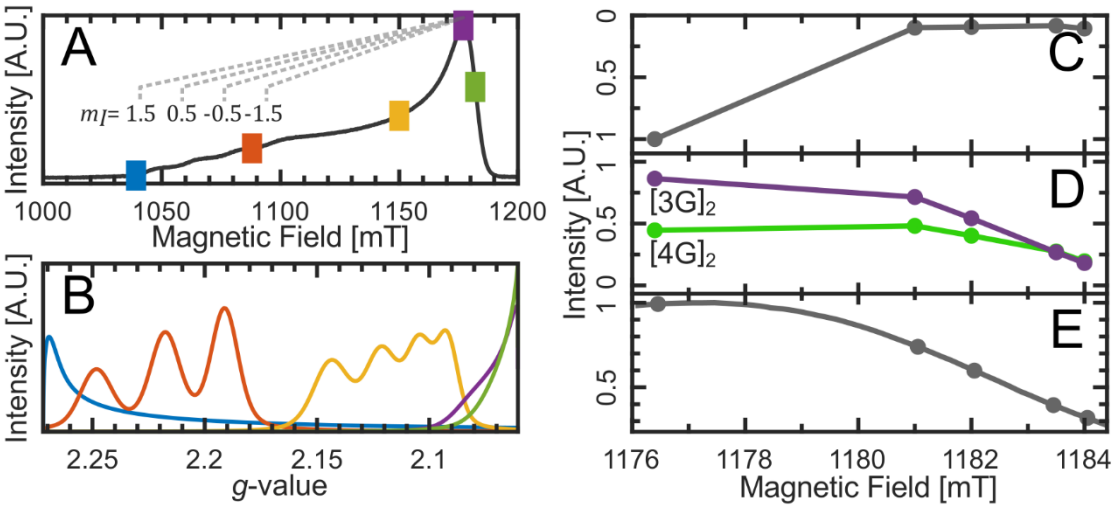

Figure 17: DEER optimization for quantitative measurements on GQs. A&B: Field-dependent *g*-value selection. **A**: ESE-detected field-sweep with the hyperfine splitting indicated by gray dashed lines. Furthermore, different field positions are marked by colored rectangles. The *g*-value distributions for these positions are shown in B. **B**: The distribution of *g*-values at the respective field positions (1040, 1088, 1150, 1177, 1182 mT) shown in A (same color). The *g*-values were calculated by doing orientation-selective simulations with pepper to calculate the intensity of each orientation at each field position. Then, the *g*-value for each orientation was calculated, and the orientation-dependent intensities were added up based on which *g*-value they correspond to. C-D: Field-dependent DEER optimization of a $[3G]_2$ and $[4G]_2$ mixture. **C**: The signal separation between the dipolar signal of $[3G]_2$ $[4G]_2$. The signals were fit as Gaussians, and the overlap area, normalized to the maximum overlap, was plotted on an inverted y-axis. **D**: The total signal intensity of the $[3G]_2$ and $[4G]_2$ dipolar signals. **E**: ESE-signal intensity at each field position, normalized to the maximum signal intensity.

Therefore, the perpendicular region of the spectrum was chosen for optimization. To find the best field position in the perpendicular range, multiple DEER traces were recorded on a sample where $[3G]_2$ and $[4G]_2$ had just been mixed. The signal separation, as well as the total signal strength, are plotted in Figure 17c-e. While the separation between the dipolar signals increases from 1177 mT to 1181 mT, it begins to plateau thereafter (Figure 17c). Meanwhile, the total signal intensity begins to drop off rapidly (Figure 17e). To ensure good separation while keeping a reasonable signal intensity, 1182 mT was chosen as the field position for quantitative DEER measurements. Interestingly, the ratio between the $[3G]_2$ and $[4G]_2$ dipolar signals changed with field. The relative intensities are dependent on two main factors. The first one is the total echo intensity of each species. Its influence is straightforward, as the measured DEER signal is simply the sum of DEER signals each species would have on its own. Therefore, a stronger echo results in a stronger contribution to the overall signal. This part implicitly includes the shape of the EPR spectrum.

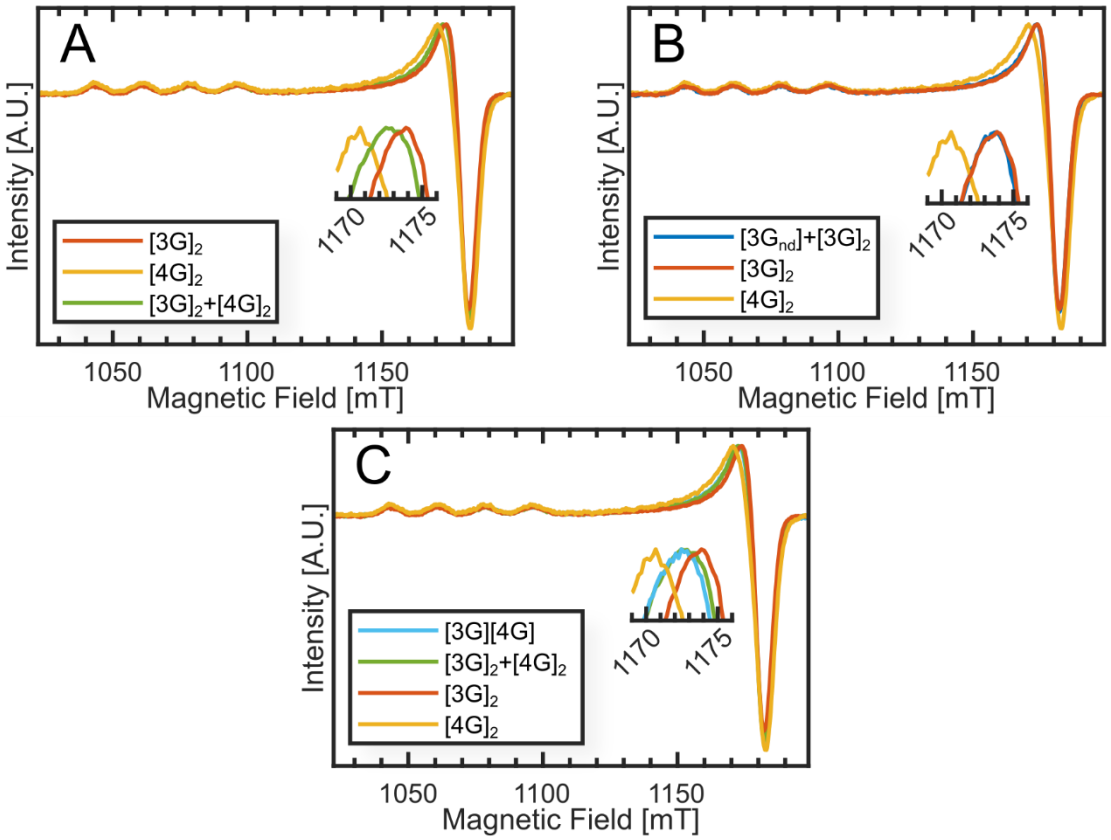

Figure 18: ESE detected field-sweeps of $[3G]_2$, $[4G]_2$, [3G][4G]-mixtures and mixtures with $[3G_{nd}]$. All spectra are pseudomodulated with a modulation amplitude of 3 mT. **A**: Comparison of pure $[3G]_2$, $[4G]_2$ and a mixture of $[3G]_2$ and $[4G]_2$ (sample taken immediately after mixing). **B**: Comparison of $[3G]_2$ with a 1:1 mixture of $[3G]_2$ and $[3G_{nd}]$. $[4G]_2$ is additionally shown as reference. **C**: Comparison of a 1:1 mixture of $[3G]_2$ and $[4G]_2$ after 1 min and after 40 hours, where significant amounts of [3G][4G] have formed. $[3G]_2$ and $[4G]_2$ are additionally shown as reference.

The second factor stems from the orientation selection-based part of $\lambda_{B,eff}$. To determine the source of this behavior, samples containing $[3G]_2$, $[4G]_2$, and $[3G_{nd}]$, a non-dimerizing version of [3G], as well as mixtures of them, were compared (Figure 18). $[3G_{nd}]$ and $[3G]_2$ display virtually identical EPR spectra (Figure 18b), indicating that the dimerization process of the GQs has little effect on the confirmation and environment of the spin label itself. However, $[3G]_2$ and $[4G]_2$ display distinctly different EPR spectra with a noticeable change in the perpendicular region (Figure 18a). Furthermore, the spectra of $[3G]_2$+$[4G]_2$ seems to be a combination of both. To ensure that this change is simply the result of the $[3G]_2$ and $[4G]_2$ spectra overlaying and not oligonucleotides exchanging mixtures of $[3G]_2$ and $[4G]_2$ with $[3G_{nd}]$ were incubated for 40 hours (Figure 19). No change in modulation depth was observed. If mixed GQs containing oligonucleotides from $[3G_{nd}]$ formed, one would expect the uptake of oligonucleotides with an overhang on the binding side to hinder dimeraization. Finally, the formation of [3G][4G] does not lead to a change in spectral lineshape compared to $[3G]_2$+$[4G]_2$ either (Figure 18c). Thus, the parameters controlling the spectral lineshape (g, A, linewidth) are independent of the tertiary structure of the GQ and only depend on the structure right at the copper label, which in this case probably depends on the extra thymine at the 5′ end for [3G] and $[3G_{nd}]$.

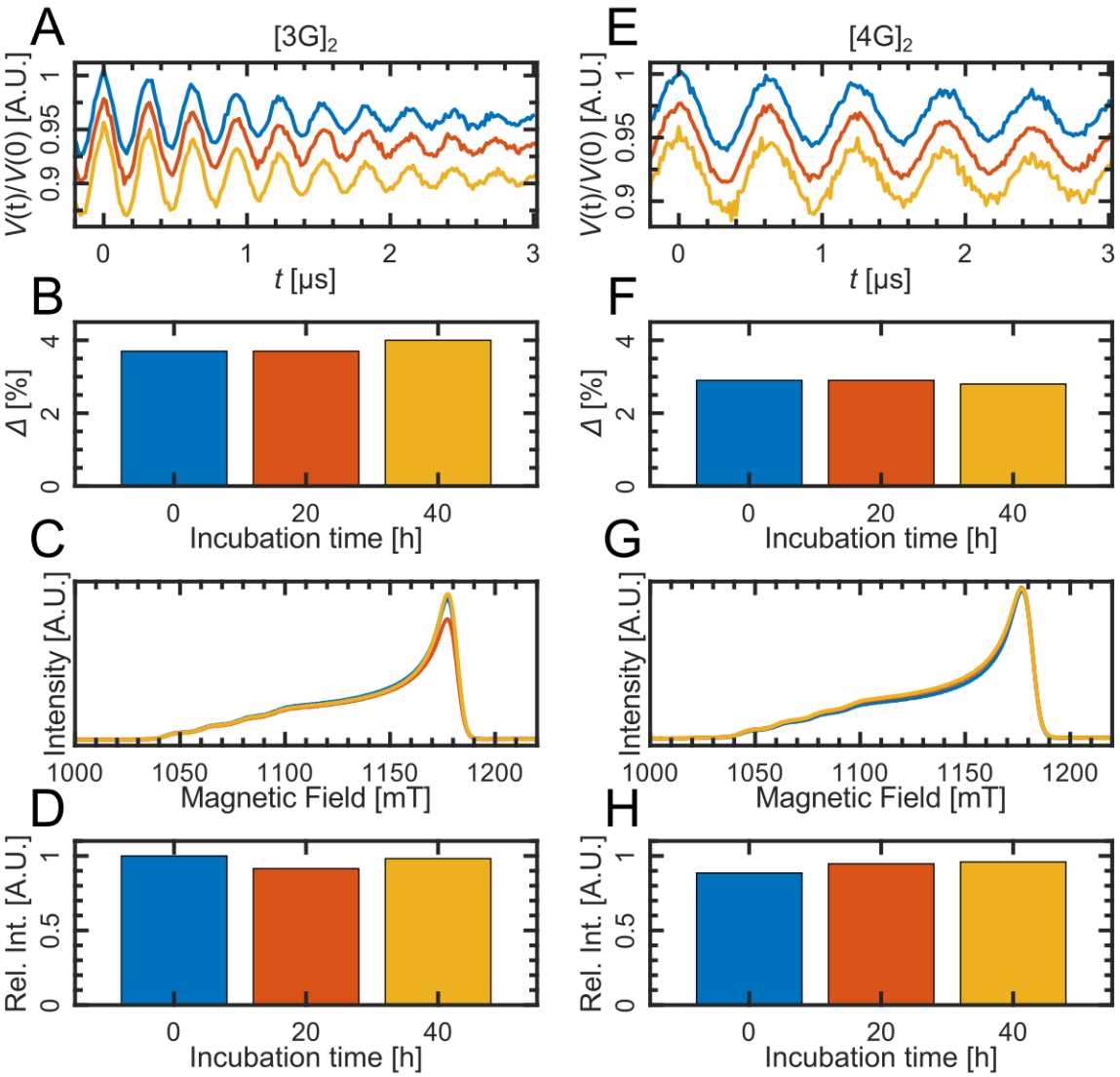

Figure 19: Stability measurements on $[3G]_2$ and $[4G]_2$ mixed with $[3G_{nd}]$. Samples were incubated at 12 °C for 1 min (blue), 20 h (orange) and 40 h (yellow). **A**&**E**: DEER traces of the $[3G]_2$ and $[4G]_2$ mixtures, respectively. **B**&**F**: The associated modulation depths. **C**&**G**: ESE-detected field sweeps of the respective samples, normalized to spectrometer parameters only. **D**&**H**: Integral of the total signal intensity of the field sweep. The intensities were normalized to the largest intensity between all samples.

To ensure that the GQs themselves are stable, the signal intensity was monitored over time (Figure 18c, d, g, h). While ESE-detected fieldsweeps in the overcoupled QT-II resonator aren't fully quantitative, they can still give a rough estimate for the total amount of formed GQs with Cu^{2+} in them (Figure 19c,d,g,h). This can be achieved because free copper relaxes much faster than bound copper, resulting in a significantly lower signal intensity.[29] Therefore, if GQs were to dissociate over time, one would expect a drop in signal intensity as bound copper is released. This is not the case, indicating that the model GQ is stable at 12 °C.

Given that the DEER measurements were taken at the very high field end of the spectrum, one would expect that the *g*-value is approximately the same for all field positions. Therefore, the changes in dipolar signal would be purely the result of different amounts of B-spins at the respective field positions, not changes in orientation selection. If this hypothesis is true, one would expect the modulation amplitude to scale with the signal intensity at the pump position

(Figure 20a). Furthermore, the same should also apply to the dipolar signals if correlated with the echo intensities of their own species (Figure 20b).

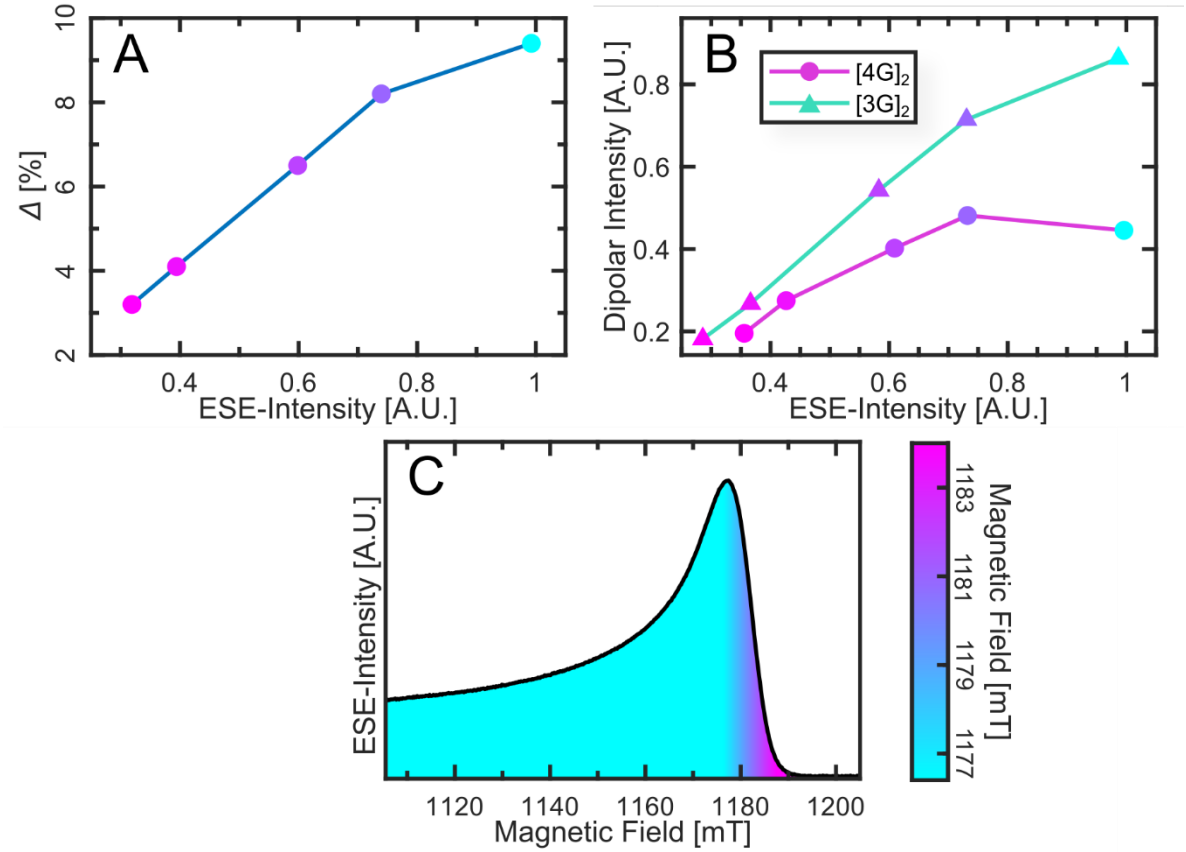

Figure 20: **A**: Modulation amplitude of $[3G]_2$+$[4G]_2$ sample plotted against the ESE-intensity. The markers are colored in based on the field position of the DEER experiment. **B**: Intensity of the $[3G]_2$ and $[4G]_2$ dipolar signal plotted against the ESE-intensity of a pure $[3G]_2$ and $[4G]_2$, respectively. The markers are colored in based on the field position of the DEER experiment. **C**: ESE-detected fieldsweep colored in the same fashion as A and B.

Both expectations are fulfilled for up to 1181 mT, although the $[4G]_2$ dipolar signal is a slightly worse fit. However, for 1177 mT, things clearly start to deviate. This fits with the prior observation that the overlap between both dipolar signals only changes up to 1181 mT, since a change in overlap requires a change in shape of the dipolar signal, which in turn requires a change in sampled orientations.

Finally, combining the idea that dimerization has a negligible impact on the spectral line-shape and that orientation selection does not change above 1181 mT, one could predict that for a mixture of $[3G]_2$, $[4G]_2$ and [3G][4G], the fraction of [3G][4G] dipolar signal does not change. In the case of [3G][4G], either [3G] or [4G] can serve as the B-spin. As a result, [3G][4G] experiences both the increase in signal $[3G]_2$ experiences and the decrease $[4G]_2$ experiences.

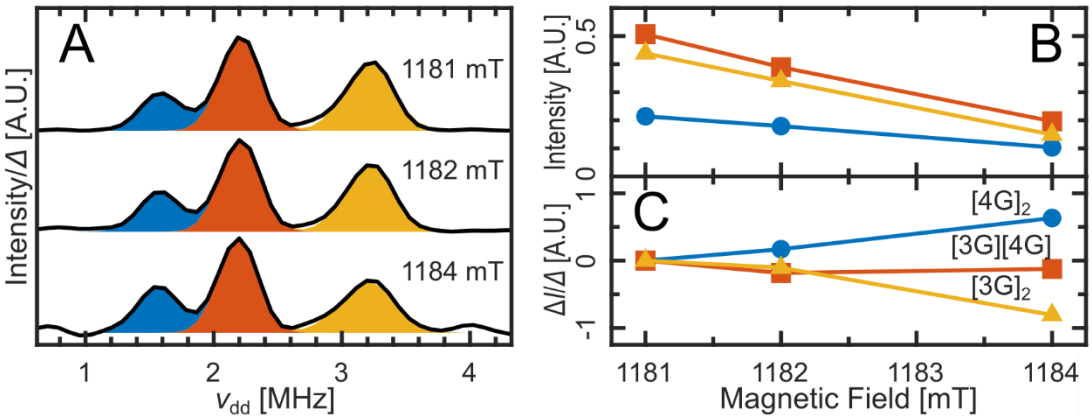

Figure 21: Field-dependent DEER measurements on a mixture of $[3G]_2$ (yellow), $[4G]_2$ (blue) and [3G][4G] (orange). **A**: Dipolar spectra for each field with each species fit with Gaussians. **B**: The relative intensities of each species. The sum of the total intensities for each field position was normalized. To better show the relative change for each species, the intensities for each species were additionally normalized to their mean value.

Indeed, while the total dipolar signal intensity decreases, the fraction of [3G][4G] remains consistent, independent of the field position, as predicted (Figure 21). Therefore, orientation selection on modulation depth can be effectively eliminated in copper-labeled GQ by moving to the high end of the spectrum.

3.1.1. DEER vs RIDME

One downside to performing very orientation-selective DEER is the low modulation depth resulting from orientation selection on the B-spin. In principle RIDME could provide a good alternative to DEER since its B-spin inversion only depends on the mixing time (T_{mix}) and T_1-distribution. However, since copper acts as both A- and B-spin it is not possible to set T_{mix} significantly larger than T_1 as the A-spin would also relax back during the mixing block. Using a shorter mixing time has two main consequences. First, the full possible inversion efficiency of 50% for copper cannot be reached. Given that the DEER measurements only reach modulation depths of around 7% RIDME is still likely to present an improvement in modulation depth. However, the second consequence is that now, the inversion efficiency is dependent on the T_1-distribution potentially reintroducing orientation selection for inversion efficiency. DEER and RIDME were compared at two field positions (1176.4 mT and 1184 mT) corresponding to the signal maximum and highest practical field position, aka the field position where the highest orientation selection is expected (Figure 22). RIDME did indeed provide a higher modulation depth (1.8 times for 1176.4 mT and 4.75 times for 1184 mT). However, while DEER showed fully separated dipolar signals for $[3G]_2$ and $[4G]_2$ at 1184 mT, RIDME did not, with the 1184 mT RIDME signal giving similar separation to the 1176.4 mT DEER signal (Figure 22d).

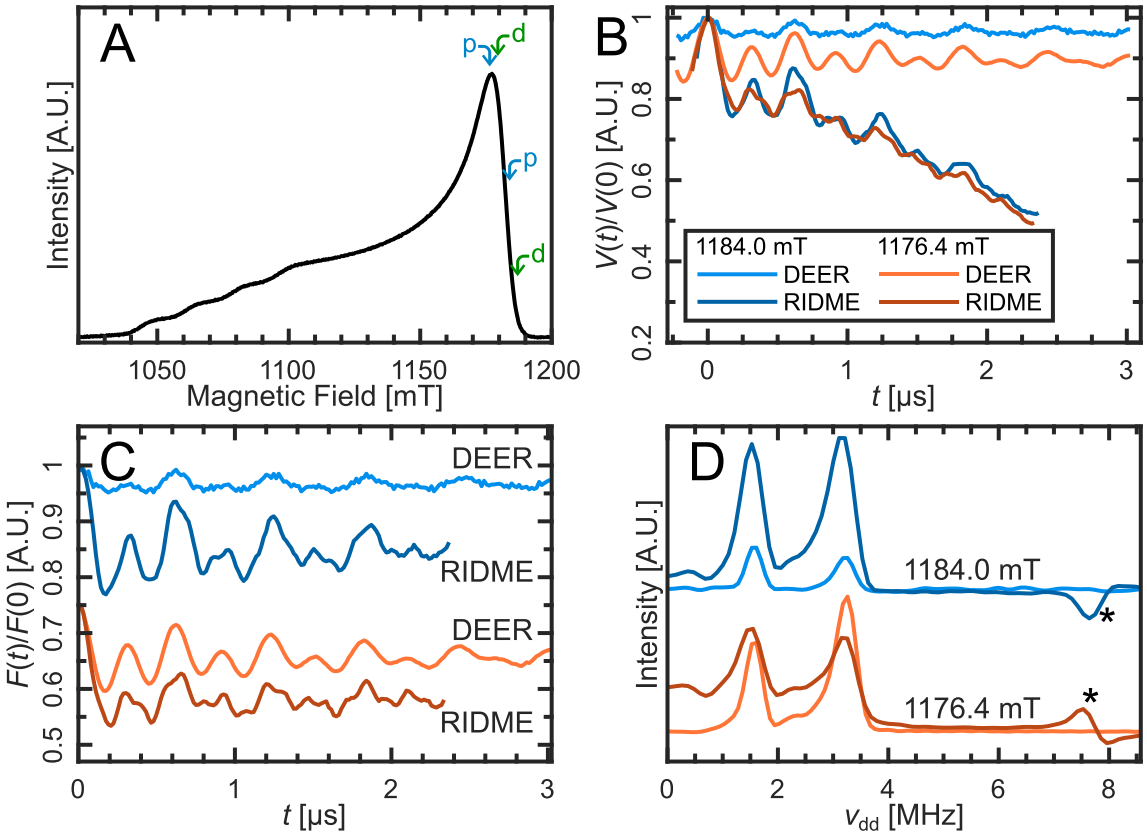

Figure 22: Comparison of DEER and RIDME measurements. Measurements are taken on a mixture of $[3G]_2$ and $[4G]_2$ frozen directly after mixing. Measurements are taken at Q-band at 19 K for DEER and 30 K for RIDME. The mixing time for the RIDME measurements was set to 15 µs. Pump detect separation for DEER was 90 MHz. **A**: ESE detected fieldsweep with the pump and detect positions used for DEER marked. RIDME measurements were taken at the respective pump positions. **B**: Raw measurements. **B**: Background corrected measurements. Background correction was done with DEERanalysis, a third-order polynomial correction was used for the RIDME traces, while a third-order homogenous background was used for the DEER spectra. **D**: One-sided dipolar spectra. Both RIDME traces display ^{2}H ESEEM artefacts at around 7.7 MHz indicated by an asterisk.

Since the proposed method requires a good separation of the dipolar signals, RIDME was deemed unsuitable. Nonetheless, RIDME still shows clear orientation selection, demonstrating the rigidity of the system, and could provide a good alternative for GQs where higher modulation depth is the primary concern. It could also prove helpful for the study of GQs where the copper labels are misaligned, for example, bent GQs, which could result in a significant separation of desirable pump and detection positions. It should also be noted that in theory, the modulation depth of a RIDME measurement can be calculated from T_1 and T_{mix}. Therefore, the amount of dimer can in theory be calculated without requiering any standard. However, in practice flip flip-flops reduce the achieved modulation amplitude. [137] Additionally, anisotrope T_1 can influence the modulation amplitude quite a lot as shown by the attempt to calculate the amount of dimers this way (Chapter 5.5.1)

Aside from RIDME, chirped pump pulses can also help with low inversion efficiency. Unlike a classical monochromatic pulse, a chirped pulse's frequency is swept during the pulse. This allows chirped pulses to have a much larger bandwidth than conventional pulses. To test the effectiveness of chirped pulses, three different field positions were compared for a sample of $[4G]_2$ mixture (Figure 23). Similar to RIDME, the application of chirped pump pulses

significantly increases the modulation depth. However, unlike RIDME, the width of the dipolar signal barely changes (Figure 23c). This can be explained by the considerable width of the copper spectrum. Although only a fraction of B-spins is inverted by the monochromatic pulse, and many more through the chirp pulse, compared to the entire width of the spectrum, the difference is virtually negligible, and the additional spins flipped by the chirp pulse are still in the same orientation as the ones pumped by just the monochromatic pulse.

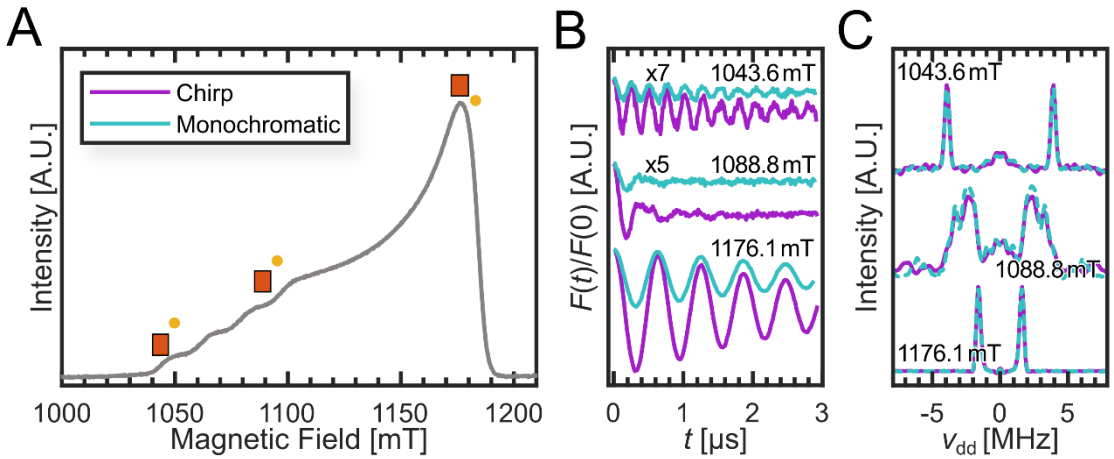

Figure 23: Field-dependent chirped pump pulse DEER measurements on $[4G]_2$ with chirped (pink) and and monochromatic (blue) pulses. **A**: ESE-detected fieldsweep of $[4G]_2$ with the detect (yellow) and pump (orange) positions marked. The width of the pump window is estimated using the easyspin function exciteprofile. **B**: The DEER traces for each field position. The traces for 1088.8 mT and 1043.6 mT were scaled up by a factor of 5 and 7 for visibility reasons. **C**:Dipolar spectra.

3.1.2. Monomer shuffling

With the basic quantitative DEER characteristics of the tetramolecular quadruplexes quantified, the method needed to be tested on an actual dynamic system. For this purpose, the

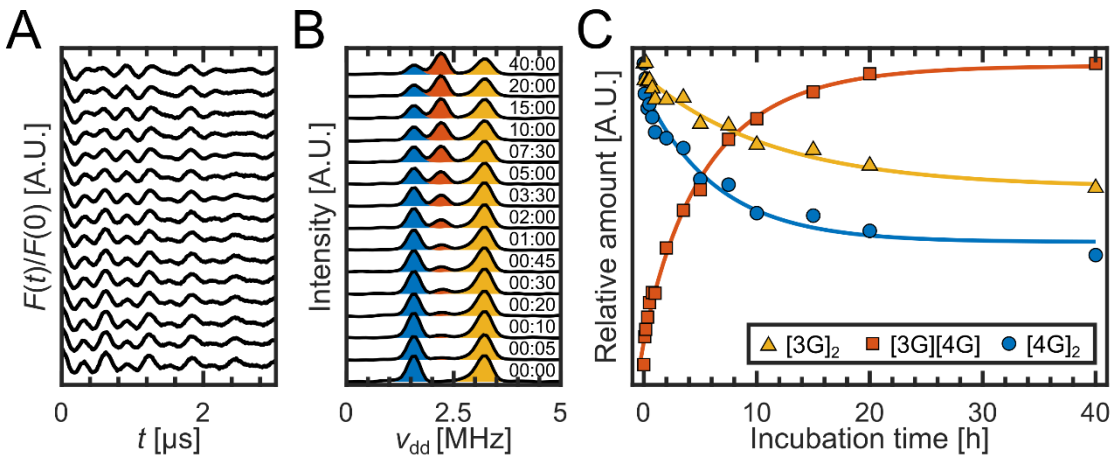

Figure 24: $[3G]_2$ and $[4G]_2$ were mixed at 12 °C, forming [3G][4G]. DEER measurements were taken at 1182 mT. The trace at 0 min was constructed from the sum of $[3G]_2$ and $[4G]_2$, each mixed with $[3G_{nd}]$. **A**: Background corrected DEER traces of DEER measurements over time. **B**: Dipolar spectra with the fitted areas filled (yellow $[3G]_2$, orange [3G][4G], blue $[4G]_2$). **C**: The intensities fitted against the incubation time. Since the relation between signal strength and concentration is currently unknown, the signals for each species were normalized to the largest signal of that species. Stretched exponentials were fitted to the data to function as a guide to the eye.

interaction of quadruplexes in a mixture of [3G]2 and [4G]2 was followed for 40 hours with DEER (Figure 24). As expected, $[3G]_2$ and $[4G]_2$ began to exchange monomers slowly, forming

[3G][4G], approaching equilibrium between $[3G]_2$, $[4G]_2$, and [3G][4G] after 40 hours (Figure 24c). The relative concentrations of $[3G]_2$ and $[4G]_2$ change at different rates, with $[4G]_2$ decreasing more rapidly than $[3G]_2$. This implies that the dimerization of [3G] has a higher equilibrium constant than that of [4G], which is consistent with NMR studies on the topic.[138] While there is some variation in the calculated amounts (Figure 24c) the amounts overall follow a smooth curve as expected.

Overall, the data could be easily and quickly fitted, demonstrating that quantitative data can be extracted directly from the frequency domain of copper-labeled GQs.

3.2. Intercalation and temperature dependence

A myriad of different intercalators are known for GQs. Among them are many drugs that specifically target GQs.[80,81,91,133] Therefore, being able to follow the binding of intercalators to GQs would provide a powerful tool for drug development. The same studies that showed that DEER is able to distinguish between [3G]2, [4G]2, and [3G][4G] also showed that$[3G]_2$ and $[4G]_2$ can serve as a test system for intercalators integrating into the interface between the GQs and detecting the resulting change in GQ-dimer structure. However, so far, this has only been demonstrated for intercalators already present during the assembly of the tetramolecular GQs.[29]

3.2.1. PIPER intercalation

PIPER was one of the intercalators that had previously been shown to intercalate into GQs when added during GQ formation (Figure 25).

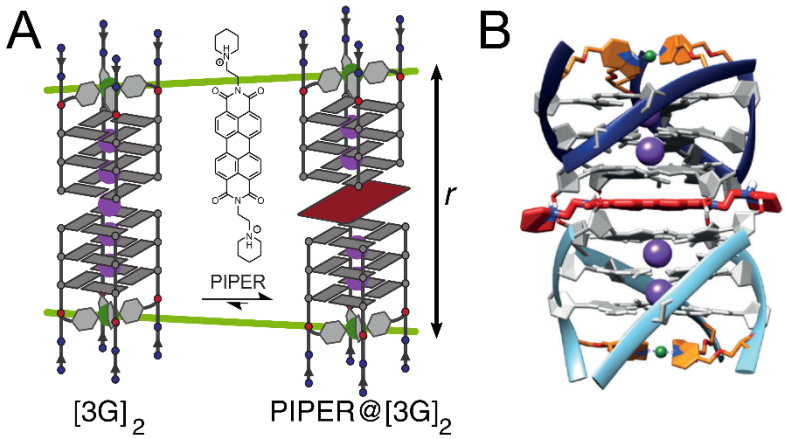

Figure 25: **A**: Schematic intercalation of PIPER into $[3G]_2$ with the change in distance that is measured with DEER indicated by green lines. **B**: MD-derived structural models of the PIPER@$[3G]_2$ sandwich complex (adapted from Stratmann, Kutin, et all. Angewandte Chemie 60, 4939–4947 (2021) under creative commons license (CC4))[29]

Starting with a signal of just $[3G]_2$, a signal of PIPER@[3G]2 grows over time (Figure 26). Following the same rule, already established for $[3G]_2$, $[4G]_2$ and [3G][4G], of "what happens at the GQ-GQ interface has no observable effect on the copper labels", the intercalation of PIPER also seems not to affect the lineshape (Figure 49a). Combined with the relatively small change in the intramolecular angles ξ and β ($0° \pm 1° \rightarrow 4° \pm 8°$ and $0° \pm 1° \rightarrow 1° \pm 12°$), [29] $[3G]_2$

and PIPER@$[3G]_2$ can be assumed to have the same relationship between dipolar signal intensity and concentration.

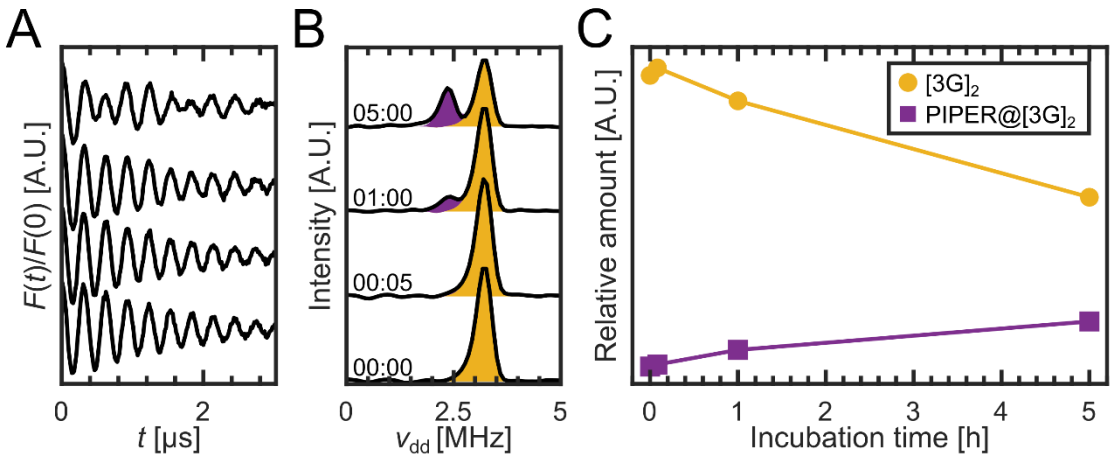

Figure 26: $[3G]_2$ and PIPER were mixed at 12 °C (1:1). DEER measurements were taken at 1182 mT. **A**: Background corrected DEER traces of DEER measurements over time (same times as traces in B at the same height). **B**: Dipolar spectra with the fitted areas filled (yellow $[3G]_2$, violet PIPER@$[3G]_2$). **C**: The relative amounts plotted against the incubation time.

While more data points are needed to get the whole picture, one can already observe that the total dipolar signal intensity decreases over time. This indicates that while PIPER prefers to bind to GQs, a PIPER@$[3G]_2$ complex is less stable than a $[3G]_2$ complex, and at least part of them dissociate into PIPER@[3G]. Furthermore, the amount of $[3G]_2$ has dropped by almost half after 5 hours. This behavior is similar to that of mixing $[3G]_2$ and $[4G]_2$, where the amount of $[3G]_2$ after 5 hours is also close to the halfway point between the initial and final amounts (Figure 24). While this, on its own, is hardly proof, it could be a first indicator that the underlying mechanism behind monomer shuffling and intercalator binding is the same.

3.2.2. Temperature dependence

Another point of interest for these kinds of measurements is temperature. To record DEER spectra, the sample must be cooled to cryogenic temperatures. Therefore, the question arises as to what state the frozen sample represents. Is it frozen rapidly enough that the sample represents the system at the temperature it had before it was frozen? Or does it represent the system at a temperature just before freezing, regardless of the original temperature of the sample? To answer this question, two batches, $[4G]_2$ and PIPER@$[4G]_2$, where PIPER was added during GQ-assembly, were measured at different temperatures. $[4G]_2$ was chosen over $[3G]_2$ due to its lower stability, ensuring that any temperature dependence is detected, if possible.

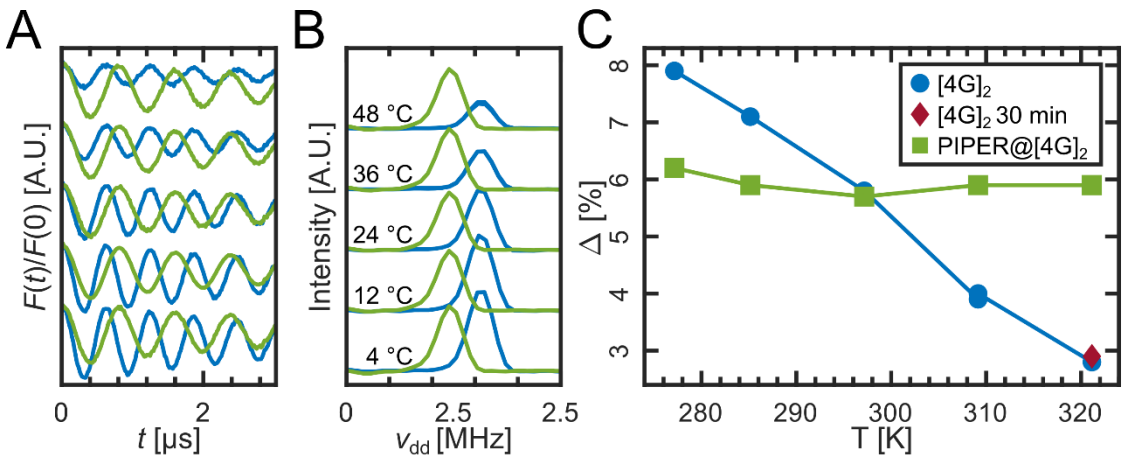

Figure 27: $[4G]_2$ (blue) and PIPER@$[4G]_2$ (green) were brought to different temperatures for 15 min, then rapidly mixed with glycerol and flash frozen. DEER measurements were taken at 1182 mT. **A**: Background corrected DEER traces of samples at different temperatures. **B**: The corresponding dipolar spectra. **C**: The modulation depths plotted against temperature. Additionally, a $[4G]_2$ sample incubated at 48 °C for 30 min is shown in dark brown.

Each sample was incubated at the respective temperature for 15 min; additionally, a sample of $[4G]_2$ was incubated for 30 min at 48 °C. Since both the 15- and 30 min incubation time samples yielded virtually the same modulation depth, 15 min can be considered sufficient incubation time for equilibrium to reestablish (Figure 27c). Again, the same simplifications with regard to angle and lineshape can be made (Figure 49b).

The modulation depth of $[4G]_2$ noticeably decreases with increasing temperature, clearly indicating that the frozen sample does represent the system before freezing, not during. In contrast to $[4G]_2$, PIPER@$[4G]_2$ displays virtually no temperature dependence. Furthermore, at temperatures below 24 °C the modulation depth of $[4G]_2$ is higher than the modulation depth of PIPER@$[4G]_2$. It seems that rather than PIPER simply binding to GQs and stabilizing or destabilizing them, another more complex mechanism is at play.

3.2.3. Double intercalation

In addition to removing the temperature dependence in GQ stability, another previously unknown property of PIPER intercalation was discovered. When adding PIPER to fully formed $[4G]_2$ at 4 °C, two PIPER intercalated into $[4G]_2$, exclusively forming 2PIPER@$[4G]_2$ (Figure 28).

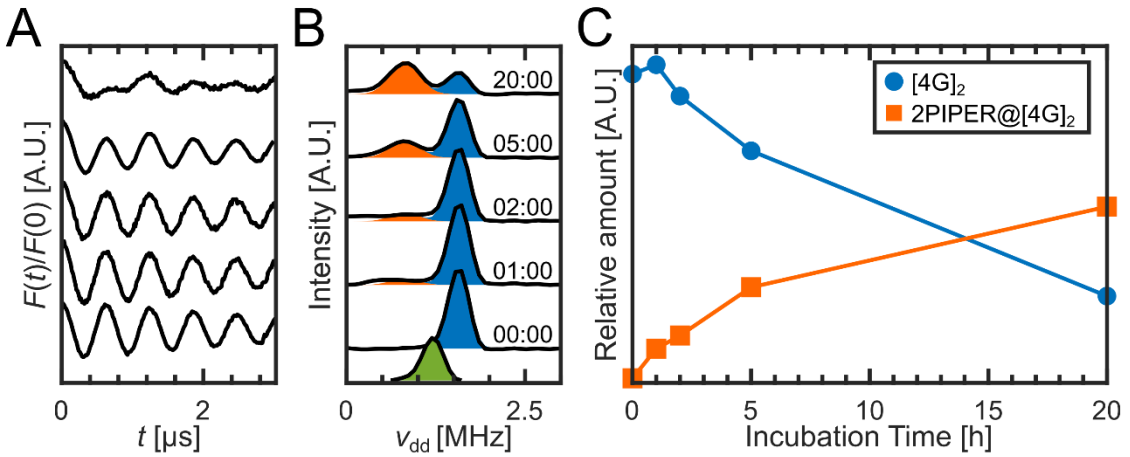

Figure 28: $[4G]_2$ and PIPER were mixed at 4 °C (1:1). DEER measurements were taken at 1182 mT. **A**: Background corrected DEER traces of DEER measurements over time (same times as traces in B at the same height). **B**: Dipolar spectra with the fitted areas filled (blue $[4G]_2$, orange 2PIPER@$[4G]_2$). Additionally, PIPER@$[4G]_2$ is shown in green for comparison. **C**: The relative amounts plotted against the incubation time.

This is unexpected, as adding 1 equivalent of PIPER during annealing at 4 °C exclusively produced single intercalation, and even 3.5 equivalents of PIPER still only resulted in a mixture of single and double intercalation. Furthermore, adding PIPER to fully formed $[3G]_2$ at 12 °C also exclusively produces single intercalation, mirroring the addition of PIPER during annealing (Table 4).

Table 4: Intercalation modes found for different environments. PIPER equivalents are given relative to the amount of GQ-dimers.

5′-TTL GGG-3′ + PIPER (1eq)	$\xrightarrow{\text{annealing}}$	PIPER@$[3G]_2$			Single intercalation[29]
5′-TTL GGG-3′ + PIPER (2eq)	$\xrightarrow{\text{annealing}}$	PIPER@$[3G]_2$ (50%) +2PIPER@$[3G]_2$ (50%)			Single intercalation & double intercalation[29]
$[3G]_2$ + PIPER (1eq)	$\xrightarrow{12\ °C}$	PIPER@$[3G]_2$			Single intercalation
5′-TLG GGG-3′ + PIPER (1eq)	$\xrightarrow{\text{annealing}}$	PIPER@$[4G]_2$	$\xrightarrow{4,12,24,\ 36,48\ °C}$	PIPER@$[4G]_2$	Single intercalation
$[4G]_2$ + PIPER (1eq)	$\xrightarrow{4\ °C}$	2PIPER@$[4G]_2$			Double intercalation

There are multiple possible mechanisms that might explain this behavior. First, the reduced temperature might cause PIPER to form dimers and simply replace the uptake of a single PIPER with that of two PIPER. PIPER is prone to aggregating, and similar compounds are known to form dimers.[82] Furthermore, while the annealing process mostly occurs at 4 °C, it starts at 85 °C and is then cooled to 4 °C over almost 3 hours. Therefore, PIPER@$[4G]_2$ might already form at higher temperatures, with all PIPER being used up by the time low temperatures are reached.

Alternatively, the double intercalation might be the result of PIPER intercalation being a multistep reaction. This scheme presupposes that PIPER doesn't move into formed dimers but instead binds to monomers, which then recombine into dimers. It is known from our temperature-dependent measurements that there are fewer single GQ at 4 °C compared to 12 °C. Therefore, the single quadruplex/ PIPER-quadruplex equilibrium would be far on the side of PIPER-quadruplex leading to the recombination of mostly 2PIPER@[G].

3.3. Conclusion

DEER spectroscopy is well-suited to study the dynamics of GQs. It can resolve the differences in dipolar frequency enough to distinguish different GQ and GQ intercalator complexes. Furthermore, it appears that GQ dynamics occur on a timescale of hours, making them sufficiently slow that multiple samples can be taken during the incubation period. While the potential of orientation selection effects on modulation depth presents a caveat, the evidence so far suggests that this can be mitigated by staying in the high-field region and accounting for echo intensities. Arguably, the method's main drawback at present is the lack of a standard to compare measurements against, which prevents the association of actual concentration units with measured results. However, the use of standards for DEER is well discussed in literature, making the creation of a suitable standard only a question of time.[37] However, even without a standard, the method was able to uncover a new, switch-like behavior in the formation of PIPER sandwich complexes, leading to unexpected double intercalation. Furthermore, this demonstrates the method's resilience, as the formation of double-stacked dimers was not predicted at all, yet could be readily identified nonetheless. Looking into the future, there are whole classes of different GQs besides the small model ones used here, most of which this label can be applied to.[28] One might also imagine copper-labeled GQs as sensors, with the effect the species of interest has on the GQ-dimers being used as a readout.

3.4. Materials and methods

3.4.1. Sample preparation

GQs were assembled by the Clever lab with the following protocol. Stock solutions were prepared by dissolving the respective oligonucleotide and $CuSO_4$ in 50 mM potassium phosphate buffer (pD 7.0) in D_2O.

The stock solutions were heated to 85 °C for 10 min, then slowly cooled to 4 °C with a cooling rate of 0.5 °C/min, and then left at this temperature overnight. Subsequently, the samples were frozen at -20 °C for 1 h and thawed again to 4 °C. The stock solutions were mixed and incubated at 12 °C. Whenever a sample was taken, the sample was rapidly mixed with glycerol-d_8 (1:1 v/v), transferred into an EPR-tube, and frozen in liquid nitrogen. The final concentration was 62.5 μM GQ.

Table 5: Overview of the used GQs.

	Tetrads	Dimerizes	DNA-sequence
[3G]	3	Yes	5'-TTL GGG-3'
[3G$_{nd}$]	3	No	5'-TTL GGG T-3'
[4G]	4	Yes	5'-TLG GGG-3'

3.4.2. Measurement parameters

All measurements were performed in a QT-II resonator from Bruker in overcoupled mode. Since GQs proved to be very sensitive to the positioning of the DEER measurement on the spectrum, the following modification was made to the standard over-coupling procedure. After the resonator was overcoupled and the spectrometer turned into pulse mode instead of changing the spectrometer frequency to match the resonator frequency, the frequency was set to 34.003 GHz and the cavity length was adjusted to match the spectrometer frequency. Pulse lengths for pump and detect were determined using p(t) - τ_1 - $\frac{\pi}{2}$ - τ_2 - π - τ_2 - echo. The detect position was shifted down by 90 MHz. Typical pulse lengths for π_{d} were 70 – 72 ns and 30 – 32 ns for π_{p}. The pump pulse was incremented in 14 ns steps with a starting value of t=-200 ns and $\tau_1$and τ_2 were set to 300 and 3200 ns each. The shot repetition time was set to 510 µs.

Table 6: Measurement parameters for pulsed ESE-detected field sweeps

Pulse sequence	$\pi/2$	- τ	- π	- τ	- Detect
Length [ns]	10	300	20	300	80
Channel	+<x>		+<x>		
Attenuation	3 dB				
Sweep rate	33.31 G/s				
Shot repetition time	1200 µs				
Temperature	19 K				
Frequency	34.003 GHz				

Table 7: Measurement parameters for microwave nutation for detect sequence

Pulse sequence	d	- τ_{w}	- $\pi/2$	- τ_1	- π	- τ_1	- Detect
Length [ns]	2+t	5000	25	340	50	340	180
Shape[a]	(1)		(1)		(1)		
Amplitude	90%		90%		90%		
Attenuation	0 dB						
t	0 ns to 600 ns in 2 ns steps						
Shot repetition time	1000 µs						
Temperature	19 K						
Frequency	33.913 ± 0.000 GHz						
Field	1182 mT						

[a] Numbering system following Bruker standard, (1): Gaussian pulse, (6): Gaussian pulse with adjusted sweep frequency [139].

Table 8: Measurement parameters for microwave nutation for pump pulse

Pulse sequence	d	- τ_w	- $\pi/2$	- τ_1	- π	- τ_1	- Detect
Length [ns]	2+t	5000	10	320	20	320	250
Shape[a]	(1)		(1)		(1)		
Amplitude	90%		90%		90%		
Attenuation	0 dB						
t	0 ns to 600 ns in 2 ns steps						
Shot repetition time	1000 µs						
Temperature	19 K						
Frequency	34.003 ± 0.000 GHz						
Field	1182 mT						

Table 9: Measurement parameters for GQ-GQ DEER with 16-step phasecycling $(\pi/2 - \tau_1 - \pi - (\tau_1 + t) - p - (\tau_2 - t) - \pi - \tau_2 - \text{Detect})$

Pulse sequence	$\pi/2$	π	p	τ_1	τ_2	t	Detect
Length [ns]	36.5 ± 1.3	73.0 ± 2.5	32.6 ± 2.3	300	3200	-200:14:3062	46 ± 5
Shape[h]	(1)	(1)	(1)				
Amplitude	90%	90%	90%				
Frequency offset [MHz]			+90				
Shot repetition time	510 µs						
Temperature	19 K						
Frequency	33.913 ± 0.000 GHz						
Field	1182 mT						

Table 10: Measurement parameters for GQ-GQ RIDME with 8-step phasecycling $(\pi/2 - \tau_1 - \pi - (\tau_1 + t) - \pi/2 - T_{mix} - \pi/2 - (\tau_2 - t) - \pi - \tau_2 - \text{Detect})$

Pulse sequence	$\pi/2$	π	T_{mix}	τ_1	τ_2	t	Detect
Length [ns]	33	66	15 µs	300	2600	-50:14:2414	46 ± 5
Shape[h]	(1)	(1)					
Amplitude	90%	90%					
Frequency offset [MHz]							
Shot repetition time	204 µs						
Temperature	30 K						
Frequency	34.003 GHz						
Field	1184 mT						

[a] Numbering system following Bruker standard, (1): Gaussian pulse, (6): Gaussian pulse with adjusted sweep frequency [139].

3.4.3. Data analysis

Background correction was performed in DeerAnalysis using a homogeneous background. For RIDME, a second-order polynomial was used.

To extract the amount of dipolar signal, a self-written global fitting algorithm that fits all time steps at the same time was used. The algorithm allows for either fitting the shapes of peaks as Gaussian shapes or directly supplying the shape of a species signal if a measurement of just that species is available. (Here Gaussian fits were used for PIPER@[3G], and 2PIPER@[4G]) To generate starting values for fitting, the algorithm fits each spectrum separately with Gaussians only. The resulting peaks are then binned and the most likely values for each peak's frequency selected. From this, the limits for fitting the frequency are constructed as the range from the next lower frequency peak (or 0) to the next higher frequency peak (or the selected maximum). Next, starting values from the prefit that lie outside of this range are replaced by those generated from the binning process. Finally, if additional shapes were given, these shapes are assigned to the peaks based on the values from the binning process, and the scaling factors from the prefit are converted into scaling factors for the shapes, which replace the Gaussians in the main fit. For the main fit each spectrum still uses it's own set of widths and frequencies for the peaks. However, here the RMSD is additionally multiplied with a function that punishes divergent values for the parameters of each peak. Specifically, it takes a weighted average of the parameters for each peak with the intensity as the weight factor. It then takes the RMSD of the parameters from the mean value.

All related algorithms will be published on https://github.com/victorselve-del/eprTools.

4.
RNR

The β_2-subunit of *E. Coli* RNR contains multiple potentially EPR-active sides (Figure 29a). First are the respective Y_{122} in each β-subunit, which will form a Tyrosyl radical in the active form of β_2 (Figure 29b).

Furthermore, the metal-binding sides in each subunit can harbor up to two metals, which can be either manganese or iron. All EPR-active components have different, distinct distances to each other (Figure 29c). DEER spectroscopy was employed to monitor the loading of Mn in both subunits, the generation of Tyr-radicals and the generation of Tyr-radicals in β_2 with a mixed FeMn cofactor. This chapter provides compelling evidence that only a limited number of β_2 can bind any manganese in the first place. Furthermore, this fraction can bind manganese in both β-subunits. Finally, it shows that the formation of the tyrosyl radical can still occur even if the opposite β_2 subunit contains manganese.

A

		EPR-active when:	Spin:
Y_{122}•	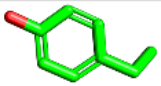	Requires 3 Fe^{2+} + O_2 for generation. Is only generated in both subunits at the same time.	**1/2**
Mn^{II}		Always EPR active	**5/2**
$Mn^{III}Fe^{III}$		Always EPR active, has combined spin ½	**1/2**
$Mn^{II}Mn^{II}$		Ground state is EPR silent, excited spin 1 and 2 states are possible	**0**,1,2
Fe^{III}-(O^{2-})-Fe^{III}	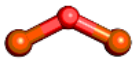	EPR silent. Formed in active β_2-subunit.	**0**

B

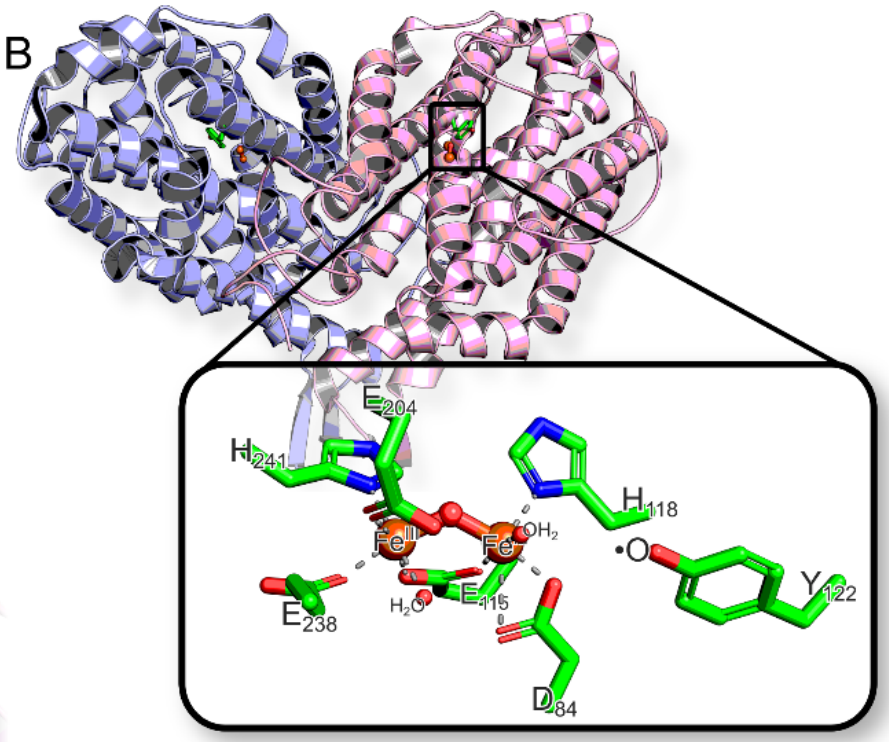

C

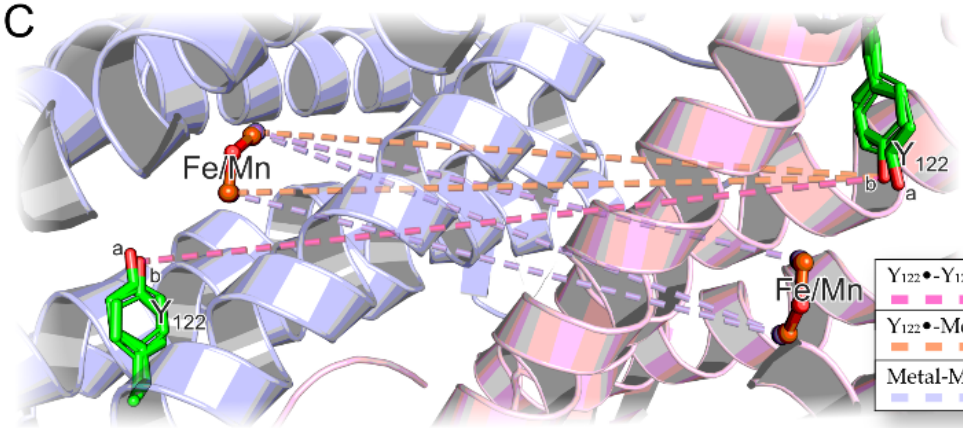

	Distance
Y_{122}•-Y_{122}•	3.21 nm
Y_{122}•-Metal	2.81-2.91 nm
Metal-Metal	2.53-2.56 nm

Figure 29: **A**: Table of potentially EPR-active species that can exist in β_2. **B**: β_2-subunit with zoom in on the active iron-bound center.[140] **C**: Potential distances in β_2. The protein structure of manganese-bound β_2[141] was overlaid with the structure of iron-bound β_2. Tyr_{122} a and b belong to the iron- and manganese-bound structure, respectively. Distances within the respective subunits are not shown as they are too short to be recorded with DEER.

4.1. Tyr-DEER

To study the effect of manganese mismetallation of RNR, the apo form of β_2 was exposed to manganese, followed by the addition of 5 eq. of iron. While other methods, such as UV-vis or quantitative CW-EPR, can provide information about the total amount of Tyr-radicals generated, DEER can provide information on the distribution of radicals in β_2.

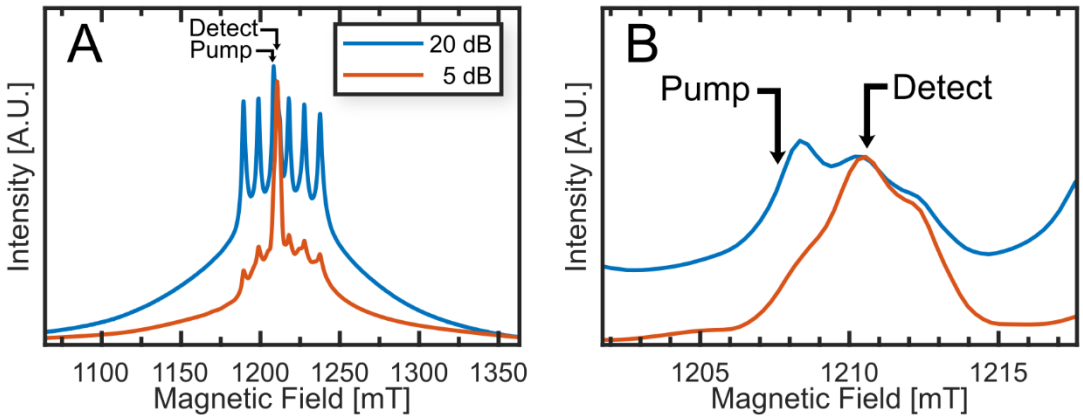

Figure 30: **A**: ESE- detected field-sweep of 1-Mn-5Fe:2h,[a] measured at 5 dB with long shot repetition time (highlighting the Tyr-signal) and 20 dB with short shot repetition time (highlighting the manganese signal) power. The pump and detect positions used for Tyr-Tyr DEER are indicated. **B**: Zoom in on the Tyr-signal.

Initial DEER measurements were taken at 1207.6 mT, 33.919 GHz, with the pump pulse offset by 84 MHz (Figure 30). When 1 eq. of Mn^{2+} is added before adding 5 eq. of Fe^{2+}, a Tyr-Tyr distance is observed (Figure 31a-b). The modulation depth increased over time as expected, since more Tyr• is produced, thus increasing the Tyr• to Mn^{II} signal ratio. However, after 2 h, a second minor distance started to manifest at around 2.85 nm (Figure 31b). This distance falls within the expected range for Tyr-Metal, based on crystal structures of β_2 (Figure 29c).[140,141] The same distance became more significant when the initially added amount of Mn^{2+} was increased (Figure 31c-d).

[a] All sample abbreviations are listed in Table 11

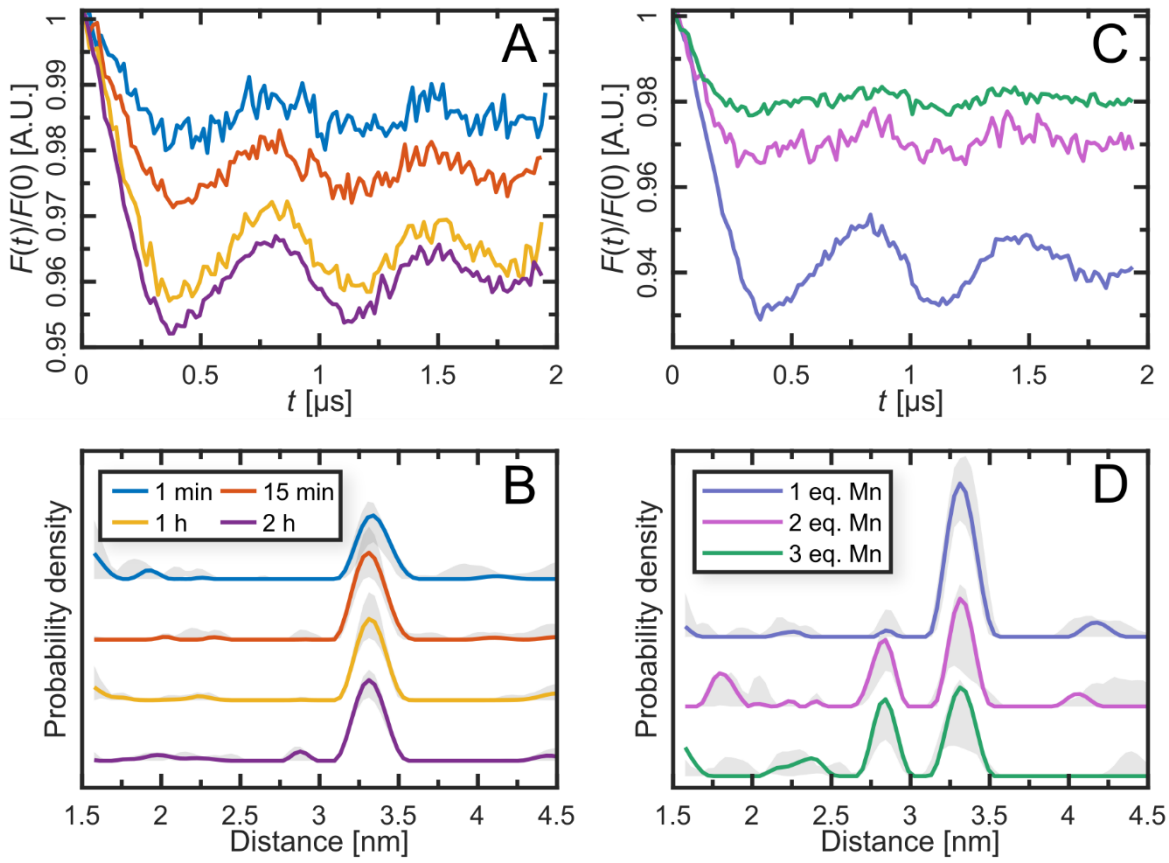

Figure 31: Tyr-Tyr DEER measured on 1-Mn-5Fe:1min,15min,1h,2h time series (A-B) and 1,2,3-Mn-5Fe:wash concentration series (C-D). **A&C**: Background corrected DEER traces. **B&D**: Distances with uncertainties as calculated by DEER-analysis given as the shaded area. Raw and dipolar spectra can be found in Chapter 5.3.

Since the diiron cofactor is strongly antiferromagnetically coupled and therefore basically EPR silent at 10 K,[100] the distance would have to arise from mono-Mn, di-Mn or FeMn. This would demonstrate that β_2 can be active even when one of its subunits contains manganese.

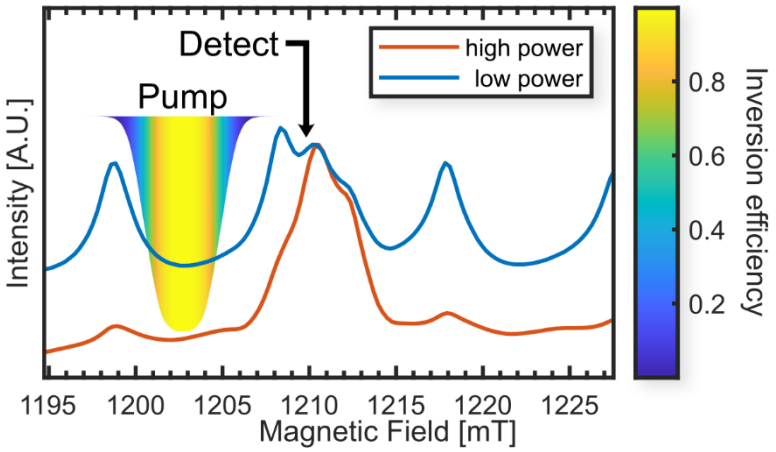

Figure 32: ESE-detected fieldsweep of 1-Mn-5Fe:2h, measured at low and high pulse power to highlight manganese and Tyr•. The position of the detection sequence used for Tyr-FeMn DEER is marked. The pump pulse is indicated by its inversion profile. The inversion profile was calculated with the EasySpin function exciteprofile.

To further probe this Tyr-metal distance, DEER with chirped pump pulses was employed in combination with utilizing the outer dip of the QTII resonator (Figure 47). The utilization of chirp pulses and the landscape of the QTII dip are discussed in more detail in Chapter 5.2. This allows for measurements with a much broader part of the spectrum (Figure 32).[137]

The Tyr-Metal distance measurements for the time series samples from Figure 31a-b are shown in Figure 33. The dipolar signal exhibits two prominent peaks; a lower-frequency one appearing at approximately 1.12 MHz can be assigned to Tyr-Tyr (Figure 33c). Seeing a minor Tyr-Tyr distance contribution is not unexpected, as the pump pulse has some light overlap with the low-field shoulder of the Tyr spectrum. The Tyr-metal to Tyr-Tyr ratio in the signal decreases over time, while the modulation depth increases significantly (Figure 33b). Therefore, the Tyr radical production in missmetallized and regular β_2 follows at least partially distinct pathways with different reaction speeds.

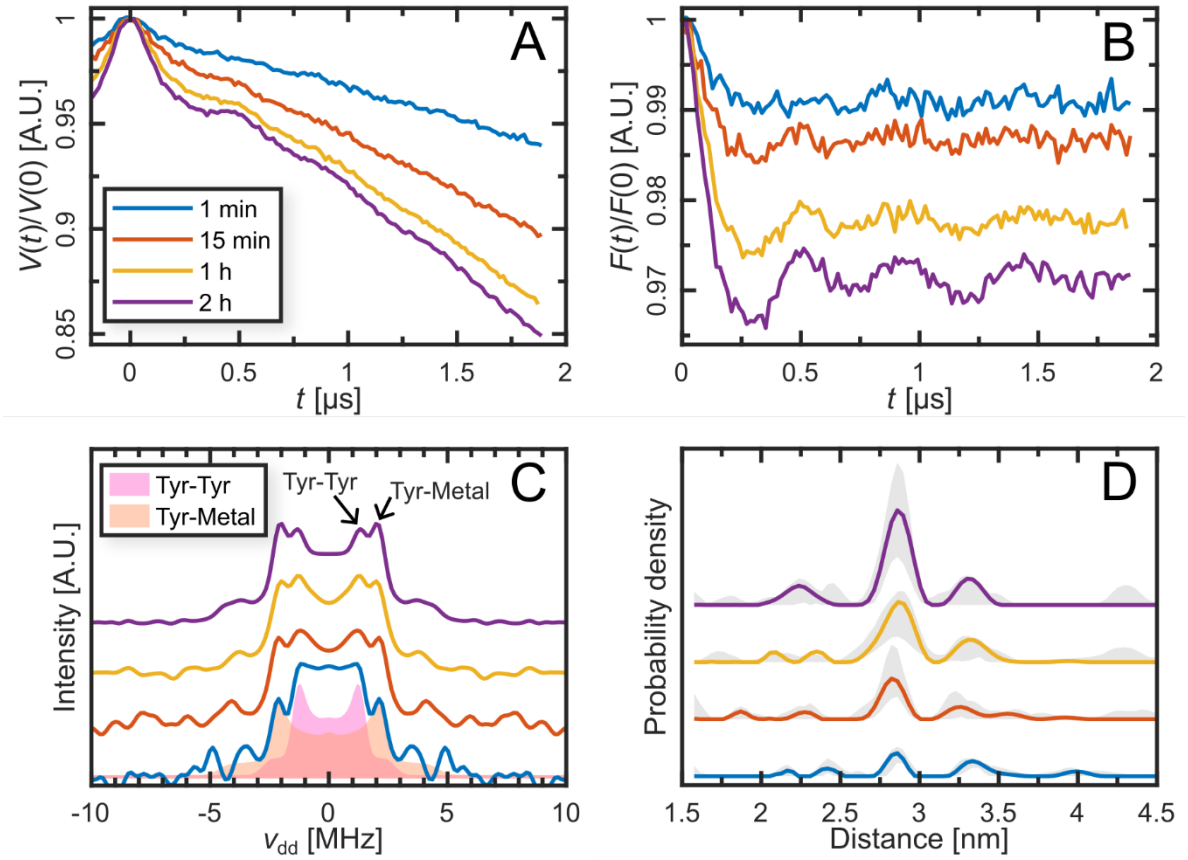

Figure 33: Tyr-Metal DEER measurements on 1-Mn-5Fe:1min, 15min, 1h, 2h. **A**: Raw DEER traces. **B**: Background corrected DEER traces. **C**: Dipolar spectra. The frequencies associated with the Tyr-Tyr and Tyr-Metal distance are marked. Furthermore, the dipolar spectra associated with the respective frequencies of each distance (taken from fit of 1 eq. Mn^{2+} sample in Figure 35) are shown. **D**: Results of distance analysis with uncertainty estimates.

However, this doesn't answer the question of which metal or metals are actually bound across from Tyr•. Since the di-manganese is also weakly antiferromagnetically coupled, meaning a significant portion of it is EPR silent at 10 K,[62] FeMn and mono-manganese would be the main suspects. With monochromatic pulses the flip angle Φ of a pulse is simply given by the Rabi freqeuncy and the pulse length as described in equation (*14*):[102,103]

$$\Phi = \gamma B_1 \sqrt{S(S+1) - m_s(m_s+1)} \cdot t. \quad (29)$$

Since FeMn is $S = 1/2$ while Mn^{II} is $S = 5/2$ the optimal pulse length/power for pumping Mn^{II} would be significantly lower at 44.72-33.33% (depending on the transition) of what is required for FeMn. However, for chirped pulses, the critical adiabaticity Q_{crit} of the pulse itself determines the flip angle, with the maximum flip angle for any species being 180°.[137,142,143]

$$\Phi = \arccos\left(2 \cdot \exp\left(-\frac{\pi}{2} Q_{crit}\right) - 1\right) \quad (30)$$

Therefore, FeMn and Mn^{II} cannot be distinguished by changing the pulse length of the chirped pump pulse. Of course, switching back to monochromatic pump pulses would solve this issue, but it would come at the cost of significantly reducing the pump bandwidth and, therefore, the modulation depth. Instead, RIDME spectroscopy can provide both an infinitely wide pump range and information on the spin of the metallic center.

Since RIDME uses T_1-relaxation for its B-spin flips, the B-spin is not limited to $|\Delta m_s| = 1$ transitions like in DEER. Therefore, species with $S > 1/2$ will generate overtones where multiples of the dipolar frequency are recorded as the B-spin undergoes $|\Delta m_s| = 2,3,\ldots$ transitions.[144] As expected, RIDME did provide a significant improvement in modulation depth compared to chirped DEER (Figure 34a-b). However, the much longer pulse sequence also limits the length of the trace and signal-to-noise compared to chirped DEER. Still, the RIDME measurement clearly shows overtones caused by manganese (Figure 34c-d).

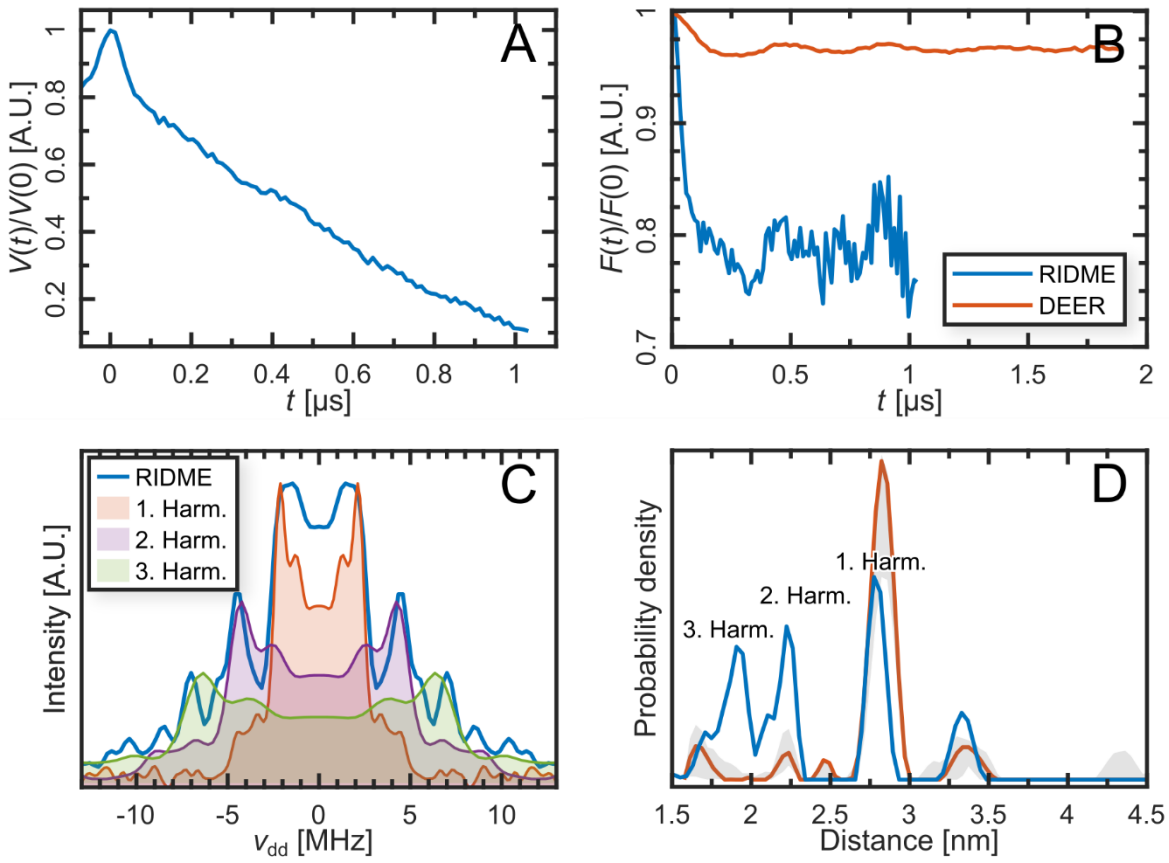

Figure 34: Tyr-Metal RIDME measurements on 2-Mn-5Fe:wash **A**: Raw RIDME trace. **B**: Background corrected RIDME trace with the corresponding DEER trace from Figure 35 plotted for reference. **C**: Dipolar spectrum. The corresponding dipolar spectrum from DEER, as well as the DEER spectrum scaled up to double and triple the frequency (1,2,3. Harm.), are plotted to illustrate the overtones present in the RIDME spectrum. **D**: Results of distance analysis with distances resulting from the overtones highlighted.

A modified version of DEER analysis (OvertoneAnalysis)[145] that takes these overtones into account exists, but, it was not able to properly fit the signal. This makes sense if a combination of Mn^{II} and FeMn generates the signal, as OvertoneAnalysis is not able to take combinations of different species into account. However, the RIDME signal also contains some, although minor Tyr-Tyr distance, which might also explain why OvertoneAnalysis didn't work.

To gain further insight into manganese binding, Tyr-Metal DEER was measured on the samples with 1,2,3 eq. Mn^{2+} + 5 eq. Fe^{2+} as well (Figure 35). The modulation depth changes comparatively little (Figure 35b) with the 1 eq. Mn^{2+} sample showing a significant amount of Tyr-Tyr signal (Figure 35c). However, of the three samples, the 2 eq. Mn^{2+} sample clearly has the strongest Tyr-Metal signal. This stands in contrast to the Tyr-Tyr DEER measurements (Figure 31d), where the intensity of the Tyr-Metal distance compared to the Tyr-Tyr distance was largest for the 3 eq. Mn^{2+} sample.

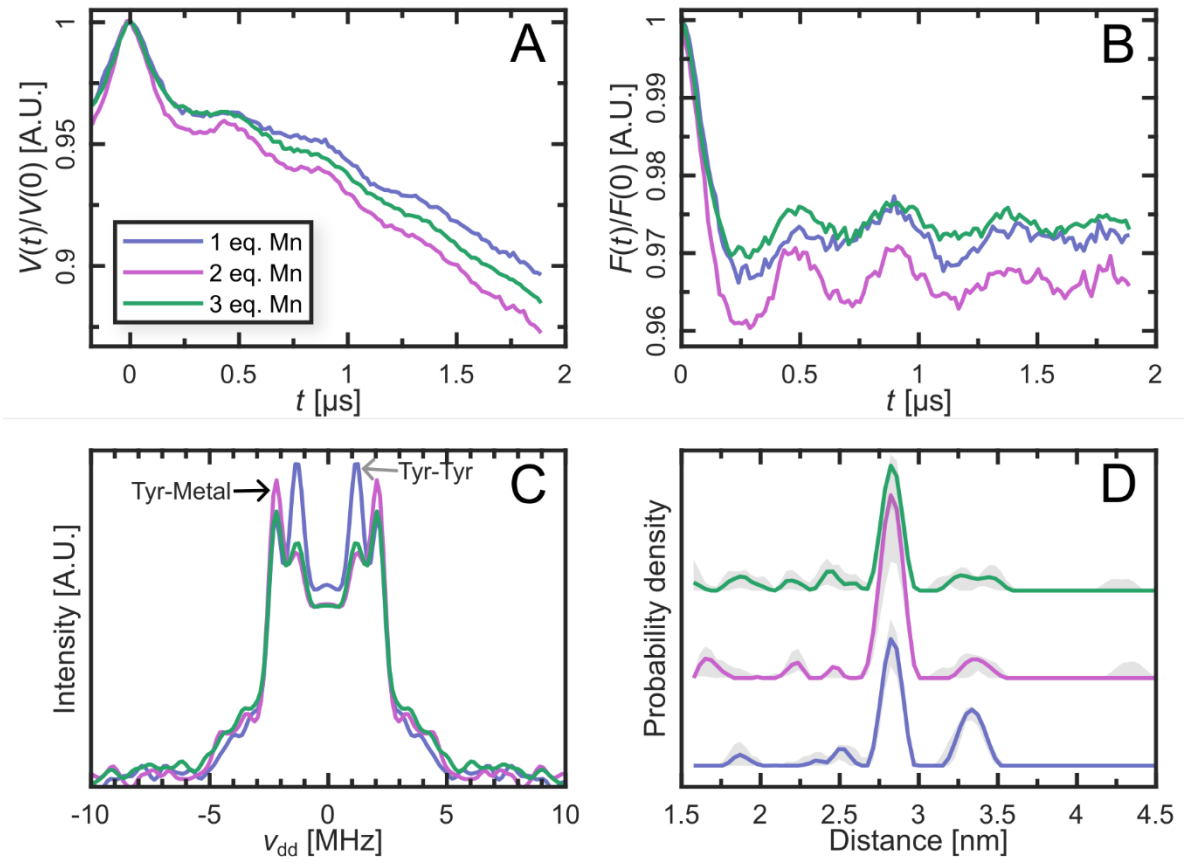

Figure 35: Tyr-Metal DEER measurements on 1,2,3-Mn-5Fe:wash **A**: Raw DEER traces. **B**: Background corrected DEER traces. **C**: Dipolar spectra. **D**: Results of distance analysis with uncertainty estimates.

Under the assumption that the Tyr-Metal distance was solely the result Tyr-Mn^{II} the intensity ratios b_I (Tyr-Tyr DEER) and b_{II} (Tyr-Metal DEER) are described by the following expressions, with the concentrations c and signal factors a which describe how much signal contribution is generated per concentration in each respective experiment:

$$b_{I,2} = \frac{a_{Mn,I} \cdot c_{Mn,2}}{a_{Tyr,I} \cdot c_{Tyr,2}} \quad b_{II,2} = \frac{a_{Mn,II} \cdot c_{Mn,2}}{a_{Tyr,II} \cdot c_{Tyr,2}}$$
$$b_{I,3} = \frac{a_{Mn,I} \cdot c_{Mn,3}}{a_{Tyr,I} \cdot c_{Tyr,3}} \quad b_{II,3} = \frac{a_{Mn,II} \cdot c_{Mn,3}}{a_{Tyr,II} \cdot c_{Tyr,3}} \tag{31.1}$$

$$\frac{b_{I,2}}{b_{I,3}} = \frac{c_{Mn,2}}{c_{Mn,3}} \cdot \frac{c_{Tyr,3}}{c_{Tyr,2}}$$
$$\frac{b_{II,2}}{b_{II,3}} = \frac{c_{Mn,2}}{c_{Mn,3}} \cdot \frac{c_{Tyr,3}}{c_{Tyr,2}}. \tag{31.2}$$

Therefore, the signal ratios should change in the same fashion for both experiments. However, assuming the Tyr-Metal distance to be a combination of Tyr-Mn^{II} and Tyr-FeMn, the following equations are generated:

$$b_{I,2} = \frac{a_{Mn,I} \cdot c_{Mn,2} + a_{FeMn,I} \cdot c_{FeMn,2}}{a_{Tyr,I} \cdot c_{Tyr,2}} \quad b_{II,2eq} = \frac{a_{Mn,II} \cdot c_{Mn,2} + a_{FeMn,II} \cdot c_{FeMn,2}}{a_{Tyr,II} \cdot c_{Tyr,2}}$$
$$b_{I,3} = \frac{a_{Mn,I} \cdot c_{Mn,3} + a_{FeMn,I} \cdot c_{FeMn,3}}{a_{Tyr,I} \cdot c_{Tyr,3}} \quad b_{II,3eq} = \frac{a_{Mn,II} \cdot c_{Mn,3} + a_{FeMn,II} \cdot c_{FeMn,3}}{a_{Tyr,II} \cdot c_{Tyr,3}} \tag{32.1}$$

$$\frac{b_{\mathrm{I},2}}{b_{\mathrm{I},3}} = \frac{a_{\mathrm{Mn,I}} \cdot c_{\mathrm{Mn},2} + a_{\mathrm{FeMn,I}} \cdot c_{\mathrm{FeMn},2}}{a_{\mathrm{Mn,I}} \cdot c_{\mathrm{Mn},3} + a_{\mathrm{FeMn,I}} \cdot c_{\mathrm{FeMn},3}} \cdot \frac{c_{\mathrm{Tyr},3}}{c_{\mathrm{Tyr},2}}$$
$$\frac{b_{\mathrm{II},2}}{b_{\mathrm{II},3}} = \frac{a_{\mathrm{Mn,II}} \cdot c_{\mathrm{Mn},2} + a_{\mathrm{FeMn,II}} \cdot c_{\mathrm{FeMn},2}}{a_{\mathrm{Mn,II}} \cdot c_{\mathrm{Mn},3} + a_{\mathrm{FeMn,II}} \cdot c_{\mathrm{FeMn},3}} \cdot \frac{c_{\mathrm{Tyr},3}}{c_{\mathrm{Tyr},2}}. \quad (32.2)$$

In this case, the ratios of the ratios no longer have to be the same. Therefore, by combining measurements with different signal factors and samples with different concentrations, it is possible to differentiate between cases of a single B-spin species or multiple B-spin species, even if those give the same distance. If β_2 were able to produce both Tyr• while carying a missmetelated center DEER would not only record the freqency from the dipolar interaction of the A-spin to both B-spins but also the sum or difference of these interactions when both B-spins are pumped (equation (*24*)). Since neither the Tyr-Tyr nor Tyr-Metal measurements show any of these combinations of frequencies, it can be concluded that β_2 can only produce both Tyr• if metalated correctly or at most one Tyr• when missmetalated. Therefore, the `two or none` model fails when manganese is introduced. Furthermore, Tyr• production does not require the correct loading of the opposing β-subunit. Therefore, a reexamination of manganese binding behavior is in order.

4.2. Mn-Mn DEER

While the manganese loading of β_2 has been studied by quantitative CW before,[61–63] dedicated studies of the loading of manganese in oposing β-subunits are still missing. These studies suggested that single manganese binding to a β-subunit blocks binding in the second subunit. However, DEER measurements, presented here, show compelling evidence that binding in both sides is not only possible but preferred. Multiple concentration series with different preparation methods were prepared (Table 11).

All 1 eq. samples, regardless of preparation method, showed almost exclusively bound manganese (Figure 36a), lacking any of the resolved hyperfine splittings expected from free manganese. Meanwhile, samples with 2 eq. manganese and restricted access to oxygen start to show free manganese (Figure 36b). Finally, all samples show clear free manganese signals at 3 eq.

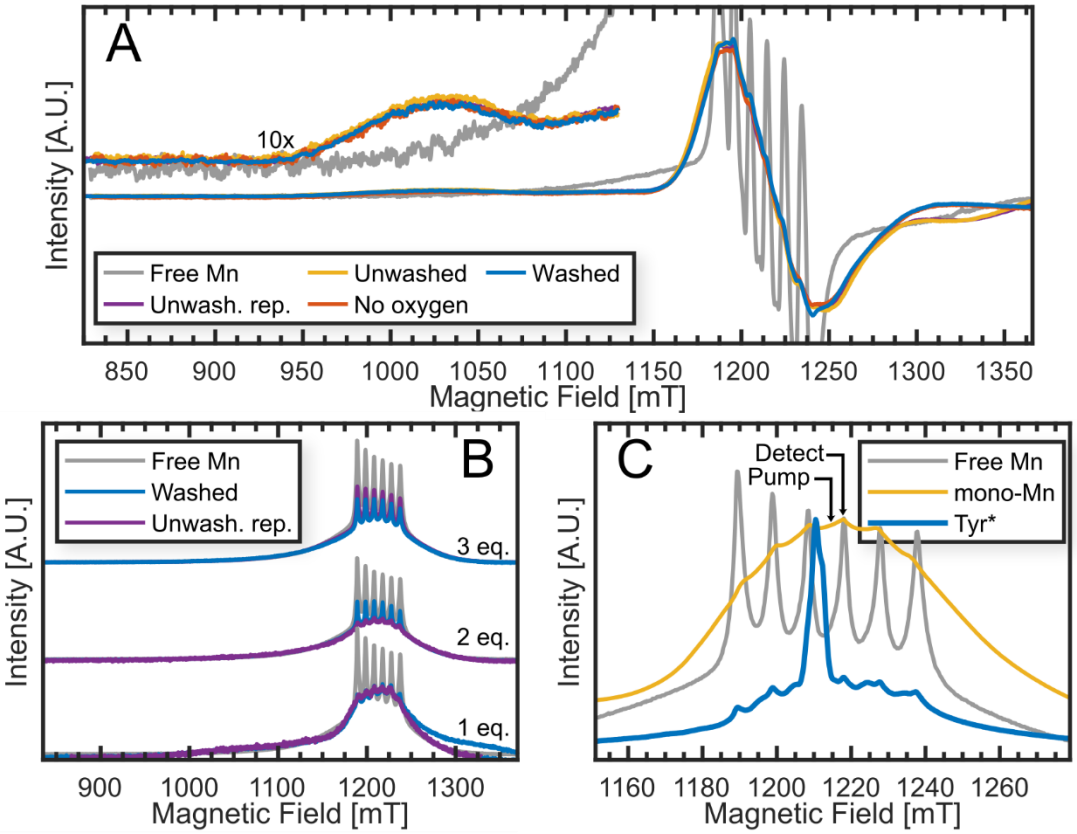

Figure 36: **A**: 4 dB ESE-detected fieldsweeps of 1 eq. manganese samples from each concentration series and free manganese. The spectra were normalized to the left shoulder (1123-1172 mT), and pseudo-modulated with a modulation amplitude of 8 mT. **B**: 20 dB ESE-detected fieldsweeps of 1,2,3-Mn:wash as well as 1,2,3-Mn:rep. All spectra were normalized by maximizing the left shoulder (900-1160 mT). **C**: ESE- detected fieldsweep of free manganase, 1-Mn:rep recorded at low power to highlight the mono-manganese signal, and 1-Mn-5Fe:2h measured at 4 dB to highlight the Tyr-signal. The pump and detect positions used for Mn-Mn DEER are indicated.

DEER was measured on the fourth peak of the manganese spectrum (Figure 36c). This position was chosen because it covers the maximum of the mono-manganese signal while also avoiding the Tyr•-signal. Some Mn-Mn DEER measurements showed an unexplained artefact that could not be removed by phase-cycling. The steps taken to remove the artefact are discussed in Chapter 5.4.2.

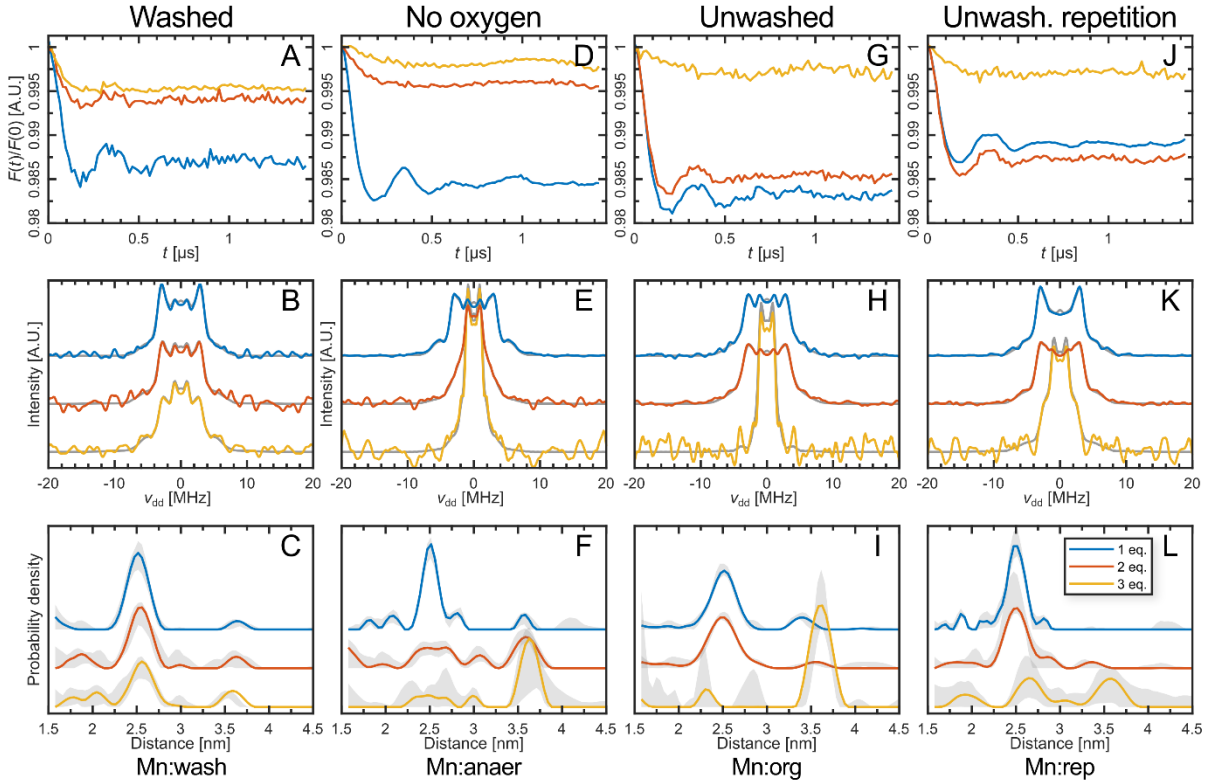

Figure 37: Mn-Mn DEER measurements on β_2 with 1, 2 & 3 eq. Mn^{2+} added. **A-C**: The samples were washed after the addition of manganese to remove free manganese. Buffer was bubbled through with nitrogen gas. **D-F**: Samples were prepared anaerobically in a glovebox but not washed. **G-L**: Samples were prepared without washing or any measures to restrict oxygen access. **Top row**: Background corrected DEER traces. **Middle row**: Dipolar spectra with fits indicated in grey. **Bottom row**: Distance distributions with uncertainty estimates.

All 1 eq. samples showed a distance of about 2.52 nm, which is within the range expected for a Mn-Mn distance based on crystal structures (Figure 37).[141] The modulation depths all fall into a range of 1.1-1.7%. For comparison, $MnDOTA_2OPE$, a manganese ruler, was measured with DEER, to give an estimation on the maximum achievable modulation depth. This resulted in a modulation depth of 1.9%, which is not significantly larger than the ones measured for β_2. Supporting information on the manganese ruler, and it providing a good estimate on the maximum modulation depth expected for β_2-bound manganese, is outlined in Chapter 5.4. At 2 eq., the modulation depth decreases significantly for both the washed and anaerobic samples, while it barely changes for the samples with unrestricted oxygen access. Finally, at 3 eq. all samples show very low modulation amplitudes. It was previously established by parallel and perpendicular CW that manganese mainly binds as mono-manganese at 1 eq. and mainly binds as di-manganese at 2 eq. manganese, if added under similar anaerobic conditions.[62] As di-manganese is mostly EPR silent at 10 K, that would explain the lack of modulation at 2/3 equivalents. Furthermore, all samples start to display an undefined signal at 0.88 MHz with higher manganese equivalents. This signal is less prevalent in the washed samples. The origin of this signal is currently unclear. No nucleus would produce an ESEEM artefact at this frequency, and the resulting distance of 3.6 nm also doesn't correspond to any known manganese binding site. Since manganese displays barely any *g*-anisotropy, selection orientation effects are also unlikely to be the reason.

This data shows that manganese not only can occupy both β-subunits but prefers to do so. However, both previous studies as well as TXRF measurements on the washed samples (internal communications), show that at the very most 2 equiv. of manganese is bound to β_2. Previously, this was explained by the binding of manganese to one subunit, blocking binding to the second subunit.[62] However, taking the Mn-Mn DEER results into account, this explanation cannot hold true. Therefore, some factor must exist that blocks some β_2 units, similar to how the maximum amount of active β_2, when combined with iron, is limited.

Continuing the study of manganese loading, Mn-Mn DEER was measured on the 1-Mn-5Fe series (Figure 38). Surprisingly, the Mn-Mn signal vanishes immediately upon iron addition, with only a very small amount of signal being recovered over time. However, at the same time, the background density increases, indicating that the total amount of EPR-active manganese also increases. Since both mono-manganese and free manganese contribute to the background density, the increase in manganese must originate from di-manganese being released.

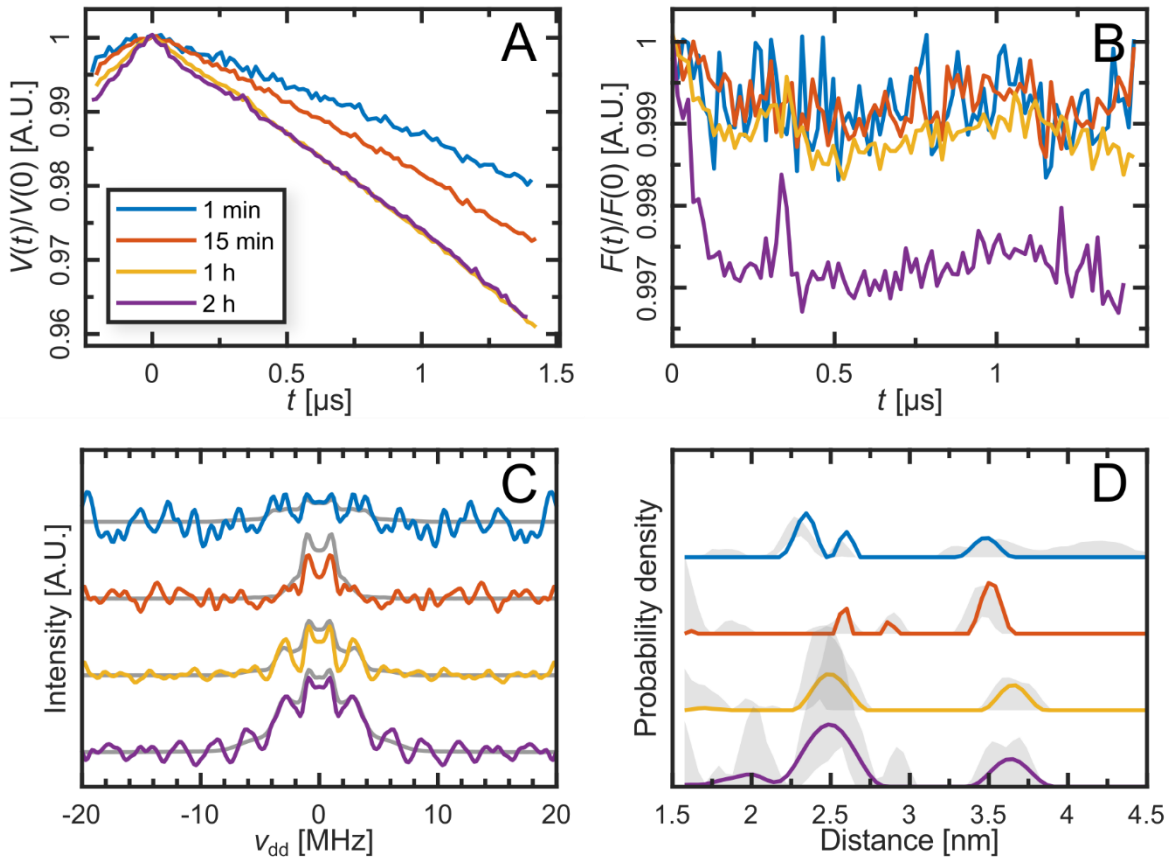

Figure 38: Mn-Mn DEER measurements on 1-Mn-5Fe:1min,15min,1h,2h. **A**: Raw DEER traces. **B**: Background corrected DEER traces. **C**: Dipolar spectra with the fits from distance analysis in grey. The fit for 1 eq. was scaled down by a factor of 5 due to its very poor quality. **D**: Results of distance analysis with uncertainty estimates.

The same loss of Mn-Mn signal (2.5 nm) is observed for 2 and 3 eq. of Mn^{2+} (Figure 39), with the 1,2,3-Mn-5Fe:wash series showing that even at high manganese concentrations, the presence of iron prevents the simultaneous binding of mono-manganese in both β-subunits.

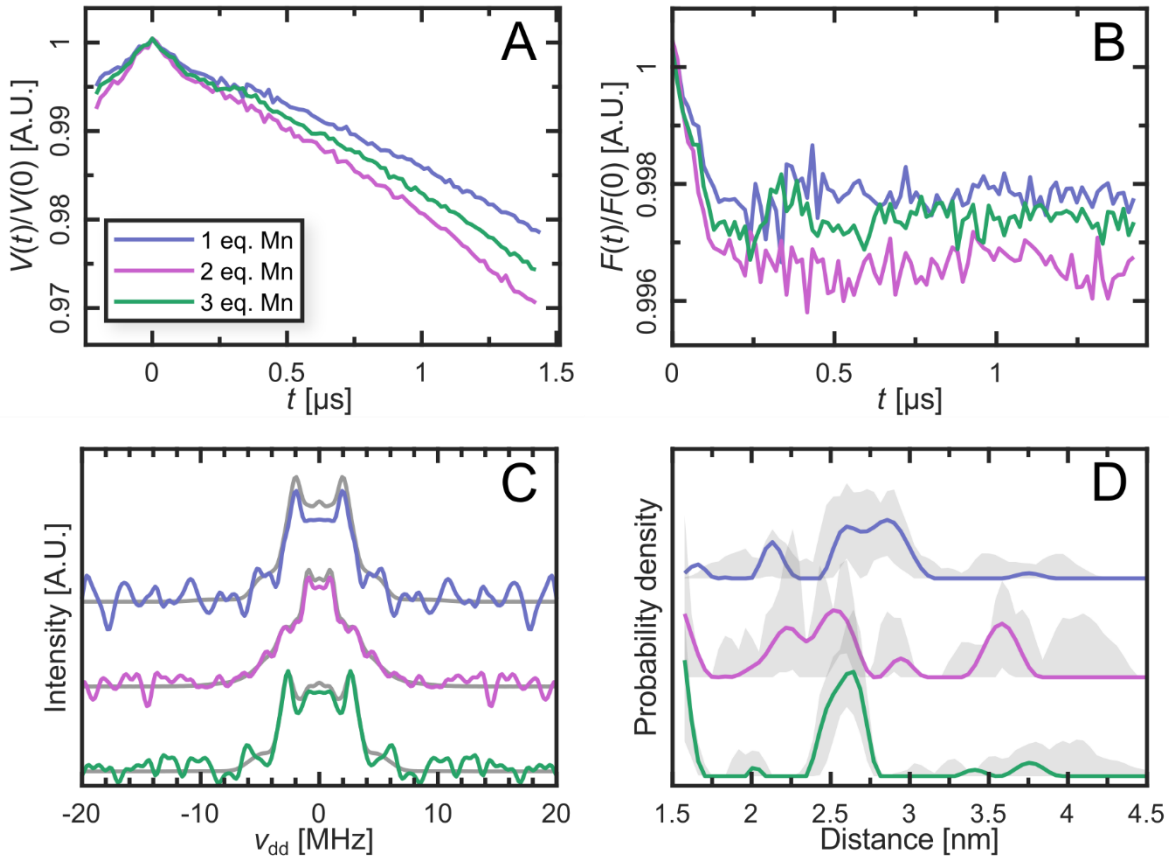

Figure 39: Mn-Mn DEER measurements on 1,2,3-Mn-5Fe:wash. **A**: Raw DEER traces. **B**: Background corrected DEER traces. **C**: Dipolar spectra. **D**: Results of distance analysis with uncertainty estimates.

This rapid removal of mono-manganese from at least one β-subunit demonstrates that, even though manganese loading of apo-β_2 inhibits activity, β_2 still possesses a partial recovery mechanism. However, to get the full picture of what happens to mono-Mn, DEER needs to be combined with field-swept spectra.

4.3. Power-dependent field sweeps

Power-dependent ESE-detected field-sweeps can provide further insights into the binding of manganese. Unlike with spin ½ species, where a single optimal pulse length/power combination exists, S >½ species have multiple optimal values depending on the transition. This can be exploited to enhance or suppress features of the spectrum. The measurements shown in this chapter were measured at two different machines. Measures taken to ensure comparability of measurements between devices are discussed in Chapter 5.1. Whenever microwave power is discussed, it is referred to by the power used at the XQ-band machine. A conversion table can be found in chapter 5.1.1. Due to the effective power dropping off more rapidly for the XQ-band from 1250 mT upwards, the right shoulder of the manganese signals cannot be matched. However, the data analysis presented here focuses on the main signal and the left shoulder, which are not affected.

Since free manganese has a comparatively symmetric environment, its $m_s = -1/2 \rightarrow 1/2$ transition displays sharp, well-resolved lines (Figure 40).

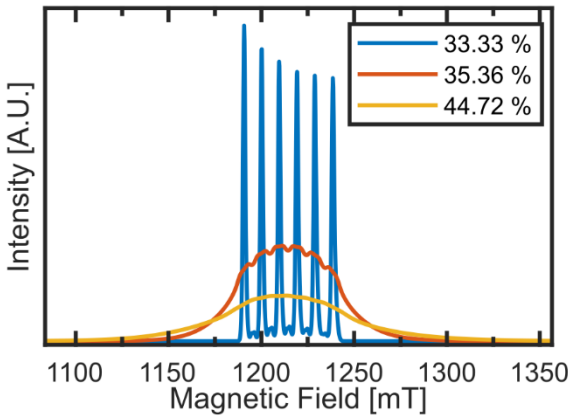

Figure 40: Simulation of the respective transitions of free Mn^{2+} ($\pm 5/2 \leftrightarrow \pm 3/2$ in yellow, $\pm 3/2 \leftrightarrow \pm 1/2$ in orange and, $-1/2 \leftrightarrow +1/2$ in blue). The transitions are labeled based on their preferred optimal pulse length/amplitude. 100% is assigned to the optimum for a $m_s = -1/2 \leftrightarrow +1/2$ of a *S*=1/2 system.[102]

To optimally highlight the $m_s = \pm 1/2$ transition, a power of 20 dB, which is lower than the optimal power, was selected. While underrotating the $m_s = \pm 1/2$ transition does reduce its signal intensity, the intensity of the other transitions is reduced more, leading to a relative increase in the $m_s = \pm 1/2$ transition intensity (Figure 53).

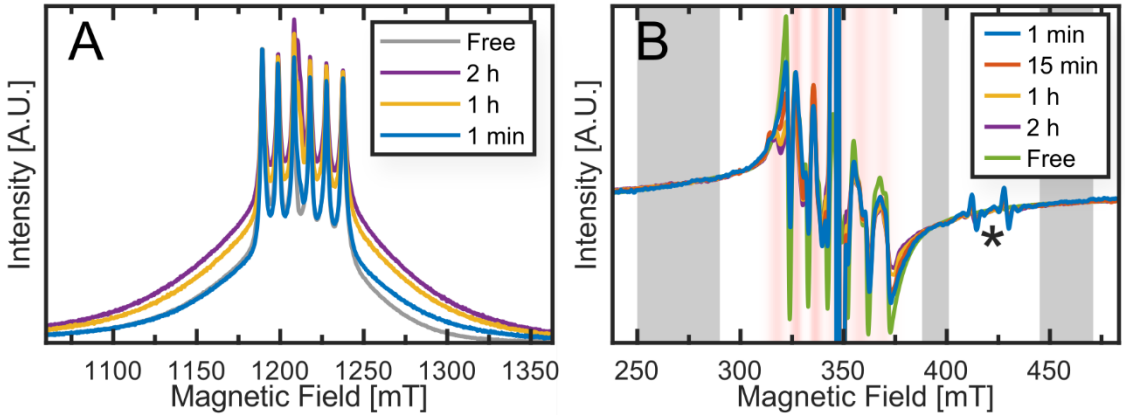

Figure 41: **A**: ESE detected field-sweeps of 1-Mn-5Fe:1min,15min,1h,2h, recorded at 20 dB and 10 K. All samples mostly display the narrow lines associated with free Mn^{2+}. Spectra are normalized to the height of the first peak. Additionally, a spectrum of free Mn^{2+} is plotted in grey for comparison. (Not normalized data in Figure 42b) **B**: CW measurements of the time series samples and a sample of free Mn^{2+} in buffer recorded in X-band at 15 K, with a modulation amplitude of 0.8 mT. The red shaded regions indicate the area where the FeMn signal is found (shading intensity equals the intensity of the signal). The FeMn signal was simulated based on the parameters measured by Pierce et al.[62] using the easyspin function pepper.[146] The spectra were scaled using the grey regions, as these regions only contain the free manganese signal. An asterisk marks a background signal. The measurements were recorded by Sergius Boschmann.

Comparing the 20 dB measurements, the 1 min signal is virtually identical to the signal of free manganese (Figure 41a). Furthermore, the signal is significantly lower at 1 min, indicating that some manganese is still being released. This is further supported by X-band CW measurements (Figure 41b). By scaling the shoulders of the spectrum where no FeMn signal is present, the amount of free manganese can be calculated. A release of 45, 65, 99 & 100% of manganese (relative to the final released amount) can be calculated. Compared to free manganese the bound mono-Mn has a highly asymetric enviorment. This results in a large zero-field splitting, which is visible as broad shoulders in the spectrum. One such shoulder

can be observed quite well around 1025 mT. However, no such signal is visible at any time step (Figure 42a). Therefore, the manganese that is slowly released following the addition of Fe^{2+} must originate from di-manganese. This also means that the observed Tyr-Metal distance most likely does not stem from mono-Mn as one would expect to see at least some kind of signal. This leaves di-Mn and FeMn as the more likely candidates. While no identifiable features of di-Mn in pulsed Q-band could be found for any sample, this might simply be the result of broadening and too short T_2-times. However, as the B-spin only needs to be flipped to act as a B-spin, di-Mn would still be detectable in DEER, even though it would be underrepresented, as the fraction in the $S = 0$ manifold cannot be flipped. It should be noted that in a repetition series of 1-Mn-5Fe:1min,15min,1h,2h, the mono-Mn signal was still detectable at 1 min. However, the signal had completely vanished at 15 min and likely falls within the inherent variation between batches (Figure 55). In the repetition, another 5 eq. Fe^{2+} were added after 2 hours, which led to another rapid release of manganese followed by another slower release.

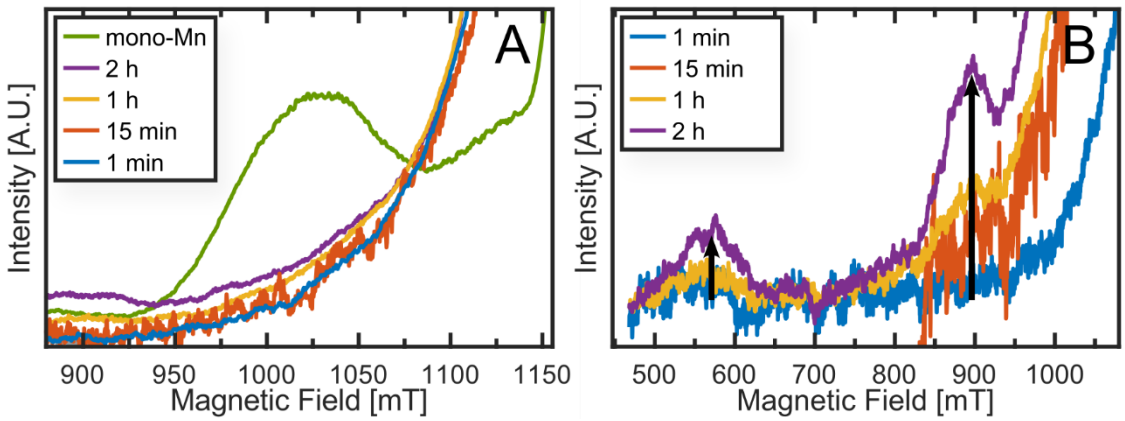

Figure 42: ESE-detected Q-band field-sweeps of 1-Mn-5Fe:1min,15min,1h,2h recorded at 10 K. **A**: Zoom in on the mono-Mn feature, recorded at 4 dB, pseudomodulated (20 mT). Additionally, to the time series, 1-Mn:wash is plotted, showing the characteristic mono-Mn signal. **B**: Zoom in on additional signal, recorded at 8 dB, displayed as first derivative (20 mT modulation amplitude).

An additional minor signal, which can neither be attributed to mono-manganese, di-manganese, free manganese, or $Fe^{III}Mn^{III}$ grows in with time (Figure 42b).

Furthermore, a FeMn feature consistent with previously reported $Fe^{III}Mn^{III}$ can be extracted at high pulse power (Figure 43a). Since the signal overlaps with the broad shoulder of free manganese, the second-order derivative was taken. This suppresses the broader contributions from manganese to the signal. Three points were chosen and scaled to each other by taking the mean of the intensity ratios between each point. The averages of the three values are shown in Figure 43c. When comparing the background density of Mn-Mn DEER (Figure 43c) with the FeMn concentration, the two match almost perfectly (Figure 43d). Therefore, the signal in the pumped region is dominated by FeMn. Still, the DEER measurements barely show any modulation depth, increasing only at the two-hour mark, while the amount of FeMn linearly increases from 15 min onwards. If FeMn could form in both β-subunits at the same time, one would expect it to contribute to the Metal-Metal DEER signal. Since it does not, FeMn seems to form exclusively in one of the two β-subunits.

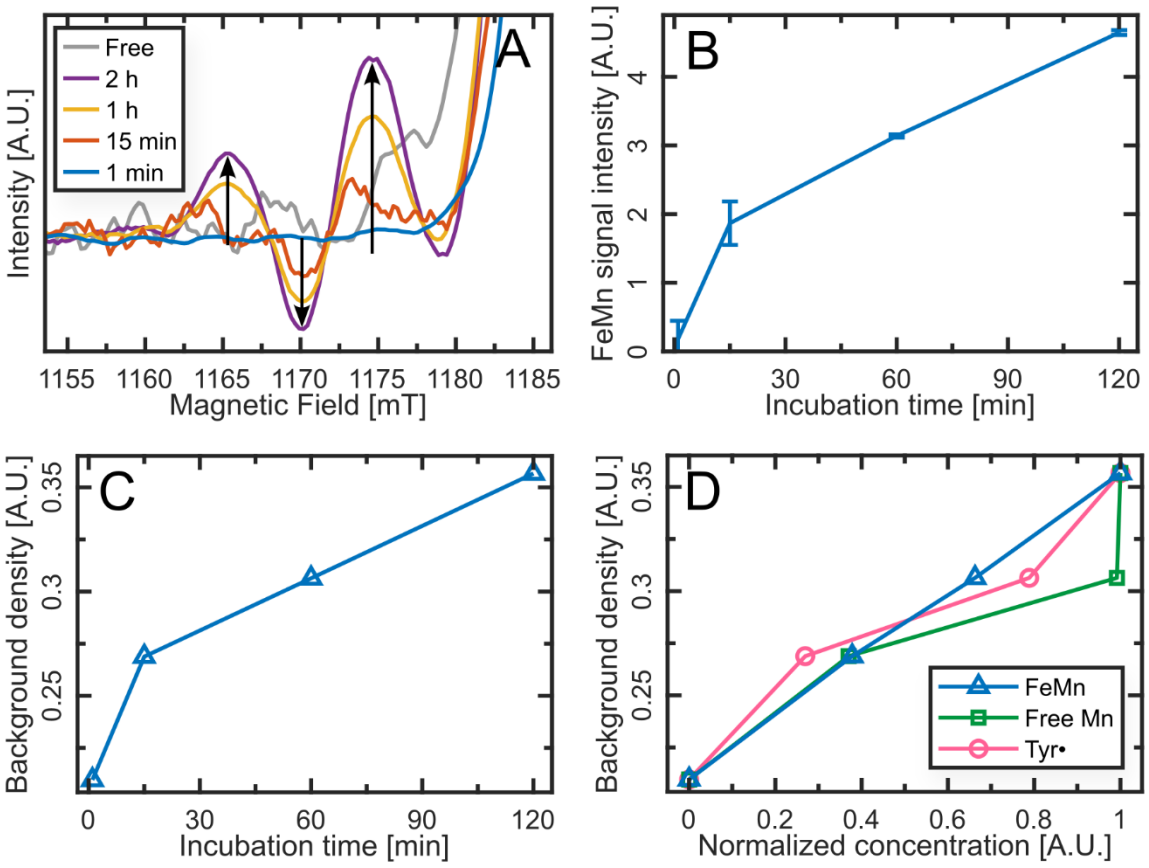

Figure 43: **A**: ESE-detected Q-band field-sweeps of 1-Mn-5Fe:1min,15min,1h,2h, recorded at 10 K. Zoom in on the FeMn feature recorded at 4 dB. Spectrum is shown as second derivative (4 mT modulation amplitude) to suppress the broader shallow shoulders of manganese. Arrows indicate the growth of signal. **B**: Intensity of the FeMn feature, calculated as the scaled mean value of the three features marked in (a). The scaling factors for the respective features were calculated as the mean value of the relative intensities of the features in the 1 & 2 h samples. **C**: Background densities of Mn-Mn DEER (Figure 38) as calculated by DEERanalysis. The values were corrected for variations in background order to align with the concentration-dependent expression for background density. **D**: Same background densities plotted against the concentration of FeMn, free manganese as calculated in Figure 41, and Tyr• as determined by previously established protocols.[147] The concentrations were rescaled to a range of 0 to 1 for better comparison.

Since FeMn is only formed slowly over time, the formation of FeMn from mono-Mn can be ruled out. The slow incorporation of Fe^{2+} in already Mn-loaded β_2 can be ruled out due to Fe^{2+} not being stable in solution if exposed to oxygen. It would rather seem that either mismetallated β_2 only forms Tyr• very slowly or manganese slowly incorporates into iron-bearing β_2, either displacing Fe or filling up spots in not fully loaded β_2.

In addition to the known $Mn_{(aq)}$, mono-Mn, and FeMn signals, another signal grows in over time (Figure 42b). Since the same signal can be extracted from samples with no iron added (Figure 44c-d), it being another FeMn species or generated when the tyrosyl radical forms can be ruled out. It is also more predominant in the 2 and 3 eq. Mn (no Fe) samples. However, if the signal were to stem from di-Mn it would not grow in but rather diminish over time. Therefore, a definite assignment of the signal is at this moment not possible.

The mono-Mn signal in the Mn-concentration series (Figure 44a) correlates with the Mn-Mn DEER signal (Figure 37). The sample prepared under completely anaerobic conditions shows

no more mono-Mn peak once more than 1 eq. of manganese is added. Meanwhile, in the samples prepared with unrestricted oxygen access, the signal persists up to 2 eq. just like the DEER signal. Finally, the sample, which was washed and prepared in buffer with nitrogen gas bubbled through, shows a loss of signal at 2 eq. but never loses its mono-Mn signal fully even at 3 eq. This also fits the DEER data, as it is the only sample where, despite a significantly reduced modulation amplitude, the Mn-Mn distance still dominates the dipolar spectrum at 3 eq (Figure 37a-c). The reason why mono-Mn can still be found at higher concentrations is probably that the washing step removes some bound manganese. Finally, the FeMn signal is only seen in the sample where iron was added, where it was almost identical for 2 and 3 eq. Mn.

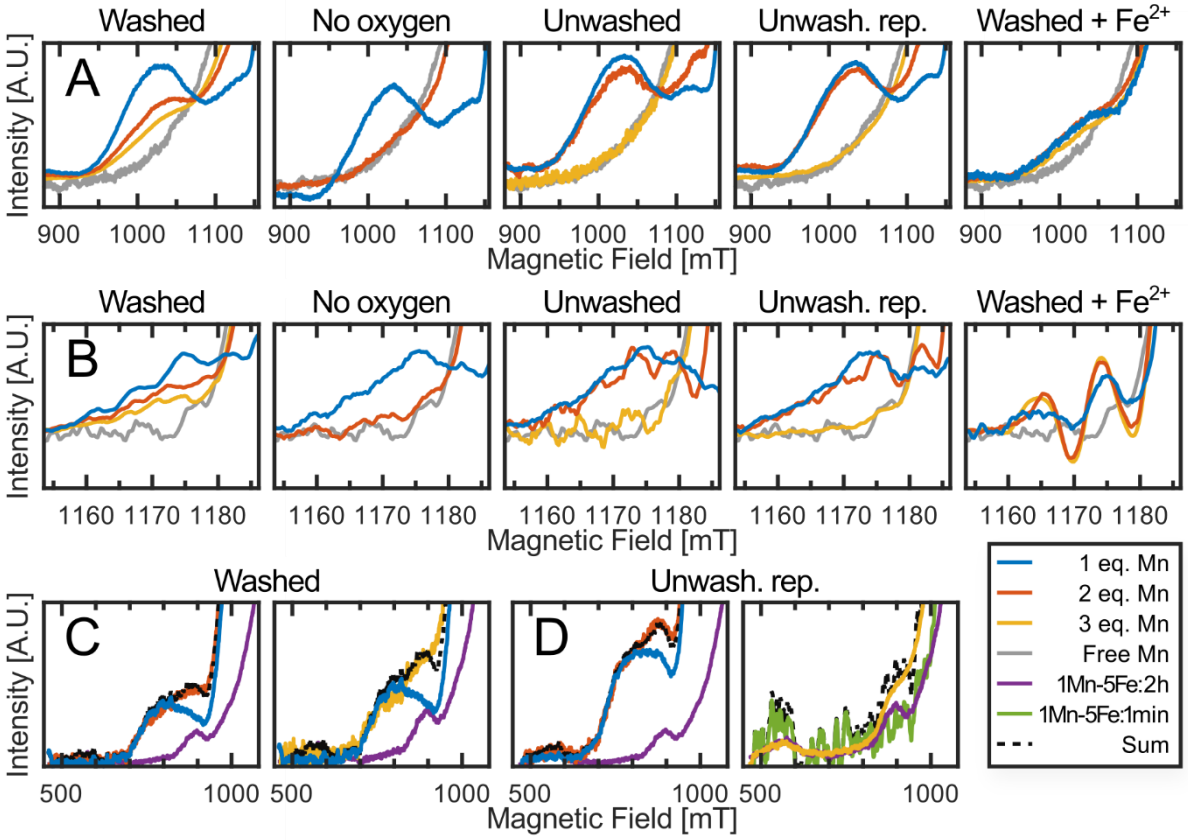

Figure 44: Zoom in on ESE-detected field-swept spectra of the manganese concentration series samples. **A**: Comparison of mono-Mn feature, measured at 4 dB, 20 mT pseudomodulated. **B**: Second-order pseudomodulated (4 mT) zoom on the FeMn signal region. **C**: Zoom in on the mono/di-Mn signal region, of the washed Mn concentration series, 20 mT pseudomodulated. Shown are the 1 eq spectrum, 2/3 eq. spectrum and how the sum of the 1 eq. spectrum and the 2 hour 1 eq Mn + 5 Fe spectrum can construct the 2/3eq. spectrum respectively. **D**: Same as C for the unwashed repetition samples. instead of the 1 eq. Mn sample the spectrum from the 1 min 1 eq Mn + 5 Fe sample is used.

4.4. Conclusions

In conclusion, this data is in agreement with previous CW-studies, which showed that manganese first binds as mono-Mn and only starts to bind as di-Mn at higher concentrations once no more binding as mono-Mn is possible. However, these studies misinterpreted the substoichiometric maximum uptake of manganese as an allosteric effect between the subunits, which limits manganese binding to one of the two β-subunits. But the combination with DEER data shows that manganese can incorporate into both subunits and uptake is actually limited

by only a portion of β_2 being able to incorporate manganese. What excatly triggers som β_2 being able to take up manganese and some not is not yet known. However, this behavior is somewhat reminiscent of the in vitro Tyr• production of β_2, where at most 60% of β_2 are active and only at most 3.6 eq. of iron are bound by β_2, regardless of Fe^{2+} availability.[59,60] Access to oxygen increases the amount of β_2 available to bind manganese. Since mono-Mn seems to be removed from β_2 much more rapidly when iron becomes available, favoring the binding of mono-Mn over di-Mn might help β_2 to recover from manganese mismetabolization. The addition of iron is followed by a slow release of di-Mn which plateaus after about an hour. At the same time FeMn is produced, however, the production of FeMn continues after the release of free manganese has stopped, indicating that FeMn is not simply created by Fe^{2+} replacing one manganese in di-manganese. Adding a second batch of iron results in another rapid release of manganese, followed by a period of slow release. As the second rapid release coincides with a temporary drop in FeMn signal (internal communications), the second rapid release of manganese may be due to manganese from FeMn being released.

Furthermore, it was found that FeMn can only be generated in one of the β-subunits. Tyr• can form in subunits opposite to subunits carrying FeMn, but it is required for FeMn formation. Furthermore, Tyr• cannot be produced in the same subunit as FeMn. Finally, Tyr• can also be created in subunits opposite of di-Mn.

4.5. Materials and methods

4.5.1. Sample preparation

All β_2 samples were prepared by Viktoria Glocke and Shari Meichsner. Apo-β_2 was produced following the protocol previously established by the Kasanmascheff lab[147] and samples were prepared in 5% (v/v) Glycerol and 50 mM Tris Buffer at a pH of 7.6. With the exception of washed samples, all samples were prepared at a final β_2 concentration of 150 μM. All samples were incubated with their respective equivalent of manganese for at least 10 min. All incubations was done on ice and in open Eppendorf cups. Six sample series were prepared (Table 11). Washed samples were prepared in buffer where oxygen was removed via bubbling through nitrogen gas. They were washed in PD10 columns following the spin protocol as described by the manufacturer. Afterwards, amicons were used to increase the concentration to the final concentration. Finished samples were transferred into 2.9 mm quartz glass EPR tubes and frozen in liquid nitrogen. Enough sample was transferred to at least fill the entire active window of the QT2 resonator.

Table 11: β_2 samples that were used in this section. Samples from the same batch are grouped together. Time series were prepared by taking samples from the same reaction vessel, concentration series were prepared in parallel.

	Final β_2 conc. [μM]	Mn^{2+}	Fe^{2+}	Further steps/notes:	Produced by
Manganese and Iron					
1-Mn-5Fe:1min	150	1 eq. 10 min	5 eq. 1 min	/	Viktoria Gocke
1-Mn-5Fe:15min	150	1 eq. 10 min	5 eq. 15 min		
1-Mn-5Fe:1h	150	1 eq. 10 min	5 eq. 1 h		
1-Mn-5Fe:2h	150	1 eq. 10 min	5 eq. 2 h		
1-Mn-5Fe:wash	150	1 eq. 10 min	5 eq. 2 h	Washed, buffer deoxygenated	Shari Meichsner
2-Mn-5Fe:wash	100	2 eq. 10 min	5 eq. 2 h		
3-Mn-5Fe:wash	100	3 eq. 10 min	5 eq. 2 h		
Manganese					
1-Mn:org	150	1 eq. 10 min	/	/	Viktoria Gocke
2-Mn:org	150	2 eq. 10 min	/		
3-Mn:org	150	3 eq. 10 min	/		
1-Mn:rep	150	1 eq. 10 min	/	/	Viktoria Gocke
2-Mn:rep	150	2 eq. 10 min	/		
3-Mn:rep	150	3 eq. 10 min	/		
1-Mn:wash	100	1 eq. 2:10 h	/	Washed, buffer deoxygenated	Shari Meichsner
2-Mn:wash	150	2 eq. 2:10 h	/		
3-Mn:wash	150	3 eq. 2:10 h	/		
1-Mn:anaer	150	1 eq. 10 min	/	Produced in glovebox under anaerobic conditions	Viktoria Gocke
2-Mn:anaer	150	2 eq. 10 min	/		
3-Mn:anaer	150	3 eq. 10 min	/		

4.5.2. Measurement parameters

Table 12: Measurement parameters for pulsed ESE-detected field sweeps

Pulse sequence	$\pi/2$	- τ	- π	- τ	- Detect
Length [ns]	16	300	32	300	80
Shape[a]	(1)		(1)		
Amplitude	90%		90%		
Attenuation	See Chapter 5.1.1				
Sweep rate	75.36 G/s				
Shot repetition time	700 µs				
Temperature	10 K				
Frequency	34.003 GHz ± 0.2 MHz				

Table 13: Measurement parameters for Tyr-Tyr DEER with 16-step phasecycling
$(\pi/2 - \tau_1 - \pi - (\tau_1 + t) - p - (\tau_2 - t) - \pi - \tau_2 - \text{Detect})$

Pulse sequence	$\pi/2$	π	p	τ_1	τ_2	t	Detect
Length [ns]	30.1 ± 1.9	60.3 ± 3.7	30.3 ± 0.8	300	2100	-200:16:1976	44.3 ± 1.4
Shape[h]	(1)	(1)	(1)				
Amplitude	90%	90%	90%				
Frequency offset [MHz]			+84				
Shot repetition time	4080 µs						
Temperature	10 K						
Frequency	33.919 ± 0.000 GHz						
Field	1207.6 mT						

Table 14: Measurement parameters for Tyr-FeMn DEER with 16-step phasecycling
$(\pi/2 - \tau_1 - \pi - (\tau_1 + t) - p - (\tau_2 - t) - \pi - \tau_2 - \text{Detect})$

Pulse sequence	$\pi/2$	π	p	τ_1	τ_2	t	Detect
Length [ns]	16.6 ± 1.3	33.1 ± 2.5	95.0 ± 0.0	300	2100	-200:16:1880	44.6 ± 1.0
Shape[h]	(1)	(1)	(6)				
Amplitude	90%	90%	90%				
Frequency offset [MHz]			+80-320				
Shot repetition time	4080 µs						
Temperature	10 K						
Frequency	33.800 ± 0.000 GHz						
Field	1202.6 mT						

[a] Numbering system following Bruker standard, (1): Gaussian pulse, (6): Gaussian pulse with adjusted sweep frequency[139].

Table 15: Measurement parameters for Mn-Mn DEER with 16-step phasecycling
$\left(\pi/2 - \tau_1 - \pi - (\tau_1 + t) - p - (\tau_2 - t) - \pi - \tau_2 - \text{Detect}\right)$

Pulse sequence	$\pi/2$	π	p	τ_1	τ_2	t	Detect
Length [ns]	50.3 ± 2.9	50.3 ± 2.9	31.4 ± 2.5	300; 410	1590	-200:14:1452	44.6 ± 1.0
Shape[h]	(1)	(1)	(1)				
Amplitude	22.5%	45%	30%				
Frequency offset [MHz]			+90				
Shot repetition time	510 µs						
Temperature	10 K						
Frequency	33.913 ± 0.000 GHz						
Field	1202.6 mT						

Table 16: Measurement parameters for Tyr-Metal RIDME, with 8-step phasecycling
$\left(\pi/2 - \tau_1 - \pi - (\tau_1 + t) - \pi/2 - T_{\text{mix}} - \pi/2 - (\tau_2 - t) - \pi - \tau_2 - \text{Detect}\right)$

Pulse sequence	$\pi/2$	π	T_{mix}	τ_1	τ_2	t	Detect
Length [ns]	16	32	60 µs	300	1650	-50:10:1060	46 ± 5
Shape[h]	(1)	(1)					
Amplitude	90%	90%					
Frequency offset [MHz]							
Shot repetition time	1020 µs						
Temperature	30 K						
Frequency	34.01863 GHz						
Field	1210 mT						

5. Appendix

5.1. Normalizations and procedures for conversion between the XQ-band machine and the Q-band standalone

5.1.1. Power levels

While both spectrometers in principle use the same TWT amplifier and the Q-standalone on paper has double the power of the XQ-machine, in practice the actual effective power in pulse mode depends on too many factors to calculate with any reliability. Therefore, measurements were taken on both spectrometers with varying power to find the best fit between the two. As a result, the following conversion table was used.

Table 17: Power best estimate of equivalents between the XQ-machine and Q-standalone.

XQ-machine	Q-standalone
4 dB	5 dB
8 dB	10 dB
13 dB	14 dB
20 dB	20 dB

5.1.2. Fieldshifts

Any classical EPR magnet will experience an offset between the magnetic field at the sample and the one measured by the hall probe. For Bruker spectrometers this offset is corrected for by applying a linear field correction. However, as the field is swept and the magnet saturates at around 1 T, the slope of the offset inverts.[148] Therefore, it is not possible to measure a full sweep for broader systems at Q-Band without any field offset on a Bruker spectrometer. This issue can be remedied by squeezing the X-axis of the measurement. However, establishing such a correction would either require additional hardware to measure the field at the sample position or very exotic samples that give sharp peaks over such a large range. Since most species measured here either don't have any significant signal below 1 T or only very broad and featureless shoulders, we instead elected to use 2 distinct calibration sets for X- and Q-band frequency measurements on the XQ-band machine. For the Q-band frequency calibration we referenced copper measurements taken on our Q-band spectrometer. The Q-band spectrometer is taken as reference for consistency with past measurements and comparability. Should high precision *g*-value determination be of interest further calibrations should be performed.

Later measurements of manganese revealed a further offset between the XQ-band and Q-band spectrometers. This offset can partially be explained by different sweep rate-dependent offsets between the spectrometers. To correct for the offset the following procedure was applied:

Spectra of samples measured at both spectrometers at the respective equivalent powers were taken (Table 18).

Table 18: The samples and respective measurements used to build the measurement pairs Meas A-E used for fieldshift correction and signal factor determination between the Q-standalone and XQ-machine (Figure 45 & Figure 46).

	Sample	Q-standalone power	XQ-machine power
Meas A	150 μM β_2 + 2 eq Mn	14.0 dB	13.0 dB
Meas B	150 μM β_2 + 3 eq Mn + free Mn removal with PD10	5.0 dB	4.0 dB
Meas C	150 μM β_2 + 3 eq Mn + free Mn removal with PD10	10.0 dB	8.0 dB
Meas D	150 μM β_2 + 3 eq Mn + free Mn removal with PD10	14.0 dB	13.0 dB
Meas E	150 μM β_2 + 1 eq Mn + 5 eq Fe after wait time + free Mn removal with PD10	5.0 dB	4.0 dB

The maxima of the first and second derivatives were determined by hand for both measurements and fitted (Figure 45).

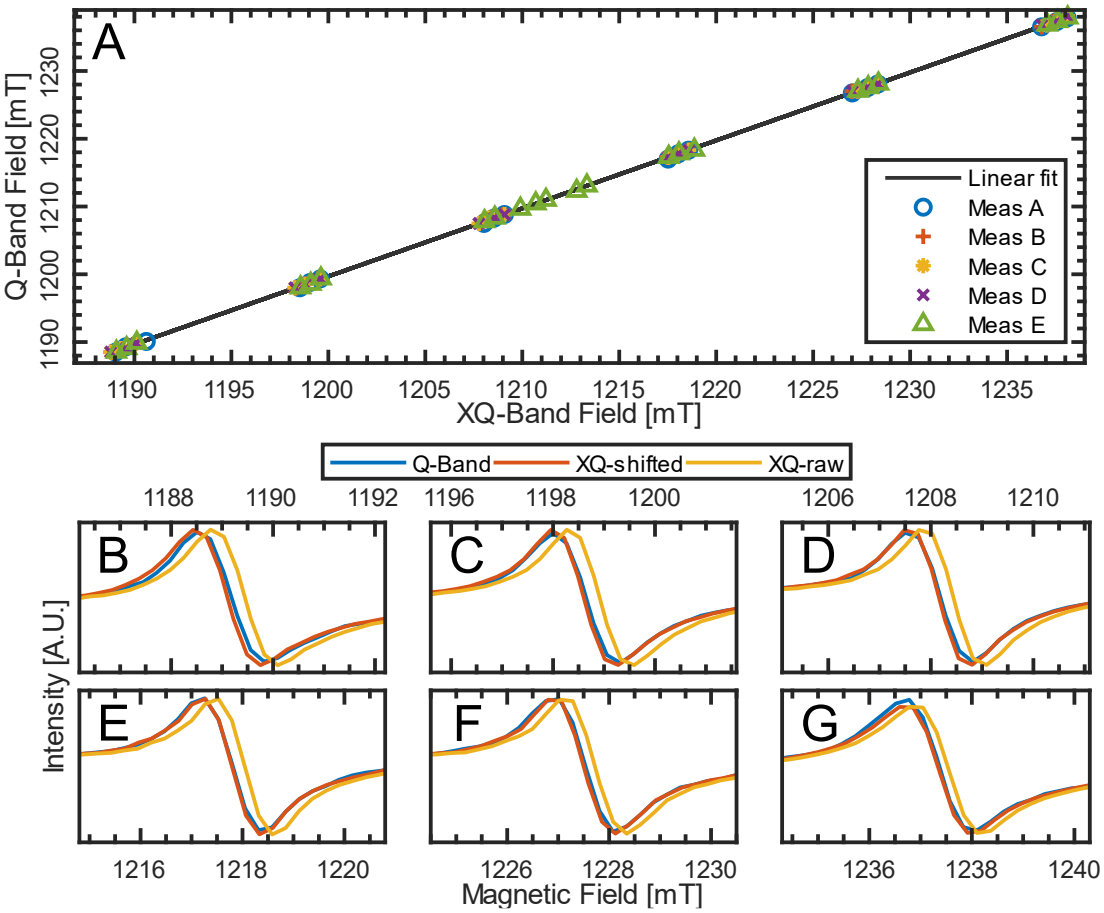

Figure 45: **A**: The first and second derivative peaks of the measurement pairs Meas A-E (Table 18) at the XQ-machine and Q-standalone are plotted against each other. A linear fit was reached for all points with 0.3134 µT/mT - 4.0703 mT. **B-G**: Exemplary zoom-in on the respective peaks of β_2 + 3 eq. Mn with and without the additional field correction applied to the XQ-Band data. The data is pseudo-modulated with a modulation amplitude of 1 mT.

On top of field-shifts due to the inhomogeneities in the magnetic fields, EPR spectrometers also experience field-shifts as the field of the magnet lags behind when the field is swept at higher sweep rates. While just reducing the sweep rate to the point where the offset disappears is possible, such low sweep rates are not practical for broad spectra, such as manganese, and make the measurement more susceptible to background instabilities. Therefore, all spectra relating to RNR were measured with a sweep rate of approximately 7.5 mT/s. To establish the offset caused by the sweep rate two spectra of 150 uM β_2 + 1 eq. Mn + 5 eq. Fe after 2 hours with the second spectrum being recorded at a sweep rate of 1.8 mT/s were compared following the same procedure as previously described. A shift of -0.126 µT/mT + 1.359 mT was determined.

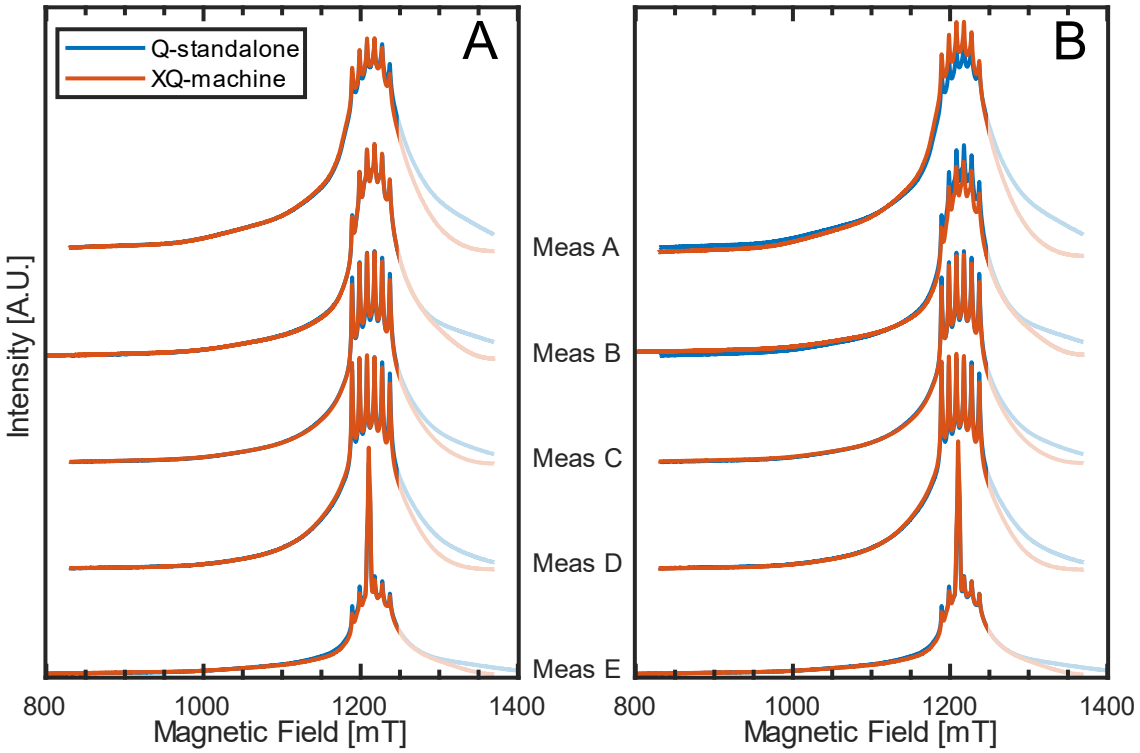

Figure 46: Scaling of signals between Q-standalone and XQ-machine. For each comparison the XQ spectra were shifted and scaled to give the best fit. Since the high field signal drops of much faster with the XQ machine data above 1248.4 mT was not included in the fit (desaturated in the plot). The measurement pairs A-E are the same used in Figure 45 and **A**: Spectra plotted with the best scaling factor for each comparison. **B**: Spectra plotted with the average scaling factor (88.46).

5.2. DEER with chirp pulses

5.2.1. QTII resonator

The QTII is a commercially available Q-EPR resonator produced by Bruker. Its characteristic features include a cavity with adjustable cavity length, and it can be overcoupled quite broadly. The adjustable cavity length allows for limited adjustment of the resonator frequency. This feature was utilised to ensure a constant frequency for DEER measurements, which was especially relevant for GQs since the signal intensity is quite sensitive to field and frequency. However, the QTII resonator has another interesting characteristic. It has two additional dips (Figure 47). By placing the detection sequence in the second dip during chirped DEER measurements, the detection sequence maintains a good signal to noise ratio despite being 200 MHz removed from the centre of the dip.

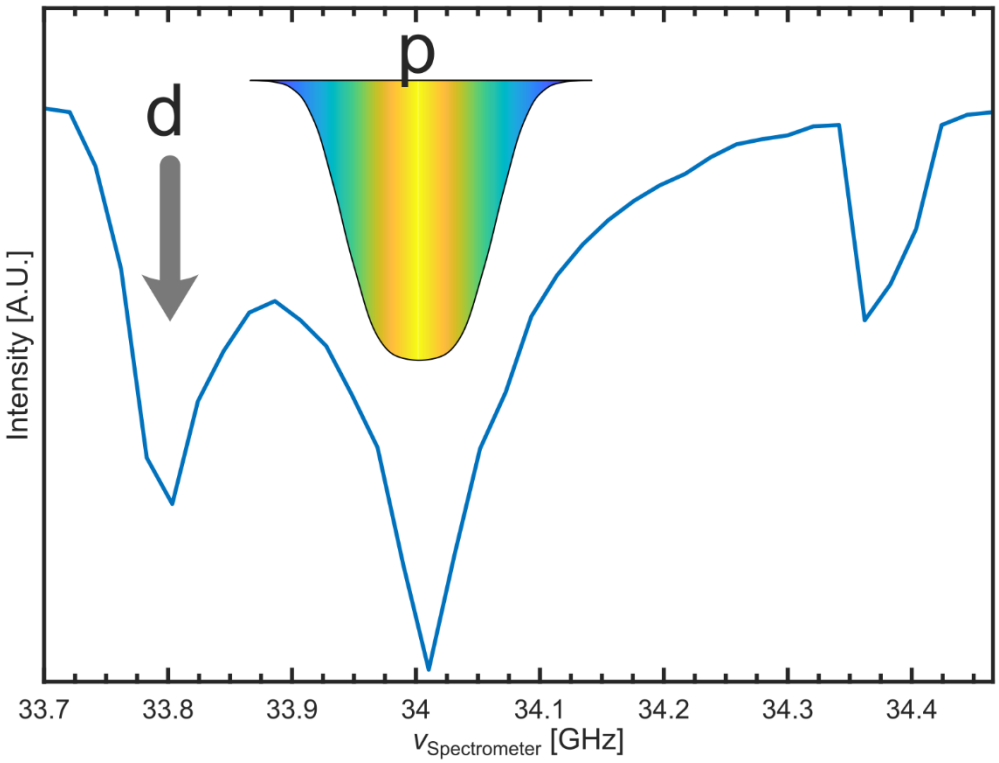

Figure 47: Resonator profile of overcoupled QTII resonator. The resonator profile was determined via field- and frequency-dependent microwave nutations with subsequent Fourier transformation to extract the main Rabi-frequency. The resonator consists of three dips, a primary dip at 34 GHz, a secondary dip at 33.8 GHz, and another dip at almost 34.4 GHz. The secondary dip can be used for DEER with chirped pump pulses, where the detection sequence is placed in the secondary dip and the chirped pump pulse fills the primary dip.

5.2.2. Pulse optimisation for Tyr-FeMn in β_2

While pulse length optimisation for monochromatic pulses is relatively straightforward with a microwave nutation experiment (Table 7) as the flip angle changes linearly with the pulse length:

$$\Phi = \gamma B_1 \sqrt{S(S+1) - m_s(m_s+1)} \cdot t_{\text{Pulse}}, \tag{33}$$

this is not the case for a chirped pulse where the critical adiabaticity Q_{crit}, determines the flip angle, with the maximum flip angle for any species being 180°.[137,142,143]

$$\Phi = \arccos\left(2 \cdot exp\left(-\frac{\pi}{2} Q_{crit}\right) - 1\right) \tag{34}$$

Instead, DEER with a variable length pump pulse was recorded. The maximum modulation amplitude was reached at a pulse length of 95 ns.

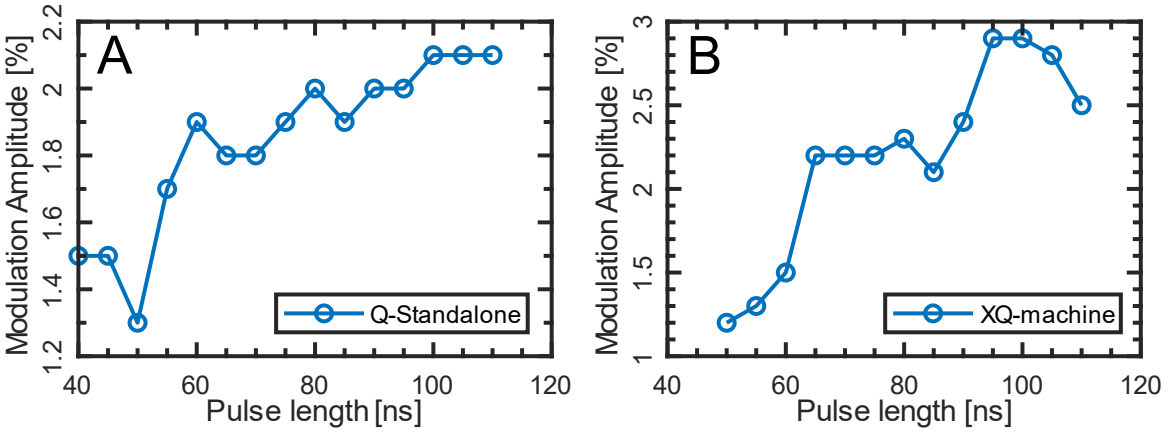

Figure 48: Modulation depth of the Q-Band standalone and X/Q-band machine.

5.3. Additional spectra

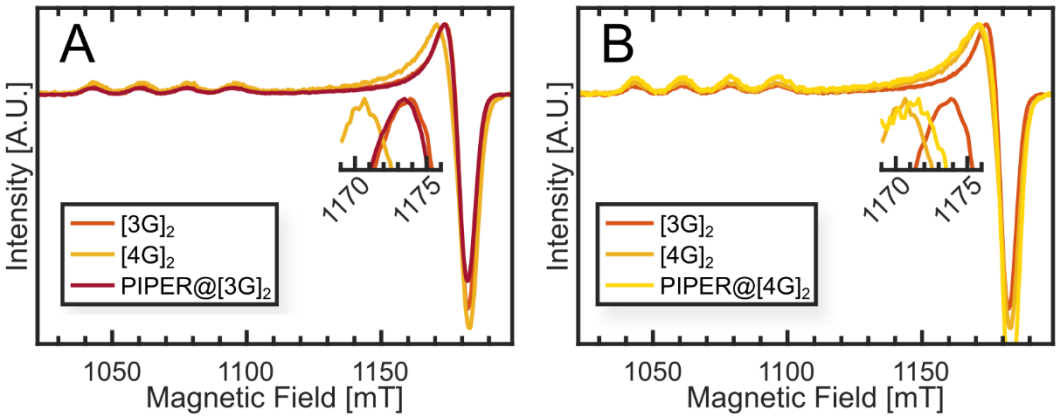

Figure 49: **A**: ESE detected field-sweeps of $[3G]_2$+PIPER after 4 hours, showing that the formation of PIPER@$[3G]_2$ does not influence the line shape. All spectra are pseudomodulated with a modulation amplitude of 3 mT. $[3G]_2$ and $[4G]_2$ are ploted for reference. **B**: ESE detected field-sweeps of PIPER@$[4G]_2$, showing that the formation of PIPER@$[4G]_2$ does not influence the line shape. All spectra are pseudomodulated with a modulation amplitude of 3 mT. $[3G]_2$ and $[4G]_2$ are ploted for reference.

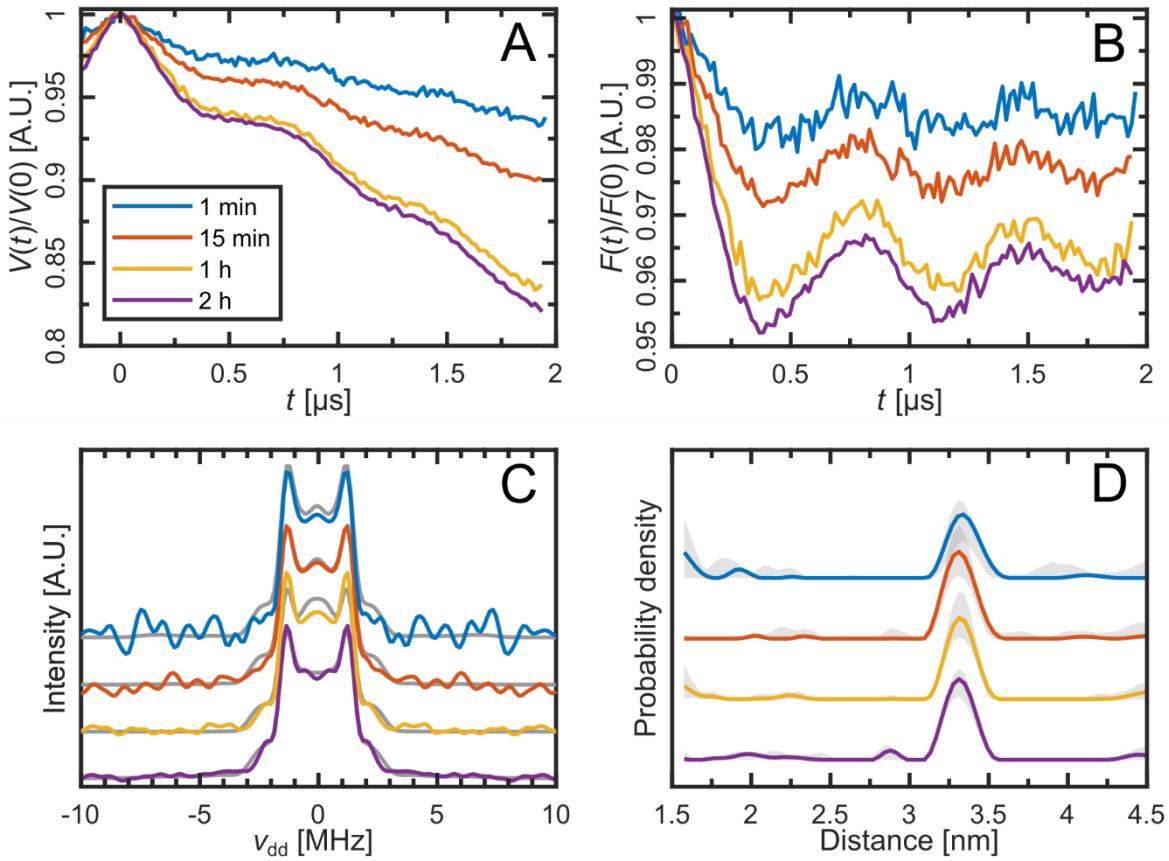

Figure 50: Tyr-Tyr DEER measurements on β_2 with 1 eq. Mn^{2+} added, followed by the addition of 5 eq. Fe^{2+}. Samples are taken at 1 min, 15 min, 1 h, and 2 h after the addition of Fe^{2+}. **A**: Raw DEER traces. **B**: Background corrected DEER traces. **C**: Dipolar spectra. The fits are included in gray. **D**: Results of distance analysis with uncertainty estimates.

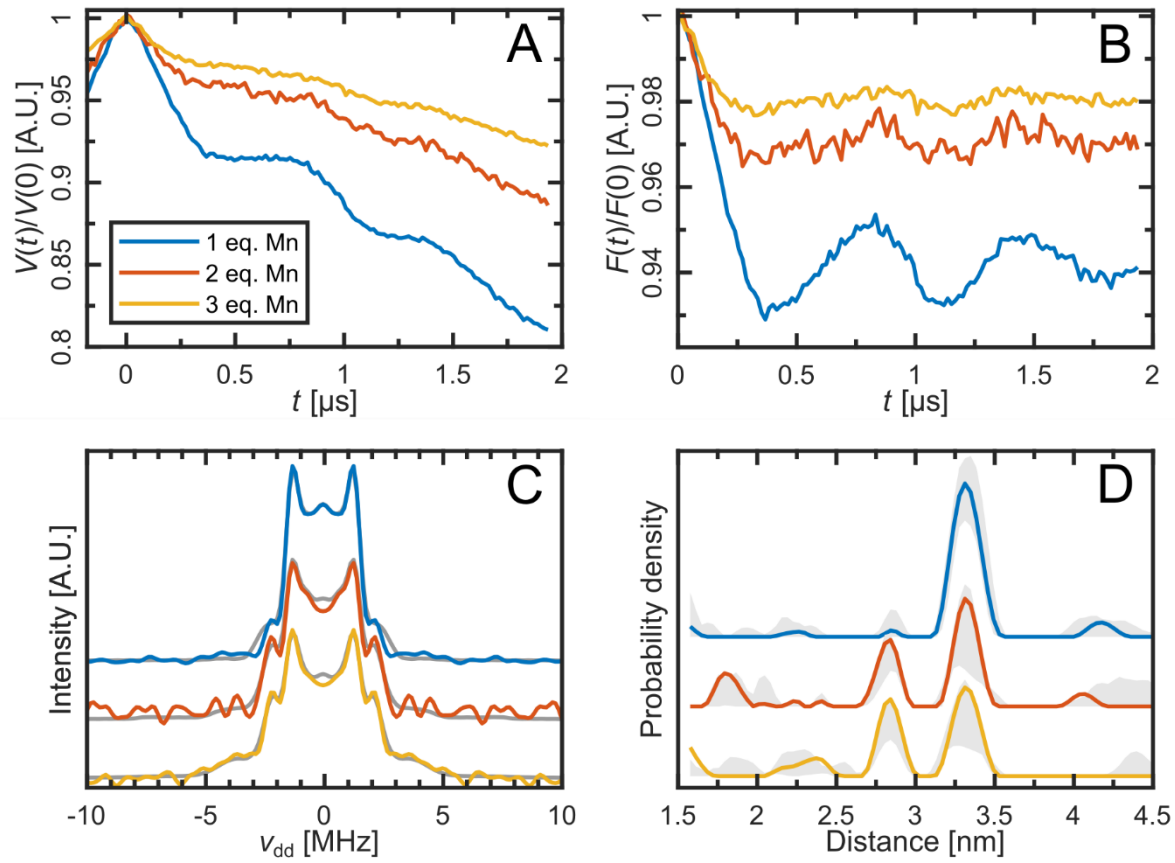

Figure 51: Tyr-Tyr DEER measurements on β_2 with 1, 2 & 3 eq. Mn^{2+} added, followed by the addition of 5 eq. Fe^{2+}. Samples were washed 2 h after the addition of Fe^{2+} and frozen in liquid nitrogen. **A**: Raw DEER traces. **B**: Background corrected DEER traces. **C**: Dipolar spectra. The fits are included in gray. **D**: Results of distance analysis with uncertainty estimates.

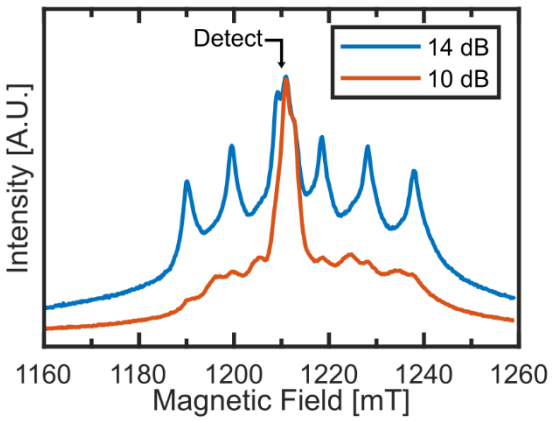

Figure 52: ESE-detected field-sweep of β_2 with 2 eq. Mn added, followed by the addition of 5 eq. Fe. Measurements were taken in a slightly overcoupled QTII resonator at 10 dB to highlight the Tyr*-signal and at 14 dB to highlight the Mn signal. The position at which RIDME was measured is indicated.

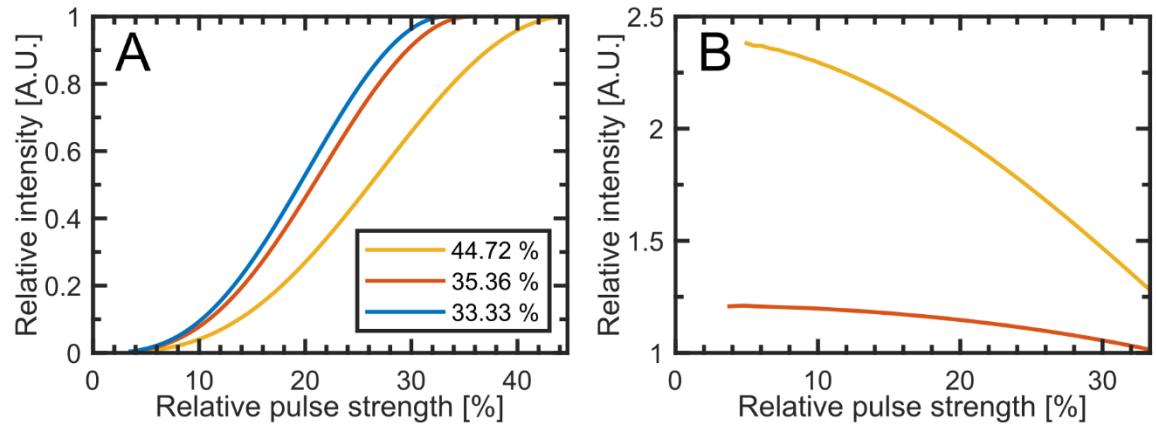

Figure 53: **A**: Relative intensities of an echo as a function of pulse strength (normalized to optimal pulse strength for *S*=1/2) for the respective optimal pulse strengths of the different transitions in manganese. **B**: Fraction of -1/2=>1/2 transition over the remaining transitions as a function of pulse strength.

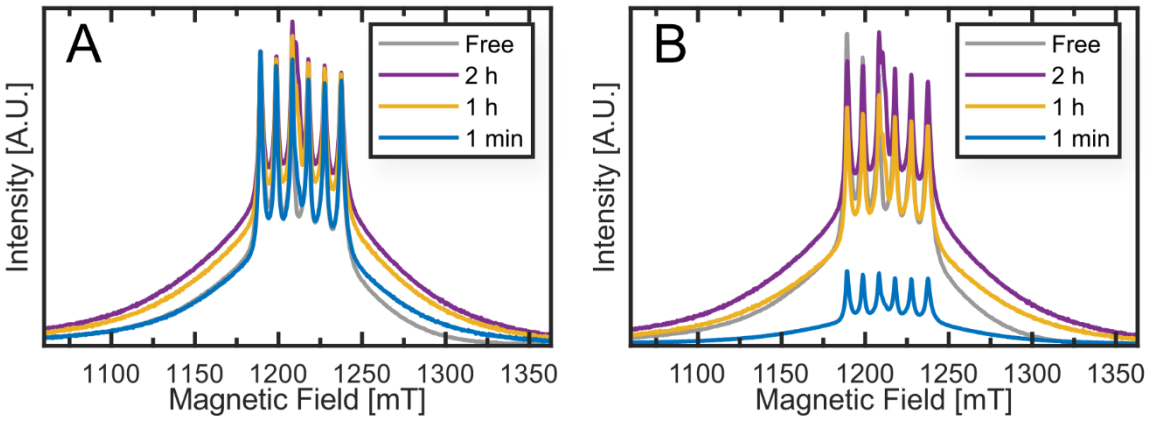

Figure 54: **A**: ESE detected field-sweeps of 1-Mn-5Fe:1min,15min,1h,2h, recorded at 20 dB and 10 K. All samples mostly display the narrow lines associated with free Mn^{2+}. Spectra are normalized to the height of the first peak. Additionally, a spectrum of free Mn^{2+} is plotted in grey for comparison. **B**: Same as (a) but only normalized to spectrometer parameters.

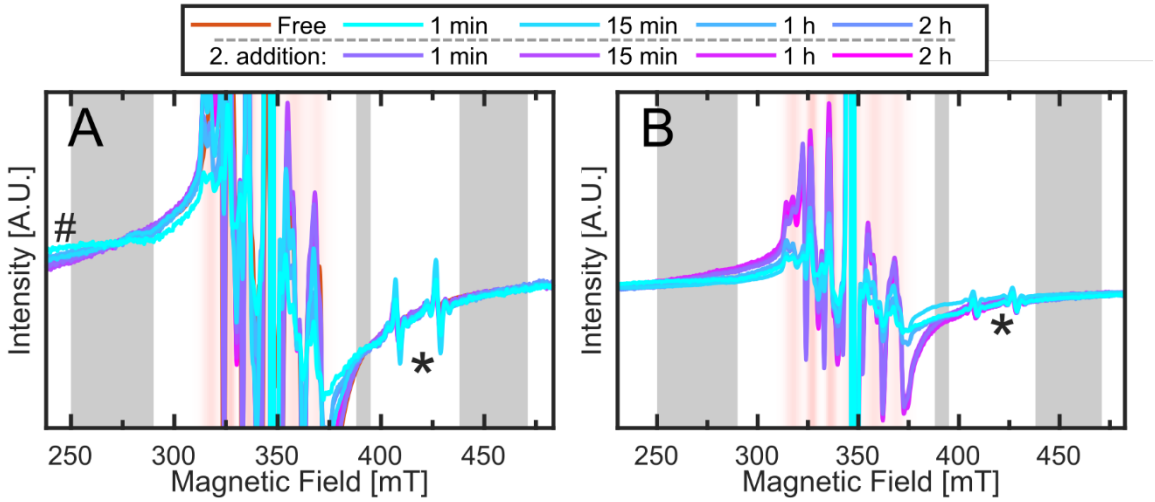

Figure 55: CW measurements of a time series repetition. Another 5 eq. of Fe^{2+} were added after the 2 h mark. The spectra were recorded in X-band at 15 K, with a modulation amplitude of 0.8 mT. Additionally, a sample of free Mn^{2+} in buffer is plotted. The spectra were scaled to maximize overlap in the grey regions. The red shaded regions indicate the area where the FeMn signal is found (shading intensity equals the intensity of the signal). An asterisk marks a background signal. The # marks the signal originating from mono-Mn at 1 min. The calculated amounts can be found in Table 19. The measurements were taken by Sergius Boschmann. **A**: spectra scaled for the shoulders to fit as in Figure 42a. **B**: Spectra only normalized for spectrometer parameters.

Table 19: Amount of free Mn^{2+} calculated for the repetition of the time series shown in Figure 55 scaled to the same scale as the first time series (Figure 42). The 1 min sample still contained some mono-Mn signal, skewing the calculated amounts.

Time	Free Mn^{2+}
1 min	(84%)
15 min	48%
1 h	84%
2 h	78%
2 h + 1 min	97%
2 h + 15 min	93%
2 h + 1 h	113%
2 h + 2 h	109%

5.4. RNR DEER

5.4.1. Alternative pulse length nutation

The normal microwave nutation $p(t) - \tau_1 - \frac{\pi}{2} - \tau_2 - \pi - \tau_2 - d$ sequence allows for the quick reading off of optimal pulse lengths for samples with a single species. [103,104] However, for mixtures of species and different spin states this no longer holds true. To circumvent this issue ESE-detected field sweeps with varying pulse lengths $(p\left(\frac{t}{2}\right) - \tau_1 - p(t) - \tau_1 - d)$ centered around the desired field position were recorded (Figure 56). Please note that this method is technically in no way an improvement; it is simply convenient to use and makes visualization of which part o the spektrum belongs to which species easier.

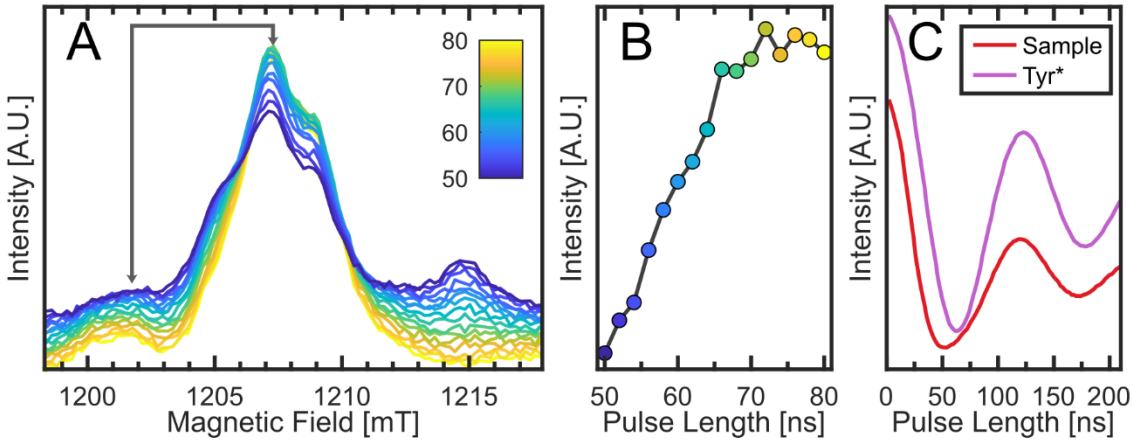

Figure 56: Determination of the optimal detect pulse length for the detection of the Tyr-radical in a sample with 1 eq. Mn^{2+} and 5 eq. Fe^{2+} added. **A**: ESE-detected field sweep with varying pulse length. Since the signal is the sum of both the manganese and Tyr* the difference between the peak and left shoulder is taken. **B**: The difference from A plotted against the pulse length. **C**: Comparison of a classic microwave nutation on the same sample and microwave nutation on a sample that only contains Tyr*, no Mn^{2+}.

5.4.2. Manganese artefact

Many Mn-Mn DEER traces showed an artefact at roughly $t = \tau_1$. The echos that different pathways created by a 4-puls DEER sequence could theoretically produce are known.[149] The only pathway that would create an echo at this position would involve the first π-pulse returning magnetization to the z-axis and the pump pulse flipping it back into the xy-plane, with the other pulses working normally. This pathway should be removed by 16-phase cycling, which was employed; however, phase cycling did not eliminate the artefact. As of this moment, no statement about the origin of the artifact can be given. However, the following procedure was implemented to successfully remove the artefact in postprocessing:

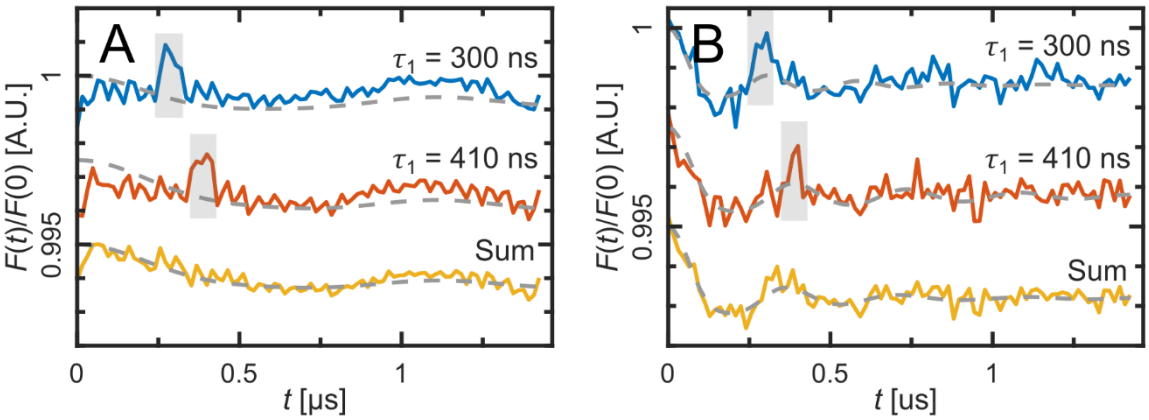

Figure 57: Background-corrected Mn-Mn DEER measurements. The artefact is highlighted with a grey box. The sum of both spectra is generated while excluding the shaded areas. **A**: 3 eq. manganese, sample prepared in glovebox. **B**: 3 eq. manganese added, followed by 5 eq. of iron.

To remove the artefact 2 traces with different τ_1 were recorded and summed up. The regions where the artefact is was identified and not included in the sum instead including the other spectrum twice (Figure 57).

5.4.3. Manganese ruler

The ruler was provided by Godt lab at Bielefeld University. DEER measurements were performed as established for RNR Mn-Mn measurements. A distance of 2.6 nm at a modulation depth of 1.9% was reached. Both results are identical to what previous W-band studies found.[150] For many DEER samples the modulation depth increases at lower frequency bands due to the spectrum being less broad, allowing for easier inversion of larger portion of the spectrum. However, with manganese, the spectrum is dominated by hyperfine and zero-field splitting, resulting in relatively minor changes in spectral width.

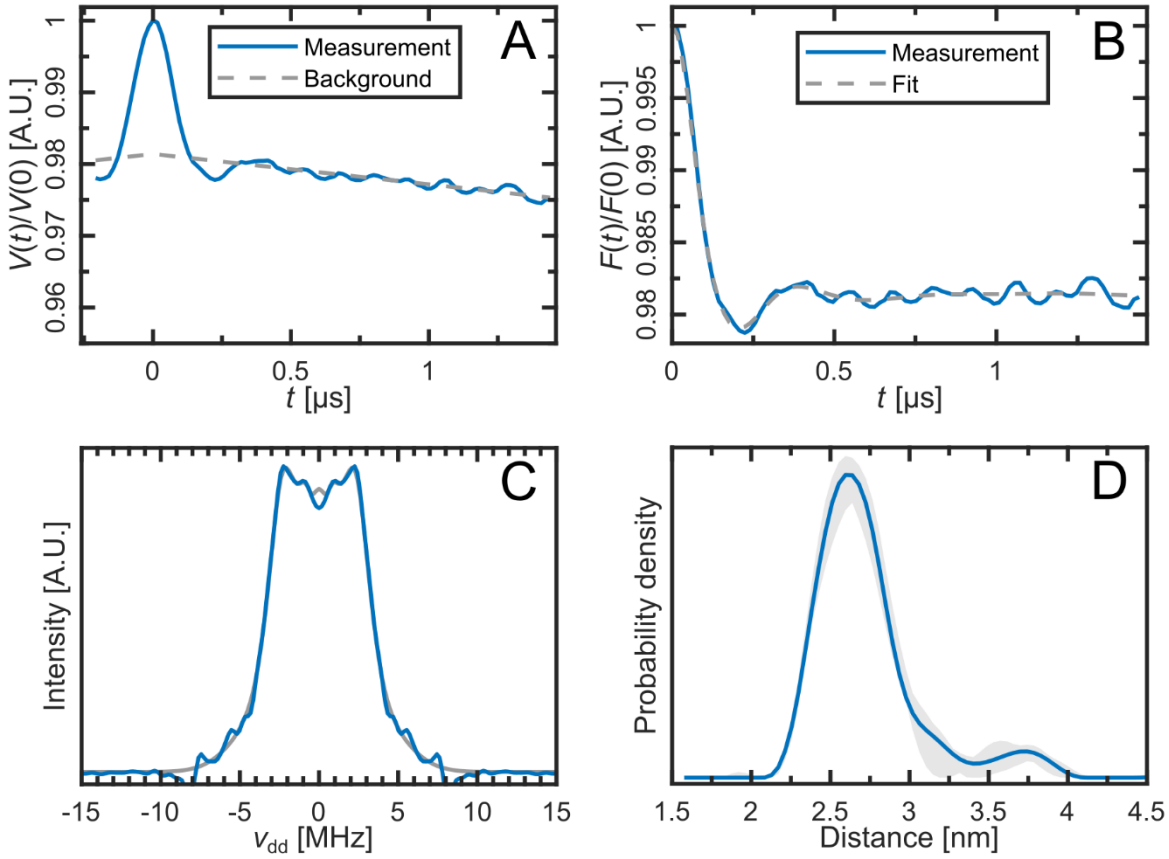

Figure 58: Mn-Mn DEER measurements on 100 µM $MnDOTA_2OPE$ in 50% (v/v) D_2O, glycerol-d8. **A**: Raw DEER trace with background fit. **B**: Background corrected DEER trace with fit from the distance analysis. **C**: Dipolar spectrum. The fits are included in gray. **D**: Result of the distance analysis with uncertainty estimates.

To confirm the binding of manganese to the ruler, the T_2 relaxation time of the ruler was determined and compared to the relaxation time of free manganese in the same solvent (Figure 59b)

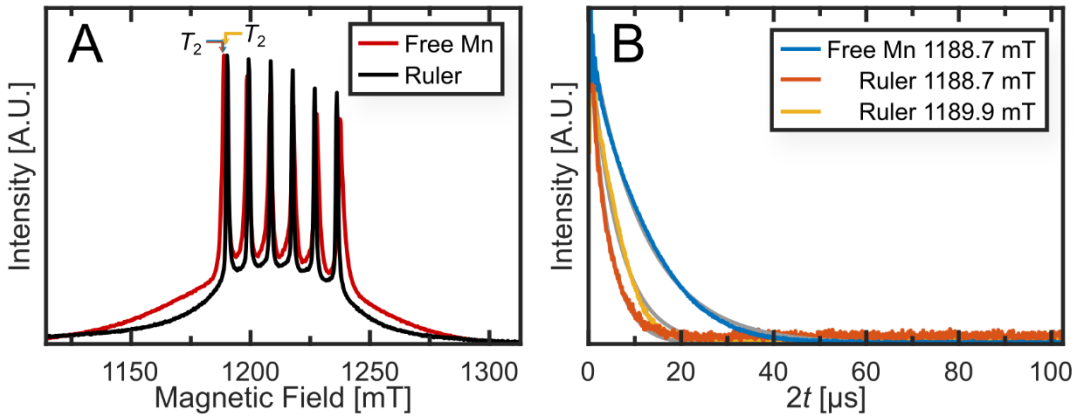

Figure 59: **A**: ESE-detected fieldsweep of free manganese and the $MnDOTA_2OPE$ ruler with the field positions used for T_2 measurements indicated. **B**: T_2 measurements.

The T_2 of the ruler is noticeably lower than that of free manganese (12 vs 4-6 µs). Furthermore, free manganese displays a larger hyperfine splitting. Therefore, if there was any significant amount of free manganese in the ruler, it should be visible in the fieldsweep. While neither is enough to quantify the amount of free manganese, it can rule out any significant amount of unbound manganese. To ensure comparability between the modulation depths, the fraction of A-spins that have a B-spin at the pump position (looking at A/B-spin pairs only) should be similar. Manganese displays virtually no orientation selection. Therefore, any single spin has an equal chance of being the B-spin to any specific A-spin and the fraction only depends on the which fraction of total spins is located at the pump position. In comparison, the spectral density of the manganese ruler is larger at the pump position than β_2-bound manganese (Table 20).

Table 20: Spectral fractions of the pump pulse of the 1 eq. Mn unwashed repetition, 3 eq. Mn unwashed repetition and manganese ruler sample for different microwave powers. The spectral fraction was calculated as the integral of the product of the inversion efficiency of the pump pulse and the spectral intensity divided by the integral of the total spectrum. The inversion efficiency was calculated using the inversion profile generated by the EasySpin function exciteprofile, with maximum inversion corresponding to a value of 1 and no inversion corresponding 0. The pulse was simulated with a length of 32 ns since this represents the average pump pulse length. However, changing the pulse length to 28 ns (shortest used pulse length) or 38 ns (longest used pulse length) does not change the relative values of the spectral fractions.

	1 eq.	3 eq.	Ruler
20 dB	1.30%	1.41%	1.67%
13 dB	1.28%	1.41%	1.70%
8 dB	1.33%	1.46%	1.78%
4 dB	1.46%	1.74%	2.03%

Therefore, the measured modulation depths of 1.7-1.1% for 1 eq. manganese are a strong indicator for a significant portion of bound manganese being bound with manganese in an opposing β-subunit.

5.5. Guanine quadruplex

5.5.1. Guanine quadruplex RIDME dimerization approximation

Two samples of $[3G]_2$ and $[4G]_2$ (125 μM) respectively, were prepared at 4 °C. RIDME and T_1 were measured at 30 K at 1043, 1177.4 & 1184 mT (Figure 60). The inversion efficiency in RIDME depends on the number of spin pairs where the B-spin experiences an odd number of spin flips P_{odd} during the mixing block.[151–153]

$$\lambda_{\mathrm{RIDME}} = P_{\mathrm{odd}} = {}^1/_2\left(1 - \exp\left(-\frac{T_{mix}}{T_1}\right)\right) \tag{35}$$

In approximation λ_{RIDME} and P_{odd} are the same. However, in practice, flip-flops, where flipping of the B-spin causes flipping of the A-spin and T_1 relaxation of the A-spin during the mixing block reduce the actual inversion efficiency. T_1 displays some field dependence for the GQs (Figure 60). Since the orientations of the A and B-spins in GQs are closely aligned, one would expect that $T_{1,\text{B-spin}}$ roughly equals $T_{1,\text{A-spin}}$. We therefore compare the modulation depths measured for each field position with the predicted inversion efficiency based on the T_1 measured for the same field position. However, the calculated fraction of dimer increases with the field for both $[3G]_2$ and $[4G]_2$ (Table 21). The two most likely reasons are either our assumption that $T_{1,\text{B-spin}} \approx T_{1,\text{A-spin}}$ is wrong or that A-B-spin flip flops are field dependent. There does not seem to be a correlation between measured modulation depth and field position with $[3G]_2$ having the highest modulation depth at 1177.4 mT while $[4G]_2$ has the lowest modulation depth at this position. Overall $[4G]_2$ gives lower dimer fractions than $[3G]_2$, which is consistent with the change in dimer ratios observed in monomer exchange experiments Chapter 3.1.2. $[4G]_2$ also displays a much lower variation in calculated dimer fractions compared to $[3G]_2$. Although not necessarily related this might be indicative of A-B flips being the culprit for the reduced modulation depth.

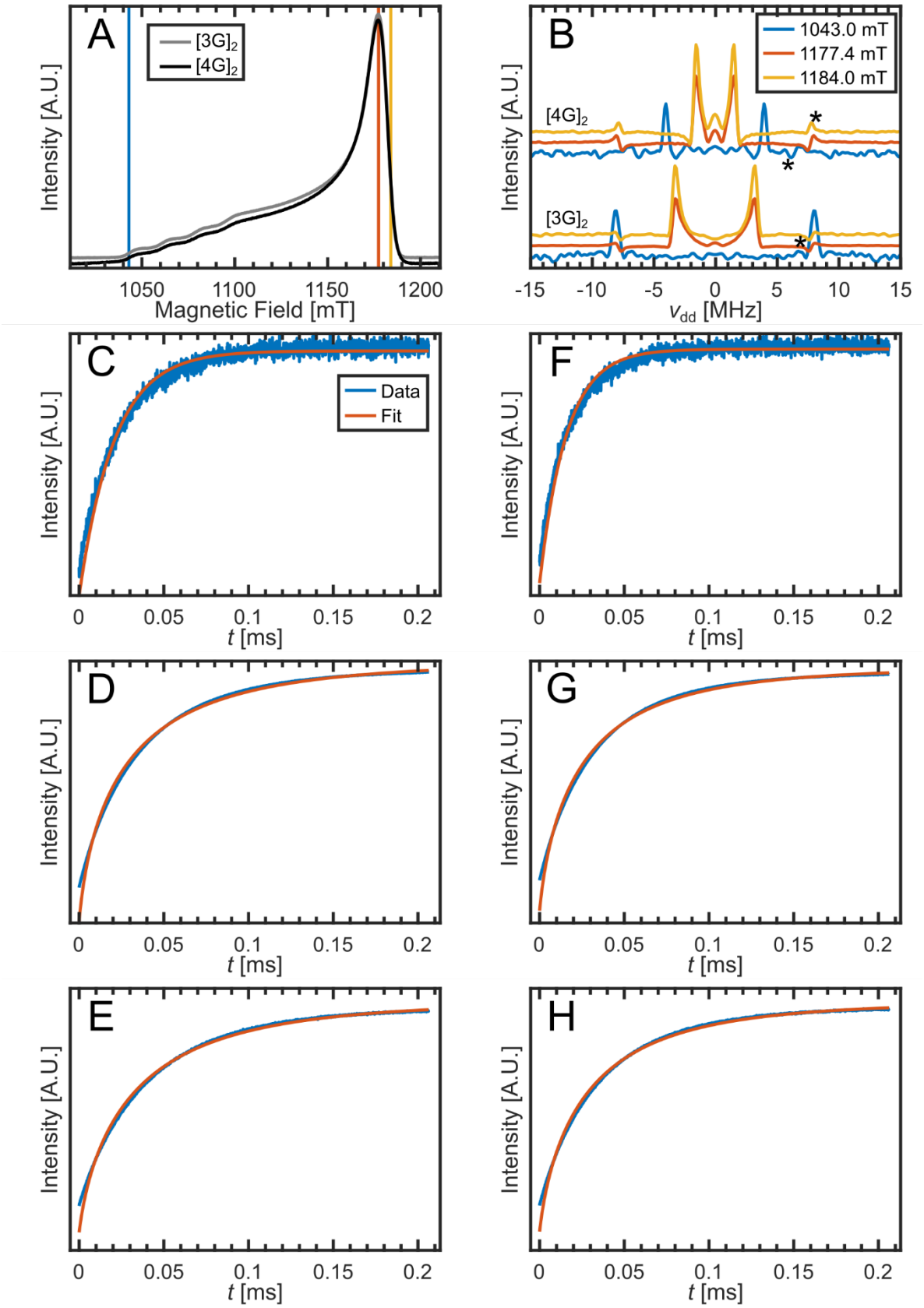

Figure 60: **A**: ESE-detected field sweeps of $[3G]_2$ and $[4G]_2$. **B**: Dipolar spectra from RIDME measurements on $[3G]_2$ (lower spectra) and $[4G]_2$ (upper spectra). ESEEM artefacts are marked with an asterisk. **C**-**E**: T_1 measurements of $[3G]_2$ at 1043, 1177.4 and 1184 mT and their fits. Fitting parameters are shown in Table 21. **F**-**H**: T_1 measurements of $[4G]_2$ at 1043, 1177.4 and 1184 mT and their fits. Fitting parameters are shown in Table 5.

Table 21: T_1 relaxation rates, measured RIDME modulation depths, calculated fraction of flipped B-spins, and based on those calculated, fraction of dimers for $[3G]_2$ and $[4G]_2$ measured at 30 K at different field positions.

		$[3G]_2$	$[4G]_2$		$[3G]_2$	$[4G]_2$		$[3G]_2$	$[4G]_2$
1043.0 mT	T_1 [µs]	20.71	15.78	P_{odd} [%]	25.76	30.67	Dimer fraction	43.47%	43.04%
	Stretch factor	1.00	1.00	Δ [%]	11.20	13.20			
1177.4 mT	T_1 [µs]	25.64	23.93	P_{odd} [%]	22.14	23.28	Dimer fraction	72.70%	48.96%
	Stretch factor	0.62	0.65	Δ [%]	16.10	11.40			
1184.0 mT	T_1 [µs]	31.15	27.04	P_{odd} [%]	19.11	21.29	Dimer fraction	70.65%	56.36%
	Stretch factor	0.67	0.67	Δ [%]	13.50	12.00			

Since equation (*35*) does not take the stretch factor β into account a second set of calculations based on the weighted sum over the T_1-distribution was calculated. The distribution was calculated based on:

$$P(T_1,\beta) = \frac{1}{\pi}\int_0^{\infty} \exp\left(-u^{\beta}\, cos\left(\frac{\pi\beta}{2}\right)\right)\cos\left(\frac{T_1^*}{T_1}u - u^{\beta}\sin\left(\frac{\pi\beta}{2}\right)\right)\mathrm{d}u \tag{36}$$

Here T_1^* is the relaxation time as defined in $I(t) = I_0\left(1 - 2\cdot\exp\left(-\left(t\cdot {T_1^*}^{-1}\right)^{\beta}\right)\right)$. The integral was evaluated numerically up to a value of u where $\exp\left(-u^{\beta}\, cos\left(\frac{\pi\beta}{2}\right)\right) \leq 10^{-5}$ with a stepsize of $\Delta u = \left|\left(20\pi\cdot\left(\frac{T_1^*}{T_1} - {u_{\max}}^{\beta-1}\sin\left(\frac{\pi\beta}{2}\right)\right)\right)^{-1}\right|$ to ensure that the stepsize was significantly smaller than the frequency of the cos term. These values allowed the faithful representation of different β for which analytic solutions are known. [108]

500 T_1-values from $10^{-5} < \frac{T_1^*}{T_1} < 2$ were sampled. However, taking the distribution into account at most caused a 2% change in the calculated fraction of dimers.

5.5.2. Guanine quadruplex chirp DEER

Chirped pump pulse DEER was recorded at 1043.6, 1150, 1182 mT for the 4 °C samples from section 3.2.2.

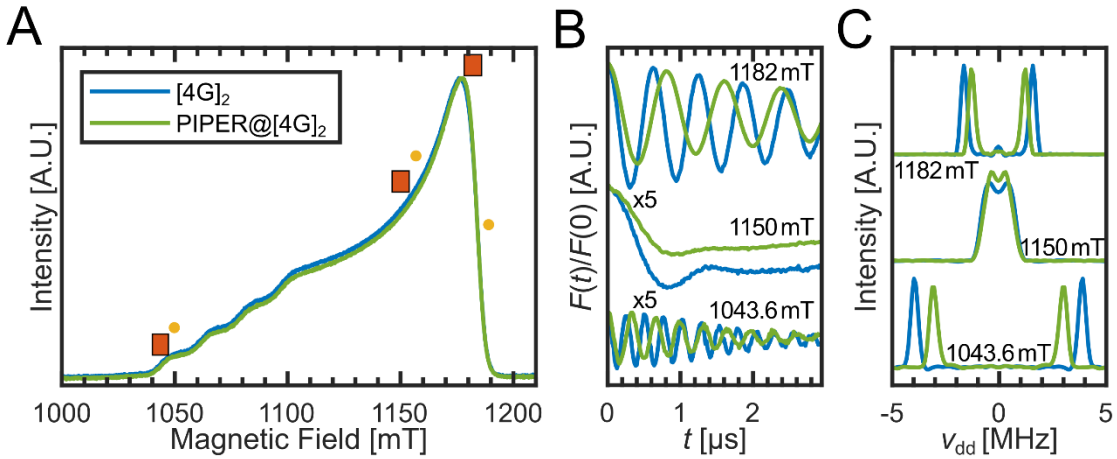

Figure 61: Field-dependent chirped pump pulse DEER measurements on $[4G]_2$ (blue) and PIPER@$[4G]_2$ (green). **A**: ESE-detected fieldsweeps of $[4G]_2$ and PIPER@$[4G]_2$ with the detect (yellow) and pump (orange) positions marked. The width of the pump window is estimated using the easyspin function exciteprofile. **B**: The DEER traces for each field position. The traces for 1150 mT and 1043.6 mT were scaled up by a factor of 5 for visibility reasons.

The modulation depth is higher for $[4G]_2$ at all field positions except for 1043.6 mT. Sitting at the very low field end of the spectrum, here PIPER@$[4G]_2$ has an only slightly lower modulation depth. It should, however be noted that while it only plays a minor role in our DEER due to its faster relaxation, there is a free copper fraction (1.5 Cu : 1 GQ). The free copper signal is noticeable as a broader shoulder in the low field, leading to free copper having a greater impact there compared to the high-field end. Therefore, it plays a larger influence in the modulation depth at the low field and might mask smaller differences in modulation depths between samples.

Table 22: The modulation depths of the measurements shown in Figure 61 for each field position. Additionally, the measurement at 1182 mT for monochromatic pump pulses (Figure 27) is listed for reference.

	$[4G]_2$	PIPER@$[4G]_2$
1043.6 mT	1.6%	1.5%
1150.0 mT	4.7%	3.4%
1182.0 mT	18.1%	14.8%
1182.0 mT*	7.9%	6.2%

*monochromatic pulse

Abbreviations

ADP	Adenosine diphosphate
ATP	Adenosine triphosphate
α_2	Class I RNR large subunit
β_2	Class I RNR small subunit
C•	Cystein radical
CDP	Cytosine diphosphate
CTP	Cytosine triphosphate
CW	Continuous wave (spectroscopy)
DEER	Double electron electron resonance spectroscopy
DNA	Deoxyribonucleic acid
E. coli	*Escherichia coli*
EPR	Electron paramagnetic resonance
ESE	Electron spin echo
FID	Free induction decay
G	Guanine
GDP	Guanosine diphosphate
GQ	Guanine quadruplex
GTP	Guanosine triphosphate
NMR	Nuclear magnetic resonance
PELDOR	Pulsed Electron Electron Double Resonance (see DEER)
Q-band	Frequency band around 34 GHz
Q-standalone	Elexsys E580 Q-Band standalone spectrometer with integrated SpinJet AWG equipped with a 150 W TWT amplifier, Oxford Instruments CF935 continuous-flow helium cryostat, and Oxford Instruments MercuryiTC temperature controller
QTII	Pulse Q-Band resonator produced by Bruker. Please note that the QTII is also referred to as the QT2, QT-II, 5106QT-2, and any other combination by Bruker
RIDME	Relaxation-Induced Dipolar Modulation Enhancement
RNA	Ribonucleic acid
RNR	Ribonucleotide reductase
T	Thymin
T_1-relaxation	Spin–lattice relaxation
T_2-relaxation	Spin–spin relaxation time

T_m-relaxation	Phase memory time
UDP	Uridine diphosphate
UTP	Uridine triphosphate
X-band	Frequency band around 9.6 GHz
XQ-machine	Bruker Elexsys E580 spectrometer equipped with a 150 W TWT amplifier, Bruker ER 5106QT-2 resonator, Bruker SpinJet AWG, Oxford Instruments CF935 continuous-flow helium cryostat and Oxford Instruments MercuryiTC temperature controller
Y•	Tyrosine radical
zfs	Zero field splitting

List of figures

*Figure 1: E. Coli RNR. **A**: Reduction of NDP/NTP to dNDP/dNTP. **B**: Cryo-electron microscopy structure of $\alpha_2\beta_2$ complex (6W4X).[55] **C**: Formation of β_2 metal cofactor.* 13
Figure 2: Illustration of different potential ways four Mn^{2+} could bind to three β_2-subunits. CW-spectroscopy only allows for the differentiation of A/B vs C/D, but not A vs B or C vs D. 14
*Figure 3: **A**: Schematic representation of a telomer with GQs in the telomeric region, and zoom in showing the binding mode of the guanine tetrad with Hoogsteen-base pairing. **B**: Exemplary oligonucleotide and its assembly into a tetramolecular GQ with copper label. **C**: Dimerization of GQs, with the distance between the Cu^{2+} measured in EPR indicated.* 15
Figure 4: Illustration of Zeeman splitting as a function of magnetic field with common spectrometer frequencies for a free electron marked on the top. 17
Figure 5: Schematic representation of field modulation in CW EPR, with the orange signal representing the field modulation and the yellow signal representing the generated signal. The insert shows how multiple time points in the field modulation correspond to time points in the signal modulation. 20
*Figure 6: **A**: Larmor precession of magnetic moment in static external magnetic field $B0$. **B**: Same picture but in rotating frame. The magnetization is static and the external magnetic field $B0Rot.\ frameB0' = 0$ vanishes.[102] **C**: Spin in rotating frame. **D**: Application of microwave pulse. The spin starts to rotate around the phase direction of the pulse counterclockwise at the Rabi frequency.* 21
*Figure 7: **A**-**E**: FID (free induction decay) following $\pi/2$-pulse flipping the magnetization onto the xy-plane. The dark purple spin package $\omega Larmor$ matches the spectrometer frequency. The brighter the spin package is colored, the larger the offset from the spectrometer frequency. As the spin packages evolve the **F**: The resulting magnetization along the Y-axis as the spin packets dephase. The bold, continuous line represents the bulk magnetization. The dashed lines represent the magnetization of different isolated spin packages.* 22
Figure 8: Different stages of a Hahn-echo signal detection. Pulse sequence on top, magnetization in rotating frame at the bottom. The pulses are -x pulses. Alternatively, to using a π-x the use of a π-y is shown in the bottom row. 23
Figure 9: Schematic Tm and $T1$ measurements on the left and exemplary resulting signals on the right. 24
Figure 10: 4-pulse DEER / 5-pulse RIDME. The top row displays the detection sequence forming a refocused Hahn-echo. The second and third rows show the B-spin inversion events for DEER and RIDME, respectively. The DEER inversion event is a π-pulse acting at a second frequency, referred to as the pump pulse. For RIDME the A-spin is flipped out of the xy-plane by a $\pi/2$ effectively storing it as a gradient along the z-axis before flipping it back onto the xy-plane after the mixing time $Tmix$. The B-spin is flipped by $T1$ relaxation processes. 25
Figure 11: Angle θ between the interspin vector r and external magnetic field B. 28

Figure 12: Exemplary Pake pattern with the dipolar frequency normalized to the dipolar frequency at $\theta = 90°$ Ddd. The black line describes a Pake pattern in the case of no orientation selection as a result of summing over all orientations (indicated by the colored lines). Since DEER is not sign-sensitive, the resulting spectra is the sum of itself and its mirror image. The dashed lines indicate the shape expected with sign-sensitive detection. The dipolar frequencies for $\theta = 90°$ $\perp$ and $\theta = 0°$ $\parallel$ are indicated. _____ *28*
Figure 13: Schematic examples of orientation selection in DEER. The hypothetical system has $g = [1, 2, 3]$. Each subplot shows a the A- and B-spin as balls with the effective g-value for each orientation colored in (1=blue, 3=yellow) and the interspin vector. The field positions where the respective spins are found in the spectrum are indicated. The field sweep was simulated with the easyspin function pepper at 9 GHz and colored in according to their g-value. ***A*****-*****C****: Interspin vector [0 0 r] rotated by the euler angles: [0, 90, 0]° (zxz-rotation). The B-spin is rotated by [35.26, 120.00, 54.74]°.* ***D*****-*****F****: Here, the interspin vector is rotated by [0, 30, -90]° B-spin is rotated by [0, 120, 0]°.*_____ *29*
Figure 14: Example of background corrected DEER spectrum with the modulation depth Δ marked. *31*
Figure 15: Orientation selection in DEER. ***A1****: An example system with two identical spins and g-anisotropy $gx, y, z = 1,2,3$ (1=blue, 3=yellow). For the sake of the example, both spins are completely rigid and the spectrometer can generate perfect pulses that flip each spin in its bandwidth perfectly.* ***B1****: Selection of the A-spin based on the detection sequence. The spins not selected are greyed out.* ***B2****: The resulting signal from just the A-spin selection which determines the signal intensity at $t = 0$.* ***C1****: Selection of the B-spin based on the pump pulse. The spins not selected are greyed out.* ***C2.1-C2.2****: The A-spins from (B) separated into the fraction with pumped B-spins $A : A \in Ad\ and\ B \in Bp$ and the fraction that does not have a pumped B-spin $A : A \in Ad\ and\ B \notin Bp$.* ***D1****: Spin pairs that comprise the modulated part of the signal $ABmod = AB : A \in Ad\ and\ B \in Bp$ as a result of the combined selection The amount the respective g-values are greyed out reflects the fraction of their spin pairs that contribute to the modulated part of the DEER trace.* ***D2****: The DEER signal that results from the sum of the modulated and unmodulated part of the DEER trace.*_____ *32*
Figure 16: Overview of structural analysis of GQ dimers with EPR. ***A****: ESE-detected fieldsweep of GQ with pump and detect positions for DEER marked. Furthermore, the parallel $\parallel$ and perpendicular $\perp$ position orientations are marked.* ***B****: Background corrected DEER traces.* ***C****: Overview of the potential angles between the copper labels. The spheres are coloured in based on the g-value in each respective direction.* ***D****: Schematic representation of the geometry of stacked GQ based on the angles found in previous DEER measurements.[29]* _____ *36*
Figure 17: DEER optimization for quantitative measurements on GQs. A&B: Field-dependent g-value selection. ***A****: ESE-detected field-sweep with the hyperfine splitting indicated by gray dashed lines. Furthermore, different field positions are marked by colored rectangles. The g-value distributions for these positions are shown in B.* ***B****: The distribution of g-values at the respective field positions (1040, 1088, 1150, 1177, 1182 mT) shown in A (same color). The g-values were calculated by doing orientation-selective simulations with pepper to calculate the intensity of each orientation at each field position. Then, the g-value for each orientation was calculated, and the orientation-dependent intensities were added up based on which g-value they correspond to. C-D: Field-dependent DEER optimization of a $[3G]_2$ and $[4G]_2$ mixture.* ***C****: The signal separation between the dipolar signal of $[3G]_2$ $[4G]_2$. The signals were fit as Gaussians, and the overlap area, normalized to the maximum overlap, was plotted on an inverted y-axis.* ***D****: The total signal intensity of the $[3G]_2$ and $[4G]_2$ dipolar signals.* ***E****: ESE-signal intensity at each field position, normalized to the maximum signal intensity.* _____ *38*
Figure 18: ESE detected field-sweeps of $[3G]_2$, $[4G]_2$, [3G][4G]-mixtures and mixtures with $[3G_{nd}]$. All spectra are pseudomodulated with a modulation amplitude of 3 mT. ***A****: Comparison of pure $[3G]_2$, $[4G]_2$ and a mixture of $[3G]_2$ and $[4G]_2$ (sample taken immediately after mixing).* ***B****: Comparison of $[3G]_2$ with a 1:1 mixture of $[3G]_2$ and $[3G_{nd}]$. $[4G]_2$ is additionally shown as reference.* ***C****: Comparison of a 1:1 mixture of $[3G]_2$ and $[4G]_2$ after 1 min and after 40 hours, where significant amounts of [3G][4G] have formed. $[3G]_2$ and $[4G]_2$ are additionally shown as reference.*_____ *39*
Figure 19: Stability measurements on $[3G]_2$ and $[4G]_2$ mixed with $[3G_{nd}]$. Samples were incubated at 12 °C for 1 min (blue), 20 h (orange) and 40 h (yellow). ***A****&****E****: DEER traces of the $[3G]_2$ and $[4G]_2$ mixtures, respectively.* ***B****&****F****: The associated modulation depths.* ***C****&****G****: ESE-detected field sweeps of the respective samples, normalized to spectrometer parameters only.* ***D****&****H****: Integral of the total signal intensity of the field sweep. The intensities were normalized to the largest intensity between all samples.* _____ *40*

*Figure 20: **A**: Modulation amplitude of $[3G]_2$+$[4G]_2$ sample plotted against the ESE-intensity. The markers are colored in based on the field position of the DEER experiment. **B**: Intensity of the $[3G]_2$ and $[4G]_2$ dipolar signal plotted against the ESE-intensity of a pure $[3G]_2$ and $[4G]_2$, respectively. The markers are colored in based on the field position of the DEER experiment. **C**: ESE-detected fieldsweep colored in the same fashion as A and B.* _____ 41
*Figure 21: Field-dependent DEER measurements on a mixture of $[3G]_2$ (yellow), $[4G]_2$ (blue) and [3G][4G] (orange). **A**: Dipolar spectra for each field with each species fit with Gaussians. **B**: The relative intensities of each species. The sum of the total intensities for each field position was normalized. To better show the relative change for each species, the intensities for each species were additionally normalized to their mean value.* _____ 42
*Figure 22: Comparison of DEER and RIDME measurements. Measurements are taken on a mixture of $[3G]_2$ and $[4G]_2$ frozen directly after mixing. Measurements are taken at Q-band at 19 K for DEER and 30 K for RIDME. The mixing time for the RIDME measurements was set to 15 µs. Pump detect separation for DEER was 90 MHz. **A**: ESE detected fieldsweep with the pump and detect positions used for DEER marked. RIDME measurements were taken at the respective pump positions. **B**: Raw measurements. **B**: Background corrected measurements. Background correction was done with DEERanalysis, a third-order polynomial correction was used for the RIDME traces, while a third-order homogenous background was used for the DEER spectra. **D**: One-sided dipolar spectra. Both RIDME traces display ^{2}H ESEEM artefacts at around 7.7 MHz indicated by an asterisk.* _____ 43
*Figure 23: Field-dependent chirped pump pulse DEER measurements on $[4G]_2$ with chirped (pink) and and monochromatic (blue) pulses. **A**: ESE-detected fieldsweep of $[4G]_2$ with the detect (yellow) and pump (orange) positions marked. The width of the pump window is estimated using the easyspin function exciteprofile. **B**: The DEER traces for each field position. The traces for 1088.8 mT and 1043.6 mT were scaled up by a factor of 5 and 7 for visibility reasons. **C**:Dipolar spectra.*_____ 44
*Figure 24: $[3G]_2$ and $[4G]_2$ were mixed at 12 °C, forming [3G][4G]. DEER measurements were taken at 1182 mT. The trace at 0 min was constructed from the sum of $[3G]_2$ and $[4G]_2$, each mixed with $[3G_{nd}]$. **A**: Background corrected DEER traces of DEER measurements over time. **B**: Dipolar spectra with the fitted areas filled (yellow $[3G]_2$, orange [3G][4G], blue $[4G]_2$). **C**: The intensities fitted against the incubation time. Since the relation between signal strength and concentration is currently unknown, the signals for each species were normalized to the largest signal of that species. Stretched exponentials were fitted to the data to function as a guide to the eye.*_____ 44
*Figure 25: **A**: Schematic intercalation of PIPER into $[3G]_2$ with the change in distance that is measured with DEER indicated by green lines. **B**: MD-derived structural models of the PIPER@$[3G]_2$ sandwich complex (adapted from Stratmann, Kutin, et all. Angewandte Chemie 60, 4939–4947 (2021) under creative commons license (CC4))[29]*_____ 45
*Figure 26: $[3G]_2$ and PIPER were mixed at 12 °C (1:1). DEER measurements were taken at 1182 mT. **A**: Background corrected DEER traces of DEER measurements over time (same times as traces in B at the same height). **B**: Dipolar spectra with the fitted areas filled (yellow $[3G]_2$, violet PIPER@$[3G]_2$). **C**: The relative amounts plotted against the incubation time.*_____ 46
*Figure 27: $[4G]_2$ (blue) and PIPER@$[4G]_2$ (green) were brought to different temperatures for 15 min, then rapidly mixed with glycerol and flash frozen. DEER measurements were taken at 1182 mT. **A**: Background corrected DEER traces of samples at different temperatures. **B**: The corresponding dipolar spectra. **C**: The modulation depths plotted against temperature. Additionally, a $[4G]_2$ sample incubated at 48 °C for 30 min is shown in dark brown.* _____ 47
*Figure 28: $[4G]_2$ and PIPER were mixed at 4 °C (1:1). DEER measurements were taken at 1182 mT. **A**: Background corrected DEER traces of DEER measurements over time (same times as traces in B at the same height). **B**: Dipolar spectra with the fitted areas filled (blue $[4G]_2$, orange 2PIPER@$[4G]_2$). Additionally, PIPER@$[4G]_2$ is shown in green for comparison. **C**: The relative amounts plotted against the incubation time.* _____ 48
*Figure 29: **A**: Table of potentially EPR-active species that can exist in β_2. **B**: β_2-subunit with zoom in on the active iron-bound center.[140] **C**: Potential distances in β_2. The protein structure of manganese-bound β_2[141] was overlaid with the structure of iron-bound β_2. Tyr_{122} a and b belong to the iron- and manganese-bound structure, respectively. Distances within the respective subunits are not shown as they are too short to be recorded with DEER.*_____ 54
*Figure 30: **A**: ESE- detected field-sweep of 1-Mn-5Fe:2h, measured at 5 dB with long shot repetition time (highlighting the Tyr-signal) and 20 dB with short shot repetition time (highlighting the manganese*

signal) power. The pump and detect positions used for Tyr-Tyr DEER are indicated. ***B****: Zoom in on the Tyr-signal.* 55
Figure 31: Tyr-Tyr DEER measured on 1-Mn-5Fe:1min,15min,1h,2h time series (A-B) and 1,2,3-Mn-5Fe:wash concentration series (C-D). ***A****&****C****: Background corrected DEER traces.* ***B****&****D****: Distances with uncertainties as calculated by DEER-analysis given as the shaded area. Raw and dipolar spectra can be found in Chapter 5.3.* 56
Figure 32: ESE-detected fieldsweep of 1-Mn-5Fe:2h, measured at low and high pulse power to highlight manganese and Tyr•. The position of the detection sequence used for Tyr-FeMn DEER is marked. The pump pulse is indicated by its inversion profile. The inversion profile was calculated with the EasySpin function exciteprofile. 56
Figure 33: Tyr-Metal DEER measurements on 1-Mn-5Fe:1min, 15min, 1h, 2h. ***A****: Raw DEER traces.* ***B****: Background corrected DEER traces.* ***C****: Dipolar spectra. The frequencies associated with the Tyr-Tyr and Tyr-Metal distance are marked. Furthermore, the dipolar spectra associated with the respective frequencies of each distance (taken from fit of 1 eq. Mn^{2+} sample in Figure 35) are shown.* ***D****: Results of distance analysis with uncertainty estimates.* 57
Figure 34: Tyr-Metal RIDME measurements on 2-Mn-5Fe:wash ***A****: Raw RIDME trace.* ***B****: Background corrected RIDME trace with the corresponding DEER trace from Figure 35 plotted for reference.* ***C****: Dipolar spectrum. The corresponding dipolar spectrum from DEER, as well as the DEER spectrum scaled up to double and triple the frequency (1,2,3. Harm.), are plotted to illustrate the overtones present in the RIDME spectrum.* ***D****: Results of distance analysis with distances resulting from the overtones highlighted.* 59
Figure 35: Tyr-Metal DEER measurements on 1,2,3-Mn-5Fe:wash ***A****: Raw DEER traces.* ***B****: Background corrected DEER traces.* ***C****: Dipolar spectra.* ***D****: Results of distance analysis with uncertainty estimates.* 60
Figure 36: ***A****: 4 dB ESE-detected fieldsweeps of 1 eq. manganese samples from each concentration series and free manganese. The spectra were normalized to the left shoulder (1123-1172 mT), and pseudo-modulated with a modulation amplitude of 8 mT.* ***B****: 20 dB ESE-detected fieldsweeps of 1,2,3-Mn:wash as well as 1,2,3-Mn:rep. All spectra were normalized by maximizing the left shoulder (900-1160 mT).* ***C****: ESE- detected fieldsweep of free manganase, 1-Mn:rep recorded at low power to highlight the mono-manganese signal, and 1-Mn-5Fe:2h measured at 4 dB to highlight the Tyr-signal. The pump and detect positions used for Mn-Mn DEER are indicated.* 62
Figure 37: Mn-Mn DEER measurements on β_2 with 1, 2 & 3 eq. Mn^{2+} added. ***A****-****C****: The samples were washed after the addition of manganese to remove free manganese. Buffer was bubbled through with nitrogen gas.* ***D****-****F****: Samples were prepared anaerobically in a glovebox but not washed.* ***G****-****L****: Samples were prepared without washing or any measures to restrict oxygen access.* ***Top row****: Background corrected DEER traces.* ***Middle row****: Dipolar spectra with fits indicated in grey.* ***Bottom row****: Distance distributions with uncertainty estimates.* 63
Figure 38: Mn-Mn DEER measurements on 1-Mn-5Fe:1min,15min,1h,2h. ***A****: Raw DEER traces.* ***B****: Background corrected DEER traces.* ***C****: Dipolar spectra with the fits from distance analysis in grey. The fit for 1 eq. was scaled down by a factor of 5 due to its very poor quality.* ***D****: Results of distance analysis with uncertainty estimates.* 64
Figure 39: Mn-Mn DEER measurements on 1,2,3-Mn-5Fe:wash. ***A****: Raw DEER traces.* ***B****: Background corrected DEER traces.* ***C****: Dipolar spectra.* ***D****: Results of distance analysis with uncertainty estimates.* 65
Figure 40: Simulation of the respective transitions of free Mn^{2+} ($\pm 52 \leftrightarrow \pm 32$ in yellow, $\pm 32 \leftrightarrow \pm 12$ in orange and, $-12 \leftrightarrow +12$ in blue). The transitions are labeled based on their preferred optimal pulse length/amplitude. 100% is assigned to the optimum for a $ms = -12 \leftrightarrow +12$ of a S=1/2 system.[102] 66
Figure 41: ***A****: ESE detected field-sweeps of 1-Mn-5Fe:1min,15min,1h,2h, recorded at 20 dB and 10 K. All samples mostly display the narrow lines associated with free Mn^{2+}. Spectra are normalized to the height of the first peak. Additionally, a spectrum of free Mn^{2+} is plotted in grey for comparison. (Not normalized data in Figure 42b)* ***B****: CW measurements of the time series samples and a sample of free Mn^{2+} in buffer recorded in X-band at 15 K, with a modulation amplitude of 0.8 mT. The red shaded regions indicate the area where the FeMn signal is found (shading intensity equals the intensity of the signal). The FeMn signal was simulated based on the parameters measured by Pierce et al.[62] using the easyspin function pepper.[146] The spectra were scaled using the grey regions, as these regions*

only contain the free manganese signal. An asterisk marks a background signal. The measurements were recorded by Sergius Boschmann. _____ 66
Figure 42: ESE-detected Q-band field-sweeps of 1-Mn-5Fe:1min,15min,1h,2h recorded at 10 K. ***A****: Zoom in on the mono-Mn feature, recorded at 4 dB, pseudomodulated (20 mT). Additionally, to the time series, 1-Mn:wash is plotted, showing the characteristic mono-Mn signal.* ***B****: Zoom in on additional signal, recorded at 8 dB, displayed as first derivative (20 mT modulation amplitude).*_____ 67
Figure 43: ***A****: ESE-detected Q-band field-sweeps of 1-Mn-5Fe:1min,15min,1h,2h, recorded at 10 K. Zoom in on the FeMn feature recorded at 4 dB. Spectrum is shown as second derivative (4 mT modulation amplitude) to suppress the broader shallow shoulders of manganese. Arrows indicate the growth of signal.* ***B****: Intensity of the FeMn feature, calculated as the scaled mean value of the three features marked in (a). The scaling factors for the respective features were calculated as the mean value of the relative intensities of the features in the 1 & 2 h samples.* ***C****: Background densities of Mn-Mn DEER (Figure 38) as calculated by DEERanalysis. The values were corrected for variations in background order to align with the concentration-dependent expression for background density.* ***D****: Same background densities plotted against the concentration of FeMn, free manganese as calculated in Figure 41, and Tyr• as determined by previously established protocols.[147] The concentrations were rescaled to a range of 0 to 1 for better comparison.* _____ 68
Figure 44: Zoom in on ESE-detected field-swept spectra of the manganese concentration series samples. ***A****: Comparison of mono-Mn feature, measured at 4 dB, 20 mT pseudomodulated.* ***B****: Second-order pseudomodulated (4 mT) zoom on the FeMn signal region.* ***C****: Zoom in on the mono/di-Mn signal region, of the washed Mn concentration series, 20 mT pseudomodulated. Shown are the 1 eq spectrum,* _____ 69
Figure 45: ***A****: The first and second derivative peaks of the measurement pairs Meas A-E (Table 18) at the XQ-machine and Q-standalone are plotted against each other. A linear fit was reached for all points with 0.3134 µT/mT - 4.0703 mT.* ***B****-****G****: Exemplary zoom-in on the respective peaks of β_2 + 3 eq. Mn with and without the additional field correction applied to the XQ-Band data. The data is pseudo-modulated with a modulation amplitude of 1 mT.*_____ 76
Figure 46: Scaling of signals between Q-standalone and XQ-machine. For each comparison the XQ spectra were shifted and scaled to give the best fit. Since the high field signal drops of much faster with the XQ machine data above 1248.4 mT was not included in the fit (desaturated in the plot). The measurement pairs A-E are the same used in Figure 45 and ***A****: Spectra plotted with the best scaling factor for each comparison.* ***B****: Spectra plotted with the average scaling factor (88.46).* _____ 77
*Figure 47: Resonator profile of overcoupled QTII resonator. The resonator profile was determined via field- and frequency-dependent microwave nutations with subsequent Fourier transformation to extract the main Rabi-frequency. The resonator consists of three dips, a primary dip at 34 GHz, a secondary dip at 33.8 GHz, and another dip at almost 34.4 GHz. The secondary dip can be used for DEER with chirped pump pulses, where the detection sequence is placed in the secondary dip and the chirped pump pulse fills the primary dip.*_____ 78
Figure 48: Modulation depth of the Q-Band standalone and X/Q-band machine. _____ 79
Figure 49: ***A****: ESE detected field-sweeps of $[3G]_2$+PIPER after 4 hours, showing that the formation of PIPER@$[3G]_2$ does not influence the line shape. All spectra are pseudomodulated with a modulation amplitude of 3 mT. $[3G]_2$ and $[4G]_2$ are ploted for reference.* ***B****: ESE detected field-sweeps of PIPER@$[4G]_2$, showing that the formation of PIPER@$[4G]_2$ does not influence the line shape. All spectra are pseudomodulated with a modulation amplitude of 3 mT. $[3G]_2$ and $[4G]_2$ are ploted for reference.* _____ 80
Figure 50: Tyr-Tyr DEER measurements on β_2 with 1 eq. Mn^{2+} added, followed by the addition of 5 eq. Fe^{2+}. Samples are taken at 1 min, 15 min, 1 h, and 2 h after the addition of Fe^{2+}. ***A****: Raw DEER traces.* ***B****: Background corrected DEER traces.* ***C****: Dipolar spectra. The fits are included in gray.* ***D****: Results of distance analysis with uncertainty estimates.*_____ 80
Figure 51: Tyr-Tyr DEER measurements on β_2 with 1, 2 & 3 eq. Mn^{2+} added, followed by the addition of 5 eq. Fe^{2+}. Samples were washed 2 h after the addition of Fe^{2+} and frozen in liquid nitrogen. ***A****: Raw DEER traces.* ***B****: Background corrected DEER traces.* ***C****: Dipolar spectra. The fits are included in gray.* ***D****: Results of distance analysis with uncertainty estimates.* _____ 81
Figure 52: ESE-detected field-sweep of β_2 with 2 eq. Mn added, followed by the addition of 5 eq. Fe. Measurements were taken in a slightly overcoupled QTII resonator at 10 dB to highlight the Tyr-signal and at 14 dB to highlight the Mn signal. The position at which RIDME was measured is indicated.* __ 81

*Figure 53: **A**: Relative intensities of an echo as a function of pulse strength (normalized to optimal pulse strength for S=1/2) for the respective optimal pulse strengths of the different transitions in manganese. **B**: Fraction of -1/2=>1/2 transition over the remaining transitions as a function of pulse strength.* 82
*Figure 54: **A**: ESE detected field-sweeps of 1-Mn-5Fe:1min,15min,1h,2h, recorded at 20 dB and 10 K. All samples mostly display the narrow lines associated with free Mn^{2+}. Spectra are normalized to the height of the first peak. Additionally, a spectrum of free Mn^{2+} is plotted in grey for comparison. **B**: Same as (a) but only normalized to spectrometer parameters.* 82
*Figure 55: CW measurements of a time series repetition. Another 5 eq. of Fe^{2+} were added after the 2 h mark. The spectra were recorded in X-band at 15 K, with a modulation amplitude of 0.8 mT. Additionally, a sample of free Mn^{2+} in buffer is plotted. The spectra were scaled to maximize overlap in the grey regions. The red shaded regions indicate the area where the FeMn signal is found (shading intensity equals the intensity of the signal). An asterisk marks a background signal. The # marks the signal originating from mono-Mn at 1 min. The calculated amounts can be found in Table 19. The measurements were taken by Sergius Boschmann. **A**: spectra scaled for the shoulders to fit as in Figure 42a. **B**: Spectra only normalized for spectrometer parameters.* 83
*Figure 56: Determination of the optimal detect pulse length for the detection of the Tyr-radical in a sample with 1 eq. Mn^{2+} and 5 eq. Fe^{2+} added. **A**: ESE-detected field sweep with varying pulse length. Since the signal is the sum of both the manganese and Tyr* the difference between the peak and left shoulder is taken. **B**: The difference from A plotted against the pulse length. **C**: Comparison of a classic microwave nutation on the same sample and microwave nutation on a sample that only contains Tyr*, no Mn^{2+}.* 84
*Figure 57: Background-corrected Mn-Mn DEER measurements. The artefact is highlighted with a grey box. The sum of both spectra is generated while excluding the shaded areas. **A**: 3 eq. manganese, sample prepared in glovebox. **B**: 3 eq. manganese added, followed by 5 eq. of iron.* 85
*Figure 58: Mn-Mn DEER measurements on 100 µM $MnDOTA_2OPE$ in 50% (v/v) D_2O, glycerol-d8. **A**: Raw DEER trace with background fit. **B**: Background corrected DEER trace with fit from the distance analysis. **C**: Dipolar spectrum. The fits are included in gray. **D**: Result of the distance analysis with uncertainty estimates.* 86
*Figure 59: **A**: ESE-detected fieldsweep of free manganese and the $MnDOTA_2OPE$ ruler with the field positions used for T_2 measurements indicated. **B**: T_2 measurements.* 87
*Figure 60: **A**: ESE-detected field sweeps of $[3G]_2$ and $[4G]_2$. **B**: Dipolar spectra from RIDME measurements on $[3G]_2$ (lower spectra) and $[4G]_2$ (upper spectra). ESEEM artefacts are marked with an asterisk. **C**-**E**: T_1 measurements of $[3G]_2$ at 1043, 1177.4 and 1184 mT and their fits. Fitting parameters are shown in Table 21. **F**-**H**: T_1 measurements of $[4G]_2$ at 1043, 1177.4 and 1184 mT and their fits. Fitting parameters are shown in Table 5.* 89
*Figure 61: Field-dependent chirped pump pulse DEER measurements on $[4G]_2$ (blue) and PIPER@$[4G]_2$ (green). **A**: ESE-detected fieldsweeps of $[4G]_2$ and PIPER@$[4G]_2$ with the detect (yellow) and pump (orange) positions marked. The width of the pump window is estimated using the easyspin function exciteprofile. **B**: The DEER traces for each field position. The traces for 1150 mT and 1043.6 mT were scaled up by a factor of 5 for visibility reasons.* 91
Table 1: Evolution of an A-spin during a 4-pulse DEER sequence. The sequence with and without pumping the B-spin is shown. For both sequences, the states of the A and B spins during each evolution period are given, as well the phase the spin packets pick up during each evolution period. The sign of the phase contribution is given as the effective phase after all π-pulses have taken effect (eq. (15)). For the echo, the sum of all contributions during the sequence is given. In both scenarios, a second sequence, where the B-spin starts off as α can be constructed. This case leads to an inversion of the sign of the dipolar contribution. Since DEER and RIDME are not sensitive to the sign of the dipolar contribution, both pathways lead to the same signal.

25

101
Table 2: Flowchart for checking if DEER/RIDME experiment can have orientation selectivity. 29 101

Table 3: Overview of which combinations of A and B-spin orientation selection result in orientation selection on θ and Δ respectively. 33
101
Table 4: Intercalation modes found for different environments. PIPER equivalents are given relative to the amount of GQ-dimers. 47
10
1
Table 5: Overview of the used GQs. 48 101
Table 6: Measurement parameters for pulsed ESE-detected field sweeps 49 101
Table 7: Measurement parameters for microwave nutation for detect sequence 49 101
Table 8: Measurement parameters for microwave nutation for pump pulse 50 101
Table 9: Measurement parameters for GQ-GQ DEER with 16-step phasecycling $\pi 2 - \tau 1 - \pi - \tau 1 + t - p - \tau 2 - t - \pi - \tau 2 - Detect$ 50
101
Table 10: Measurement parameters for GQ-GQ RIDME with 8-step phasecycling $\pi 2 - \tau 1 - \pi - \tau 1 + t - \pi 2 - Tmix - \pi 2 - \tau 2 - t - \pi - \tau 2 - Detect$
5
0
1
01
Table 11: β_2 samples that were used in this section. Samples from the same batch are grouped together. Time series were prepared by taking samples from the same reaction vessel, concentration series were prepared in parallel.
7
0
1
01
Table 12: Measurement parameters for pulsed ESE-detected field sweeps 71 101
Table 13: Measurement parameters for Tyr-Tyr DEER with 16-step phasecycling $\pi 2 - \tau 1 - \pi - \tau 1 + t - p - \tau 2 - t - \pi - \tau 2 - Detect$ 71
101
Table 14: Measurement parameters for Tyr-FeMn DEER with 16-step phasecycling $\pi 2 - \tau 1 - \pi - \tau 1 + t - p - \tau 2 - t - \pi - \tau 2 - Detect$
71
101
Table 15: Measurement parameters for Mn-Mn DEER with 16-step phasecycling $\pi 2 - \tau 1 - \pi - \tau 1 + t - p - \tau 2 - t - \pi - \tau 2 - Detect$ 72
101
Table 16: Measurement parameters for Tyr-Metal RIDME, with 8-step phasecycling $\pi 2 - \tau 1 - \pi - \tau 1 + t - \pi 2 - Tmix - \pi 2 - \tau 2 - t - \pi - \tau 2 - Detect$ 72
101
Table 17: Power best estimate of equivalents between the XQ-machine and Q-standalone. 73 101
Table 18: The samples and respective measurements used to build the measurement pairs Meas A-E used for fieldshift correction and signal factor determination between the Q-standalone and XQ-machine (Figure 45 & Figure 46).
74
101

Table 19: Amount of free Mn^{2+} calculated for the repetition of the time series shown in Figure 55 scaled to the same scale as the first time series (Figure 42). The 1 min sample still contained some mono-Mn signal, skewing the calculated amounts. _____ *82*
_____ *101*
Table 20: Spectral fractions of the pump pulse of the 1 eq. Mn unwashed repetition, 3 eq. Mn unwashed repetition and manganese ruler sample for different microwave powers. The spectral fraction was calculated as the integral of the product of the inversion efficiency of the pump pulse and the spectral intensity divided by the integral of the total spectrum. The inversion efficiency was calculated using the inversion profile generated by the EasySpin function exciteprofile, with maximum inversion corresponding to a value of 1 and no inversion corresponding 0. The pulse was simulated with a length of 32 ns since this represents the average pump pulse length. However, changing the pulse length to 28 ns (shortest used pulse length) or 38 ns (longest used pulse length) does not change the relative values of the spectral fractions. *86*
101
Table 21: T_1 relaxation rates, measured RIDME modulation depths, calculated fraction of flipped B-spins, and based on those calculated, fraction of dimers for $[3G]_2$ and $[4G]_2$ measured at 30 K at different field positions. _*89*
_____ *101*
Table 22: The modulation depths of the measurements shown in Figure 61 for each field position. Additionally, the measurement at 1182 mT for monochromatic pump pulses (Figure 27) is listed for reference. _____*90*
_____ *102*

List of tables

Table 1: Evolution of an A-spin during a 4-pulse DEER sequence. The sequence with and without pumping the B-spin is shown. For both sequences, the states of the A and B spins during each evolution period are given, as well the phase the spin packets pick up during each evolution period. The sequence is given as the effective phase after all π-pulses have taken effect (eq. (15)). For the echo, the sum of all contributions during the sequence is given. In both scenarios, a second sequence, where the B-spin starts off as α can be constructed. This case leads to an inversion of the sign of the dipolar contribution. Since DEER and RIDME are not sensitive to the sign of the dipolar contribution, both pathways lead to the same signal. _____ *26*
Table 2: Flowchart for checking if DEER/RIDME experiment can have orientation selectivity. _____ *30*
Table 3: Overview of which combinations of A and B-spin orientation selection result in orientation selection on θ and Δ respectively. _____ *34*
Table 4: Intercalation modes found for different environments. PIPER equivalents are given relative to the amount of GQ-dimers. _____ *48*
Table 5: Overview of the used GQs. _____ *49*
Table 6: Measurement parameters for pulsed ESE-detected field sweeps _____ *50*
Table 7: Measurement parameters for microwave nutation for detect sequence _____ *50*
Table 8: Measurement parameters for microwave nutation for pump pulse _____ *51*
Table 9: Measurement parameters for GQ-GQ DEER with 16-step phasecycling $\pi 2 - \tau 1 - \pi - \tau 1 + t - p - \tau 2 - t - \pi - \tau 2 - Detect$ _____ *51*
Table 10: Measurement parameters for GQ-GQ RIDME with 8-step phasecycling $\pi 2 - \tau 1 - \pi - \tau 1 + t - \pi 2 - Tmix - \pi 2 - \tau 2 - t - \pi - \tau 2 - Detect$ _____ *51*
Table 11: β_2 samples that were used in this section. Samples from the same batch are grouped together. Time series were prepared by taking samples from the same reaction vessel, concentration series were prepared in parallel. _____ *71*
Table 12: Measurement parameters for pulsed ESE-detected field sweeps _____ *72*
Table 13: Measurement parameters for Tyr-Tyr DEER with 16-step phasecycling $\pi 2 - \tau 1 - \pi - \tau 1 + t - p - \tau 2 - t - \pi - \tau 2 - Detect$ _____ *72*
Table 14: Measurement parameters for Tyr-FeMn DEER with 16-step phasecycling $\pi 2 - \tau 1 - \pi - \tau 1 + t - p - \tau 2 - t - \pi - \tau 2 - Detect$ _____ *72*
Table 15: Measurement parameters for Mn-Mn DEER with 16-step phasecycling $\pi 2 - \tau 1 - \pi - \tau 1 + t - p - \tau 2 - t - \pi - \tau 2 - Detect$ _____ *73*
Table 16: Measurement parameters for Tyr-Metal RIDME, with 8-step phasecycling $\pi 2 - \tau 1 - \pi - \tau 1 + t - \pi 2 - Tmix - \pi 2 - \tau 2 - t - \pi - \tau 2 - Detect$ _____ *73*
Table 17: Power best estimate of equivalents between the XQ-machine and Q-standalone. _____ *74*
Table 18: The samples and respective measurements used to build the measurement pairs Meas A-E used for fieldshift correction and signal factor determination between the Q-standalone and XQ-machine (Figure 45 & Figure 46). _____ *75*
Table 19: Amount of free Mn^{2+} calculated for the repetition of the time series shown in Figure 55 scaled to the same scale as the first time series (Figure 42). The 1 min sample still contained some mono-Mn signal, skewing the calculated amounts. _____ *83*
Table 20: Spectral fractions of the pump pulse of the 1 eq. Mn unwashed repetition, 3 eq. Mn unwashed repetition and manganese ruler sample for different microwave powers. The spectral fraction was calculated as the integral of the product of the inversion efficiency of the pump pulse and the spectral intensity divided by the integral of the total spectrum. The inversion efficiency was calculated using the inversion profile generated by the EasySpin function exciteprofile, with maximum inversion corresponding to a value of 1 and no inversion corresponding 0. The pulse was simulated with a length of 32 ns since this represents the average pump pulse length. However, changing the pulse length to 28 ns (shortest used pulse length) or 38 ns (longest used pulse length) does not change the relative values of the spectral fractions. _____ *87*
Table 21: T_1 relaxation rates, measured RIDME modulation depths, calculated fraction of flipped B-spins, and based on those calculated, fraction of dimers for $[3G]_2$ and $[4G]_2$ measured at 30 K at different field positions. *90*

Table 22: The modulation depths of the measurements shown in Figure 61 for each field position. Additionally, the measurement at 1182 mT for monochromatic pump pulses (Figure 27) is listed for reference. _____ *91*

References

1. Evgeny Konstantinovich Zavoisky. The paramagnetic absorption of a solution in parallel fields. Journal of Physics 8, 377–380 (1944).
2. Evgeny Konstantinovich Zavoisky. Spin-magnetic resonance in paramagnetics. *Journal of Physics* **9,** 245 (1945).
3. Evgeny Konstantinovich Zavoisky. Paramagnetic relaxation of solutions of manganese(II) salts, under magnetic fields using microwave radiation. *Journal of Physics* **9,** 211–216 (1945).
4. Salikhov, K. M., Eaton, S. S. & Eaton, G. R. Celebration of 80 years of EPR. *Appl Magn Reson* **55,** 869–888; 10.1007/s00723-024-01688-2 (2024).
5. Jeschke, G. Quo vadis EPR? *Journal of magnetic resonance (San Diego, Calif. : 1997)* **306,** 36–41; 10.1016/j.jmr.2019.07.008 (2019).
6. Goldfarb, D. Pulse EPR in biological systems - Beyond the expert's courtyard. *Journal of magnetic resonance (San Diego, Calif. : 1997)* **306,** 102–108; 10.1016/j.jmr.2019.07.038 (2019).
7. van Doorslaer, S. & Murphy, D. M. EPR spectroscopy in catalysis. *Topics in current chemistry* **321,** 1–39; 10.1007/128_2011_237 (2012).
8. Chiesa, M. & Giamello, E. On the Role and Applications of Electron Magnetic Resonance Techniques in Surface Chemistry and Heterogeneous Catalysis. *Catal Lett* **151,** 3417–3436; 10.1007/s10562-021-03576-x (2021).
9. Hinderberger, D. EPR spectroscopy in polymer science. *Topics in current chemistry* **321,** 67–89; 10.1007/128_2011_236 (2012).
10. Abdel-Rehim, F., Basfar, A. A., Al-Kahtani, H. A. & Abu-Tarboush, H. M. The use of electron spin resonance spectroscopy for the detection of irradiated mackerel. *Applied Radiation and Isotopes* **48,** 241–245; 10.1016/S0969-8043(96)00214-X (1997).
11. Hennig, G. J. & Grün, R. ESR dating in quaternary geology. *Quaternary Science Reviews* **2,** 157–238; 10.1016/0277-3791(83)90006-9 (1983).
12. Swartz, H. M. *et al.* Clinical EPR: unique opportunities and some challenges. *Academic radiology* **21,** 197–206; 10.1016/j.acra.2013.10.011 (2014).
13. Haeri, H. H. *et al.* Identification of Patients with Pancreatic Cancer by Electron Paramagnetic Resonance Spectroscopy of Fatty Acid Binding to Human Serum Albumin. *ACS pharmacology & translational science* **3,** 1188–1198; 10.1021/acsptsci.0c00116 (2020).
14. Drescher, M. & Jeschke, G. *EPR Spectroscopy. Applications in Chemistry and Biology* (Springer Berlin Heidelberg, Berlin, Heidelberg, 2012).
15. Stoll, S., Calle, C., Mitrikas, G. & Schweiger, A. Peak suppression in ESEEM spectra of multinuclear spin systems. *Journal of magnetic resonance (San Diego, Calif. : 1997)* **177,** 93–101; 10.1016/j.jmr.2005.07.012 (2005).

16. Elpelt, A. *et al.* Investigation of TEMPO partitioning in different skin models as measured by EPR spectroscopy - Insight into the stratum corneum. *Journal of magnetic resonance (San Diego, Calif. : 1997)* **310,** 106637; 10.1016/j.jmr.2019.106637 (2019).

17. Ionita, G., Mocanu, S. & Matei, I. Conformational preferences of TEMPO type radicals in complexes with cyclodextrins revealed by a combination of EPR spectroscopy, induced circular dichroism and molecular modeling. *Phys. Chem. Chem. Phys.* **22,** 12154–12165; 10.1039/d0cp01937b (2020).

18. Bačić, G., Pavićević, A. & Peyrot, F. In vivo evaluation of different alterations of redox status by studying pharmacokinetics of nitroxides using magnetic resonance techniques. *Redox biology* **8,** 226–242; 10.1016/j.redox.2015.10.007 (2016).

19. Marko, A., Sojka, A., Laguta, O. & Neugebauer, P. Simulation of nitrogen nuclear spin magnetization of liquid solved nitroxides. *Phys. Chem. Chem. Phys.* **23,** 17310–17322; 10.1039/D0CP06071B (2021).

20. Armstrong, B. D. & Han, S. Overhauser Dynamic Nuclear Polarization To Study Local Water Dynamics. *J. Am. Chem. Soc.* **131,** 11270; 10.1021/ja904317z (2009).

21. Bordignon, E. EPR Spectroscopy of Nitroxide Spin Probes. In *eMagRes,* edited by R. K. Harris & R. L. Wasylishen (John Wiley & Sons, Ltd, Chichester, UK, 2007), pp. 235–254.

22. Pandelia, M.-E. *et al.* Characterization of a unique FeS cluster in the electron transfer chain of the oxygen tolerant NiFe hydrogenase from Aquifex aeolicus. *Proceedings of the National Academy of Sciences of the United States of America* **108,** 6097–6102; 10.1073/pnas.1100610108 (2011).

23. More, C. *et al.* A new approach for the structural study of metalloproteins: the quantitative analysis of intercenter magnetic interactions. *J Biol Inorg Chem* **1,** 152–161; 10.1007/s007750050034 (1996).

24. Dole, F. *et al.* Spin-spin interactions between the Ni site and the 4Fe-4S centers as a probe of light-induced structural changes in active Desulfovibrio gigas hydrogenase. *Biochemistry* **35,** 16399–16406; 10.1021/bi961662x (1996).

25. Heghmanns, M. *et al.* Distinct Valence States of the 4Fe4S Cluster Revealed in the Hydrogenase CrHydA1. *Angewandte Chemie (International ed. in English)* **64,** e202424167; 10.1002/anie.202424167 (2025).

26. van der Zwaan, J. W., Albracht, S., Fontijn, R. D. & Roelofs, Y. EPR evidence for direct interaction of carbon monoxide with nickel in hydrogenase from Chromatium vinosum. *Biochimica et Biophysica Acta (BBA) - Protein Structure and Molecular Enzymology* **872,** 208–215; 10.1016/0167-4838(86)90273-6 (1986).

27. Adams, M. W., Johnson, M. K., Zambrano, I. C. & Mortenson, L. E. On the novel H2-activating iron-sulfur center of the "Fe-only" hydrogenases. *Biochimie* **68,** 35–42; 10.1016/S0300-9084(86)81065-3 (1986).

28. Schumann, S. L. *et al.* Structure and Flexibility of Copper-Modified DNA G-Quadruplexes Investigated by 19 F ENDOR Experiments at 34 GHz. *Chemistry (Weinheim an der Bergstrasse, Germany)* **29,** e202302527; 10.1002/chem.202302527 (2023).

29. Stratmann, L. M., Kutin, Y., Kasanmascheff, M. & Clever, G. H. Precise Distance Measurements in DNA G-Quadruplex Dimers and Sandwich Complexes by Pulsed Dipolar EPR Spectroscopy. *Angewandte Chemie (International ed. in English)* **60,** 4939–4947; 10.1002/anie.202008618 (2021).

30. Eaton, G. R., Eaton, S. S., Barr, D. P. & Weber, R. T. *Quantitative EPR. A Practitioners Guide* (Springer Vienna, Vienna, 2010).

31. Reijerse, E. & Savitsky, A. Electron Paramagnetic Resonance Instrumentation. In *eMagRes,* edited by R. K. Harris & R. L. Wasylishen (John Wiley & Sons, Ltd, Chichester, UK, 2007), pp. 187–206.

32. van der Est, A. Continuous-Wave EPR. In *eMagRes,* edited by R. K. Harris & R. L. Wasylishen (John Wiley & Sons, Ltd, Chichester, UK, 2007), pp. 1411–1422.

33. Hahn, E. L. Spin Echoes. *Phys. Rev.* **80,** 580–594; 10.1103/PhysRev.80.580 (1950).

34. Eaton, S. S. & Eaton, G. R. Relaxation Mechanisms. In *eMagRes,* edited by R. K. Harris & R. L. Wasylishen (John Wiley & Sons, Ltd, Chichester, UK, 2007), pp. 1543–1556.

35. Abdullin, D. & Schiemann, O. Pulsed Dipolar EPR Spectroscopy and Metal Ions: Methodology and Biological Applications. *ChemPlusChem* **85,** 353–372; 10.1002/cplu.201900705 (2020).

36. Eaton, S. S. & Eaton, G. R. Measurement of Distances Between Electron Spins Using Pulsed EPR. In *Biomedical EPR,* edited by S. R. Eaton, G. R. Eaton & L. J. Berliner (Kluwer Academic/Plenum Publishers, New York, NY, 2005), Vol. 24/B, pp. 223–236.

37. Bode, B. E. *et al.* Counting the monomers in nanometer-sized oligomers by pulsed electron-electron double resonance. *Journal of the American Chemical Society* **129,** 6736–6745; 10.1021/ja065787t (2007).

38. Stubbe, J. & van der Donk, W. A. Protein Radicals in Enzyme Catalysis. *Chemical reviews* **98,** 705–762; 10.1021/cr9400875 (1998).

39. Zimanyi, C. M., Chen, P. Y.-T., Kang, G., Funk, M. A. & Drennan, C. L. Molecular basis for allosteric specificity regulation in class Ia ribonucleotide reductase from Escherichia coli. *eLife* **5,** e07141; 10.7554/eLife.07141 (2016).

40. Greene, B. L. *et al.* Ribonucleotide Reductases: Structure, Chemistry, and Metabolism Suggest New Therapeutic Targets. *Annual review of biochemistry* **89,** 45–75; 10.1146/annurev-biochem-013118-111843 (2020).

41. Nordlund, P. & Reichard, P. Ribonucleotide reductases. *Annual review of biochemistry* **75,** 681–706; 10.1146/annurev.biochem.75.103004.142443 (2006).

42. Elledge, S. J., Zhou, Z. & Allen, J. B. Ribonucleotide reductase: regulation, regulation, regulation. *Trends in biochemical sciences* **17,** 119–123; 10.1016/0968-0004(92)90249-9 (1992).

43. Jordan, A. & Reichard, P. Ribonucleotide reductases. *Annual review of biochemistry* **67,** 71–98; 10.1146/annurev.biochem.67.1.71 (1998).

44. Mathews, C. K. Deoxyribonucleotide metabolism, mutagenesis and cancer. *Nature reviews. Cancer* **15,** 528–539; 10.1038/nrc3981 (2015).

45. Rudd, S. G., Valerie, N. C. K. & Helleday, T. Pathways controlling dNTP pools to maintain genome stability. *DNA repair* **44,** 193–204; 10.1016/j.dnarep.2016.05.032 (2016).

46. Wang, N., Li, Y. & Zhou, J. Downregulation of ribonucleotide reductase subunits M2 induces apoptosis and G1 arrest of cervical cancer cells. *Oncology letters* **15,** 3719–3725; 10.3892/ol.2018.7806 (2018).

47. Ueno, H. *et al.* TAS1553, a small molecule subunit interaction inhibitor of ribonucleotide reductase, exhibits antitumor activity by causing DNA replication stress. *Communications biology* **5,** 571; 10.1038/s42003-022-03516-4 (2022).

48. Nagapara, J., Patel, B., Devliya, B., Chauhan, S. & Patel, H. D. Ribonucleotide reductase (RNR) inhibitors as target-based weapon for future cancer drug development. *Future medicinal chemistry* **17,** 1601–1622; 10.1080/17568919.2025.2527596 (2025).

49. Chen, S. *et al.* Ribonucleotide reductases in cancer: Mechanisms, clinical progress, and prospects. *Cell Investigation* **1,** 100034; 10.1016/j.clnves.2025.100034 (2025).

50. Wnuk, S. F. & Robins, M. J. Ribonucleotide reductase inhibitors as anti-herpes agents. *Antiviral research* **71,** 122–126; 10.1016/j.antiviral.2006.03.002 (2006).

51. Tholander, F. & Sjöberg, B.-M. Discovery of antimicrobial ribonucleotide reductase inhibitors by screening in microwell format. *Proceedings of the National Academy of Sciences of the United States of America* **109,** 9798–9803; 10.1073/pnas.1113051109 (2012).

52. Panesso, M. P. *et al.* Ribonucleotide reductase as a therapeutic target for drug repurposing as anthelmintics. *Experimental parasitology* **255,** 108641; 10.1016/j.exppara.2023.108641 (2023).

53. Narasimhan, J. *et al.* Ribonucleotide reductase, a novel drug target for gonorrhea. *eLife* **11**; 10.7554/eLife.67447 (2022).

54. Ruskoski, T. B. & Boal, A. K. The periodic table of ribonucleotide reductases. *The Journal of biological chemistry* **297,** 101137; 10.1016/j.jbc.2021.101137 (2021).

55. Kang, G., Taguchi, A. T., Stubbe, J. & Drennan, C. L. Structure of a trapped radical transfer pathway within a ribonucleotide reductase holocomplex. *Science (New York, N.Y.)* **368,** 424–427; 10.1126/science.aba6794 (2020).

56. Aye, Y., Li, M., Long, M. J. C. & Weiss, R. S. Ribonucleotide reductase and cancer: biological mechanisms and targeted therapies. *Oncogene* **34,** 2011–2021; 10.1038/onc.2014.155 (2015).

57. Seyedsayamdost, M. R., Xie, J., Chan, C. T. Y., Schultz, P. G. & Stubbe, J. Site-specific insertion of 3-aminotyrosine into subunit alpha2 of E. coli ribonucleotide reductase: direct

evidence for involvement of Y730 and Y731 in radical propagation. *Journal of the American Chemical Society* **129,** 15060–15071; 10.1021/ja076043y (2007).

58. Ravichandran, K. R., Minnihan, E. C., Wei, Y., Nocera, D. G. & Stubbe, J. Reverse Electron Transfer Completes the Catalytic Cycle in a 2,3,5-Trifluorotyrosine-Substituted Ribonucleotide Reductase. *Journal of the American Chemical Society* **137,** 14387–14395; 10.1021/jacs.5b09189 (2015).

59. Tong, W. H. *et al.* Mechanism of Assembly of the Diferric Cluster−Tyrosyl Radical Cofactor of Escherichia coli Ribonucleotide Reductase from the Diferrous Form of the R2 Subunit. *Journal of the American Chemical Society* **118,** 2107–2108; 10.1021/ja952764y (1996).

60. Bollinger, J. M. *et al.* Mechanism of Assembly of the Tyrosyl Radical-Diiron(III) Cofactor of E. coli Ribonucleotide Reductase. 2. Kinetics of The Excess Fe2+ Reaction by Optical, EPR, and Moessbauer Spectroscopies. *Journal of the American Chemical Society* **116,** 8015–8023; 10.1021/ja00097a008 (1994).

61. Atta, M., Nordlund, P., Aberg, A., Eklund, H. & Fontecave, M. Substitution of manganese for iron in ribonucleotide reductase from Escherichia coli. Spectroscopic and crystallographic characterization. *The Journal of biological chemistry* **267,** 20682–20688 (1992).

62. Pierce, B. S., Elgren, T. E. & Hendrich, M. P. Mechanistic implications for the formation of the diiron cluster in ribonucleotide reductase provided by quantitative EPR spectroscopy. *Journal of the American Chemical Society* **125,** 8748–8759; 10.1021/ja021290h (2003).

63. Pierce, B. S. & Hendrich, M. P. Local and global effects of metal binding within the small subunit of ribonucleotide reductase. *Journal of the American Chemical Society* **127,** 3613–3623; 10.1021/ja0491937 (2005).

64. Slonczewski, J. & Foster, J. W. *Mikrobiologie. Eine Wissenschaft mit Zukunft.* 2nd ed. (Springer Spektrum, Berlin, Heidelberg, 2012).

65. WATSON, J. D. & CRICK, F. H. Molecular structure of nucleic acids; a structure for deoxyribose nucleic acid. *Nature* **171,** 737–738; 10.1038/171737a0 (1953).

66. Zheng, K.-W. *et al.* Detection of genomic G-quadruplexes in living cells using a small artificial protein. *Nucleic acids research* **48,** 11706–11720; 10.1093/nar/gkaa841 (2020).

67. Chambers, V. S. *et al.* High-throughput sequencing of DNA G-quadruplex structures in the human genome. *Nature biotechnology* **33,** 877–881; 10.1038/nbt.3295 (2015).

68. Hänsel-Hertsch, R. *et al.* G-quadruplex structures mark human regulatory chromatin. *Nature genetics* **48,** 1267–1272; 10.1038/ng.3662 (2016).

69. Cueny, R. R., McMillan, S. D. & Keck, J. L. G-quadruplexes in bacteria: insights into the regulatory roles and interacting proteins of non-canonical nucleic acid structures. *Critical reviews in biochemistry and molecular biology* **57,** 539–561; 10.1080/10409238.2023.2181310 (2022).

70. Tian, T., Chen, Y.-Q., Wang, S.-R. & Zhou, X. G-Quadruplex: A Regulator of Gene Expression and Its Chemical Targeting. *Chem* **4,** 1314–1344; 10.1016/j.chempr.2018.02.014 (2018).

71. Rhodes, D. & Lipps, H. J. G-quadruplexes and their regulatory roles in biology. *Nucleic acids research* **43,** 8627–8637; 10.1093/nar/gkv862 (2015).

72. Hänsel-Hertsch, R., Di Antonio, M. & Balasubramanian, S. DNA G-quadruplexes in the human genome: detection, functions and therapeutic potential. *Nature reviews. Molecular cell biology* **18,** 279–284; 10.1038/nrm.2017.3 (2017).

73. Bochman, M. L., Paeschke, K. & Zakian, V. A. DNA secondary structures: stability and function of G-quadruplex structures. *Nature reviews. Genetics* **13,** 770–780; 10.1038/nrg3296 (2012).

74. Fleming, A. M. & Burrows, C. J. Interplay of Guanine Oxidation and G-Quadruplex Folding in Gene Promoters. *Journal of the American Chemical Society* **142,** 1115–1136; 10.1021/jacs.9b11050 (2020).

75. Yu, H.-Q., Miyoshi, D. & Sugimoto, N. Characterization of structure and stability of long telomeric DNA G-quadruplexes. *Journal of the American Chemical Society* **128,** 15461–15468; 10.1021/ja064536h (2006).

76. Kolesnikova, S. & Curtis, E. A. Structure and Function of Multimeric G-Quadruplexes. *Molecules (Basel, Switzerland)* **24**; 10.3390/molecules24173074 (2019).

77. Robinson, J., Raguseo, F., Nuccio, S. P., Liano, D. & Di Antonio, M. DNA G-quadruplex structures: more than simple roadblocks to transcription? *Nucleic acids research* **49,** 8419–8431; 10.1093/nar/gkab609 (2021).

78. Bierer, D. E. *et al.* Ethnobotanical-directed discovery of the antihyperglycemic properties of cryptolepine: its isolation from Cryptolepis sanguinolenta, synthesis, and in vitro and in vivo activities. *Journal of medicinal chemistry* **41,** 894–901; 10.1021/jm9704816 (1998).

79. Zhou, J.-L. *et al.* Synthesis and evaluation of quindoline derivatives as G-quadruplex inducing and stabilizing ligands and potential inhibitors of telomerase. *Journal of medicinal chemistry* **48,** 7315–7321; 10.1021/jm050041b (2005).

80. Tera, M. *et al.* Macrocyclic hexaoxazoles as sequence- and mode-selective G-quadruplex binders. *Angewandte Chemie (International ed. in English)* **47,** 5557–5560; 10.1002/anie.200801235 (2008).

81. Chung, W. J. *et al.* Solution structure of an intramolecular (3 + 1) human telomeric G-quadruplex bound to a telomestatin derivative. *Journal of the American Chemical Society* **135,** 13495–13501; 10.1021/ja405843r (2013).

82. Kern, J. T. & Kerwin, S. M. The aggregation and G-quadruplex DNA selectivity of charged 3,4,9,10-perylenetetracarboxylic acid diimides. *Bioorganic & medicinal chemistry letters* **12,** 3395–3398; 10.1016/S0960-894X(02)00763-1 (2002).

83. Shu, H., Zhang, R., Xiao, K., Yang, J. & Sun, X. G-Quadruplex-Binding Proteins: Promising Targets for Drug Design. *Biomolecules* **12**; 10.3390/biom12050648 (2022).

84. Prieto Otoya, T. D., McQuaid, K. T. & Cardin, C. J. Structural insights into G-quadruplex binding by metal complexes: implications for drug design. *Med Chem Res* **33,** 2001–2019; 10.1007/s00044-024-03309-w (2024).

85. Wang, K.-B., Wang, Y., Dickerhoff, J. & Yang, D. DNA G-Quadruplexes as Targets for Natural Product Drug Discovery. *Engineering (Beijing, China)* **38,** 39–51; 10.1016/j.eng.2024.03.015 (2024).

86. Vianney, Y. M. & Weisz, K. Indoloquinoline Ligands Favor Intercalation at Quadruplex-Duplex Interfaces. *Chemistry (Weinheim an der Bergstrasse, Germany)* **28,** e202103718; 10.1002/chem.202103718 (2022).

87. Yatsunyk, L. A. *et al.* Guided assembly of tetramolecular G-quadruplexes. *ACS nano* **7,** 5701–5710; 10.1021/nn402321g (2013).

88. Mergny, J.-L. & Sen, D. DNA Quadruple Helices in Nanotechnology. *Chemical reviews* **119,** 6290–6325; 10.1021/acs.chemrev.8b00629 (2019).

89. Liu, X. *et al.* Chemical and photochemical DNA "gears" reversibly control stiffness, shape-memory, self-healing and controlled release properties of polyacrylamide hydrogels. *Chemical science* **10,** 1008–1016; 10.1039/c8sc04292f (2019).

90. Engelhard, D. M., Meyer, A., Berndhäuser, A., Schiemann, O. & Clever, G. H. Di-copper(ii) DNA G-quadruplexes as EPR distance rulers. *Chemical communications (Cambridge, England)* **54,** 7455–7458; 10.1039/c8cc04053b (2018).

91. Fedoroff, O. Y. *et al.* NMR-Based model of a telomerase-inhibiting compound bound to G-quadruplex DNA. *Biochemistry* **37,** 12367–12374; 10.1021/bi981330n (1998).

92. Bogetti, X., Hasanbasri, Z., Hunter, H. R. & Saxena, S. An optimal acquisition scheme for Q-band EPR distance measurements using Cu2+-based protein labels. *Phys. Chem. Chem. Phys.* **24,** 14727–14739; 10.1039/d2cp01032a (2022).

93. Harris, R. K. & Wasylishen, R. L. (eds.). *eMagRes* (John Wiley & Sons, Ltd, Chichester, UK, 2007).

94. Eaton, S. R., Eaton, G. R. & Berliner, L. J. (eds.). *Biomedical EPR* (Kluwer Academic/Plenum Publishers, New York, NY, 2005).

95. Goldfarb, D. & Stoll, S. (eds.). *EPR spectroscopy. Fundamentals and methods* (Wiley, Chichester, West Sussex, 2018).

96. Schweiger, A. & Jeschke, G. *Principles of pulse electron paramagnetic resonance* (Oxford Univ. Press, Oxford, 2005).

97. Tiesinga, E., Mohr, P. J., Newell, D. B. & Taylor, B. N. CODATA Recommended Values of the Fundamental Physical Constants: 2018. *Journal of physical and chemical reference data* **50,** 33105; 10.1063/5.0064853 (2021).

98. Clayton, J. A. *et al.* Quantitative analysis of zero-field splitting parameter distributions in Gd(iii) complexes. *Phys. Chem. Chem. Phys.* **20,** 10470–10492; 10.1039/C7CP08507A (2018).

99. Borel, A., Tóth, E., Helm, L., Jánossy, A. & Merbach, A. E. EPR on aqueous Gd3+ complexes and a new analysis method considering both line widths and shifts. *Phys. Chem. Chem. Phys.* **2,** 1311–1317; 10.1039/a909553e (2000).

100. Bencini, A. & Gatteschi, D. *Electron Paramagnetic Resonance of Exchange Coupled Systems* (Springer Berlin Heidelberg, Berlin, Heidelberg, 1990).

101. Joutsuka, T. & Tanimura, Y. Detecting the Dzyaloshinskii–Moriya interaction by means of pulsed EPR spectroscopy. *Chemical Physics Letters* **457,** 237–240; 10.1016/j.cplett.2008.03.074 (2008).

102. Hofbauer, W. & Bittl, R. A novel approach to separating EPR lines arising from species with different transition moments. *Journal of magnetic resonance (San Diego, Calif. : 1997)* **147,** 226–231; 10.1006/jmre.2000.2202 (2000).

103. Astashkin, A. V. & Schweiger, A. Electron-spin transient nutation: a new approach to simplify the interpretation of ESR spectra. *Chemical Physics Letters* **174,** 595–602; 10.1016/0009-2614(90)85493-V (1990).

104. Barbon, A., Rusetsky, G. A., Linarello, S., Strzelczyk, R. & Fedaruk, R. Peculiarities in Rabi oscillations for fast-relaxing electron spins. *Journal of magnetic resonance (San Diego, Calif. : 1997)* **368,** 107781; 10.1016/j.jmr.2024.107781 (2024).

105. Fedaruk, R. *et al.* Continuous-wave and pulsed EPR studies of glass-like carbon with high spin concentration: Evidence for triplet states. *Carbon* **213,** 118270; 10.1016/j.carbon.2023.118270 (2023).

106. Bowman, M. K., Chen, H. & Maryasov, A. G. Fourier-Transform EPR. In *eMagRes,* edited by R. K. Harris & R. L. Wasylishen (John Wiley & Sons, Ltd, Chichester, UK, 2007), pp. 387–406.

107. Stoll, S. Pulse EPR. In *eMagRes,* edited by R. K. Harris & R. L. Wasylishen (John Wiley & Sons, Ltd, Chichester, UK, 2007), pp. 23–38.

108. Johnston, D. C. Stretched exponential relaxation arising from a continuous sum of exponential decays. *Phys. Rev. B* **74**; 10.1103/PhysRevB.74.184430 (2006).

109. Jeschke, G. Dipolar Spectroscopy - Double-Resonance Methods. In *eMagRes,* edited by R. K. Harris & R. L. Wasylishen (John Wiley & Sons, Ltd, Chichester, UK, 2007), pp. 1459–1476.

110. Schöps, P., Spindler, P. E., Marko, A. & Prisner, T. F. Broadband spin echoes and broadband SIFTER in EPR. *Journal of magnetic resonance (San Diego, Calif. : 1997)* **250,** 55–62; 10.1016/j.jmr.2014.10.017 (2015).

111. Borbat, P. P. & Freed, J. H. Multiple-quantum ESR and distance measurements. *Chemical Physics Letters* **313,** 145–154; 10.1016/S0009-2614(99)00972-0 (1999).

112. Milov, A. D., Salikhov, K. M. & Shirov, M. Use of the double resonance in electron spin echo method for the study of paramagnetic center spatial distribution in solids. *Fizika Tverdogo Tela* **23,** 975–982 (1981).

113. Milov, A. D., Salikhov, K. M. & Shirov, M. D. Application of the double resonance method to electron spin echo in a study of the spatial distribution of paramagnetic centers in solids. *Sov. Phys. Solid State* **23,** 565–569 (1981).

114. Kuzin, S. & Yulikov, M. RIDME Spectroscopy: New Topics Beyond the Determination of Electron Spin-Spin Distances. *The journal of physical chemistry letters* **16,** 1024–1037; 10.1021/acs.jpclett.4c02667 (2025).

115. Bowman, M. K., Maryasov, A. G., Kim, N. & DeRose, V. J. Visualization of distance distribution from pulsed double electron-electron resonance data. *Appl Magn Reson* **26,** 23–39; 10.1007/BF03166560 (2004).

116. Milov, A. D. & Tsvetkov, Y. D. Double electron-electron resonance in electron spin echo: Conformations of spin-labeled poly-4-vinilpyridine in glassy solutions. *Appl Magn Reson* **12,** 495–504; 10.1007/BF03164129 (1997).

117. Jeschke, G. *et al.* DeerAnalysis2006—a comprehensive software package for analyzing pulsed ELDOR data. *Appl Magn Reson* **30,** 473–498; 10.1007/BF03166213 (2006).

118. Fábregas Ibáñez, L. & Jeschke, G. Optimal background treatment in dipolar spectroscopy. *Physical chemistry chemical physics : PCCP*; 10.1039/c9cp06111h (2020).

119. Kattnig, D. R., Reichenwallner, J. & Hinderberger, D. Modeling excluded volume effects for the faithful description of the background signal in double electron-electron resonance. *The journal of physical chemistry. B* **117,** 16542–16557; 10.1021/jp408338q (2013).

120. Keller, K. *et al.* Intermolecular background decay in RIDME experiments. *Physical chemistry chemical physics : PCCP* **21,** 8228–8245; 10.1039/c8cp07815g (2019).

121. Kuzin, S., Jeschke, G. & Yulikov, M. Diffusion equation for the longitudinal spectral diffusion: the case of the RIDME experiment. *Phys. Chem. Chem. Phys.* **24,** 23517–23531; 10.1039/d2cp03039j (2022).

122. Bode, B. E., Plackmeyer, J., Bolte, M., Prisner, T. F. & Schiemann, O. PELDOR on an exchange coupled nitroxide copper(II) spin pair. *Journal of Organometallic Chemistry* **694,** 1172–1179; 10.1016/j.jorganchem.2008.11.029 (2009).

123. Keller, K. *et al.* Accessing distributions of exchange and dipolar couplings in stiff molecular rulers with Cu(II) centres. *Phys. Chem. Chem. Phys.* **22,** 21707–21730; 10.1039/d0cp03105d (2020).

124. Abdullin, D. AnisoDipFit: Simulation and Fitting of Pulsed EPR Dipolar Spectroscopy Data for Anisotropic Spin Centers. *Appl Magn Reson* **51,** 725–748; 10.1007/s00723-020-01214-0 (2020).

125. Bedilo, A. F. & Maryasov, A. G. Electron Spin Resonance of Dipole-Coupled Anisotropic Pairs in Disordered Systems. Secular Approximation for Point Dipoles. *Journal of Magnetic Resonance, Series A* **116,** 87–96; 10.1006/jmra.1995.1193 (1995).

126. Pake, G. E. Nuclear Resonance Absorption in Hydrated Crystals: Fine Structure of the Proton Line. *The Journal of Chemical Physics* **16,** 327–336; 10.1063/1.1746878 (1948).

127. Bowen, A. M., Tait, C. E., Timmel, C. R. & Harmer, J. R. Orientation-Selective DEER Using Rigid Spin Labels, Cofactors, Metals, and Clusters. In *Structural Information from Spin-Labels and Intrinsic Paramagnetic Centres in the Biosciences,* edited by C. R. Timmel & J. R. Harmer (Springer Berlin Heidelberg, Berlin, Heidelberg, 2013), Vol. 152, pp. 283–327.

128. Parkinson, G. N., Lee, M. P. H. & Neidle, S. Crystal structure of parallel quadruplexes from human telomeric DNA. *Nature* **417,** 876–880; 10.1038/nature755 (2002).

129. Bose, K., Lech, C. J., Heddi, B. & Phan, A. T. High-resolution AFM structure of DNA G-wires in aqueous solution. *Nature communications* **9,** 1959; 10.1038/s41467-018-04016-y (2018).

130. Sen, D. & Gilbert, W. Novel DNA superstructures formed by telomere-like oligomers. *Biochemistry* **31,** 65–70; 10.1021/bi00116a011 (1992).

131. Casto, J., Palit, S. & Saxena, S. PELDOR to the Metal: Cu(II)-Based Labels Put a New Spin on Distance Measurements. *Appl Magn Reson* **55,** 889–922; 10.1007/s00723-024-01658-8 (2024).

132. Shin-ya, K. *et al.* Telomestatin, a novel telomerase inhibitor from Streptomyces anulatus. *J. Am. Chem. Soc.* **123,** 1262–1263; 10.1021/ja005780q (2001).

133. Kern, J. T., Thomas, P. W. & Kerwin, S. M. The relationship between ligand aggregation and G-quadruplex DNA selectivity in a series of 3,4,9,10-perylenetetracarboxylic acid diimides. *Biochemistry* **41,** 11379–11389; 10.1021/bi0263107 (2002).

134. Schmidt, T., Ghirlando, R., Baber, J. & Clore, G. M. Quantitative Resolution of Monomer-Dimer Populations by Inversion Modulated DEER EPR Spectroscopy. *Chemphyschem : a European journal of chemical physics and physical chemistry* **17,** 2987–2991; 10.1002/cphc.201600726 (2016).

135. Tessmer, M. H. & Stoll, S. Protein Modeling with DEER Spectroscopy. *Annual review of biophysics* **54,** 35–57; 10.1146/annurev-biophys-030524-013431 (2025).

136. Kubatova, N., Schmidt, T., Schwieters, C. D. & Clore, G. M. Quantitative analysis of sterol-modulated monomer-dimer equilibrium of the β1-adrenergic receptor by DEER spectroscopy. *Proceedings of the National Academy of Sciences of the United States of America* **120,** e2221036120; 10.1073/pnas.2221036120 (2023).

137. Breitgoff, F. D. *et al.* UWB DEER and RIDME distance measurements in Cu(II)-Cu(II) spin pairs. *Journal of magnetic resonance (San Diego, Calif. : 1997),* 106560; 10.1016/j.jmr.2019.07.047 (2019).

138. Kato, Y., Ohyama, T., Mita, H. & Yamamoto, Y. Dynamics and thermodynamics of dimerization of parallel G-quadruplexed DNA formed from d(TTAGn) (n=3-5). *Journal of the American Chemical Society* **127,** 9980–9981; 10.1021/ja050191b (2005).

139. Ralph T. Weber. Bruker SpinJet AWG User's Guide. AWG Manual, 2017.

140. Oyala, P. H. *et al.* Biophysical Characterization of Fluorotyrosine Probes Site-Specifically Incorporated into Enzymes: E. coli Ribonucleotide Reductase As an Example. *Journal of the American Chemical Society* **138,** 7951–7964; 10.1021/jacs.6b03605 (2016).

141. Högbom, M., Andersson, M. E. & Nordlund, P. Crystal structures of oxidized dinuclear manganese centres in Mn-substituted class I ribonucleotide reductase from Escherichia coli: carboxylate shifts with implications for O2 activation and radical generation. *Journal of biological inorganic chemistry : JBIC : a publication of the Society of Biological Inorganic Chemistry* **6,** 315–323; 10.1007/s007750000205 (2001).

142. Jeschke, G., Pribitzer, S. & Doll, A. Coherence Transfer by Passage Pulses in Electron Paramagnetic Resonance Spectroscopy. *The journal of physical chemistry. B* **119,** 13570–13582; 10.1021/acs.jpcb.5b02964 (2015).

143. Spindler, P. E., Schöps, P., Kallies, W., Glaser, S. J. & Prisner, T. F. Perspectives of shaped pulses for EPR spectroscopy. *Journal of magnetic resonance (San Diego, Calif. : 1997)* **280,** 30–45; 10.1016/j.jmr.2017.02.023 (2017).

144. Keller, K. *et al.* High-spin Metal Centres in Dipolar EPR Spectroscopy. *Chimia* **72,** 216–220; 10.2533/chimia.2018.216 (2018).

145. Keller, K. *et al.* Computing distance distributions from dipolar evolution data with overtones: RIDME spectroscopy with Gd(iii)-based spin labels. *Physical chemistry chemical physics : PCCP* **19,** 17856–17876; 10.1039/c7cp01524k (2017).

146. Stoll, S. Spectral simulations in solid-state electron paramagnetic resonance. ETH Zurich, 2003.

147. Shari Lorraine Meichsner. Tracing protein native radicals under in vitro and in vivo conditions via EPR. E. coli class Ia ribonucleotide reductase as a paradigm. TU Dortmund, November 2022.

148. Ralph T. Weber. ELEXSYS II E 500 User's Guide. E500 (SPU) - Manual, 2013.

149. Tait, C. E. & Stoll, S. Coherent pump pulses in Double Electron Electron Resonance spectroscopy. *Physical chemistry chemical physics : PCCP* **18,** 18470–18485; 10.1039/c6cp03555h (2016).

150. Demay-Drouhard, P. *et al.* A Bis-Manganese(II)-DOTA Complex for Pulsed Dipolar Spectroscopy. *Chemphyschem : a European journal of chemical physics and physical chemistry* **17,** 2066–2078; 10.1002/cphc.201600234 (2016).

151. Ritsch, I., Hintz, H., Jeschke, G., Godt, A. & Yulikov, M. Improving the accuracy of Cu(ii)-nitroxide RIDME in the presence of orientation correlation in water-soluble Cu(ii)-nitroxide rulers. *Physical chemistry chemical physics : PCCP* **21,** 9810–9830; 10.1039/c8cp06573j (2019).

152. Savitsky, A., Dubinskii, A. A., Flores, M., Lubitz, W. & Möbius, K. Orientation-resolving pulsed electron dipolar high-field EPR spectroscopy on disordered solids: I. Structure of spin-correlated radical pairs in bacterial photosynthetic reaction centers. *The journal of physical chemistry. B* **111,** 6245–6262; 10.1021/jp070016c (2007).

153. Hu, P. & Hartmann, S. R. Theory of spectral diffusion decay using an uncorrelated-sudden-jump model. *Phys. Rev. B* **9,** 1–13; 10.1103/PhysRevB.9.1 (1974).

List of used Tools

Matlab: Used for simulation and analysis of EPR data, accessed through privately bought licenses and university licenses

EasySpin: Simulation toolbox for EPR simulations in Matlab. Downloaded in its current active version from the GitHub EasySpin repository.

DeerAnalysis: DEER analysis toolbox for Matlab.

Inkscape: Vector graphics editor.

Word: Used to write the PhD thesis and accessed through the Microsoft Office student package offered by the Technical University Dortmund, paid privately.

Grammarly: Grammar, spelling, and AI writing assistant. It was used for spellchecking and grammar corrections only in this thesis. Used with the free license.

PyMOL: Used to generate figures of 3D DNA and protein structures. The free version was downloaded from the PyMOL website and used with a student license.

Chemdraw: Used to draw the structures of chemicals.